

A NOVEL CONTENT-BASED RETRIEVAL SYSTEM FOR HYPERSPECTRAL
REMOTE SENSING IMAGERY

A THESIS SUBMITTED TO
THE GRADUATE SCHOOL OF INFORMATICS OF
THE MIDDLE EAST TECHNICAL UNIVERSITY
BY

FATİH ÖMRÜZUN

IN PARTIAL FULFILLMENT OF THE REQUIREMENTS FOR THE DEGREE OF
DOCTOR OF PHILOSOPHY
IN
THE DEPARTMENT OF INFORMATION SYSTEMS

MAY 2024

**A NOVEL CONTENT-BASED RETRIEVAL SYSTEM FOR HYPERSPECTRAL
REMOTE SENSING IMAGERY**

Submitted by **FATİH ÖMRÜUZUN** in partial fulfillment of the requirements for the degree of **Doctor of Philosophy in Information Systems Department, Middle East Technical University** by,

Prof. Dr. Banu GÜNEL KILIÇ
Dean, **Graduate School of Informatics**

Prof. Dr. Altan KOÇYİĞİT
Head of Department, **Information Systems**

Prof. Dr. Yasemin YARDIMCI ÇETİN
Supervisor, **Information Systems Dept., METU**

Prof. Dr. Uğur Murat LELOĞLU
Co-supervisor, **Space Engineering Dept.,
Turkish Aeronautical Association University**

Examining Committee Members:

Prof. Dr. Banu GÜNEL KILIÇ
Information Systems Dept., METU

Prof. Dr. Yasemin YARDIMCI ÇETİN
Information Systems Dept., METU

Prof. Dr. Begüm DEMİR
Faculty of Electrical Engineering and Computer Science,
Technische Universität Berlin

Prof. Dr. Pekin Erhan EREN
Information Systems Dept., METU

Assoc. Prof. Dr. Fatih NAR
Comp. Eng. Dept., Ankara Yıldırım Beyazıt University

Date: 27.05.2024

I hereby declare that all information in this document has been obtained and presented in accordance with academic rules and ethical conduct. I also declare that, as required by these rules and conduct, I have fully cited and referenced all material and results that are not original to this work.

Name, Surname: FATİH ÖMRÜUZUN

Signature :

ABSTRACT

A NOVEL CONTENT-BASED RETRIEVAL SYSTEM FOR HYPERSPECTRAL REMOTE SENSING IMAGERY

ÖMRÜUZUN, FATİH

Ph.D., Department of Information Systems

Supervisor: Prof. Dr. Yasemin YARDIMCI ÇETİN

Co-Supervisor: Prof. Dr. Uğur Murat LELOĞLU

May 2024, 127 pages

Due to the increased use of hyperspectral remote sensing payloads, there has been a rise in the number of hyperspectral remote sensing image archives, resulting in a massive amount of collected data. This highlights the need for a content-based image retrieval system that can manage and enable the use hyperspectral remote-sensing images efficiently. The conventional content-based hyperspectral image retrieval (CBHIR) systems define each image by a set of endmembers and then perform image retrieval using pairwise distance measures. However, this approach significantly increases the computational complexity of retrieval, especially when there is a high diversity of materials. Additionally, those systems have difficulties in retrieving images with particular materials whose abundance is extremely low compared to other materials or those that are not considered as an endmember while modeling the image. To address these issues, a novel CBHIR system is proposed that aims to define global hyperspectral image representations based on a semantic approach to differentiate background and foreground image content considering both spatial and spectral information. In this way, two spectral content dictionaries are used in the process of modeling hyperspectral images. While the first dictionary originates in spectral terms related to materials that are rarely encountered in the relevant geographical region, called foreground content, the second dictionary contains spectral terms for materials that are commonly seen in the geographical region, called background content. The proposed system consists of two main modules. The first module characterizes the hyperspectral images in the archive by four global descriptors: 1) two binary spec-

tral descriptors (which represent spectral characteristics of distinct foreground and background materials); 2) two abundance descriptors that model the normalized cumulative fractional abundance of the corresponding materials. The second module retrieves hyperspectral images from the archive that either cover materials that are most similar to the given query signature or query image based on a hierarchical strategy that evaluates the spectral and abundance descriptor similarity. Experiments conducted on a benchmark dataset of hyperspectral images demonstrated the system's effectiveness in terms of retrieval accuracy and time.

Keywords: remote sensing, hyperspectral imaging, content-based semantic retrieval, feature extraction

ÖZ

HİPERSPEKTRAL UZAKTAN ALGILAMA GÖRÜNTÜLERİ İÇİN YENİLİKÇİ BİR İÇERİK TABANLI ERİŞİM SİSTEMİ

ÖMRÜUZUN, FATİH

Doktora, Bilişim Sistemleri Bölümü

Tez Yöneticisi: Prof. Dr. Yasemin YARDIMCI ÇETİN

Ortak Tez Yöneticisi: Prof. Dr. Uğur Murat LELOĞLU

Mayıs 2024, 127 sayfa

Hiperspektral faydalı yüklerin yaygınlaşması ile birlikte hiperspektral uzaktan algılama görüntü arşivlerinin çeşitliliği ve elde edilen veri miktarının büyüklüğü de katlanarak artmaktadır. Bu durum, hiperspektral uzaktan algılama görüntülerinin verimli olarak kullanımı ve yönetimi için özel olarak tasarlanmış içerik tabanlı görüntü erişim sistemi ihtiyacını ortaya çıkarmaktadır. Geleneksel içerik tabanlı hiperspektral görüntü erişim (İTHGE) sistemleri her bir görüntüyü bir son üyeler kümesi ile tanımlamakta ve görüntü erişimini ikili uzaklık ölçümüne dayalı olarak gerçekleştirmektedir. Bu tip bir yaklaşım özellikle son üye sayısının yüksek olduğu durumlarda erişimin hesaplama karmaşıklığını önemli ölçüde artırmaktadır. Bunun ötesinde, bu sistemler varlığı diğerlerine nazaran çok düşük miktarda olan veya görüntüler modellenirken sonüye olarak nitelendirilmeyen materyalleri içeren görüntülere erişmekte zorluklar yaşamaktadır. Bu problemlerin çözümü için bu çalışmada farklı erişim senaryolarına uygun olarak küresel hiperspektral görüntü betimleyicileri tanımlamak için önplan ve arkaplan ayrıştırma yaklaşımlarıyla öznitelik tanımlayıcıları üretmeyi amaçlayan yenilikçi bir İTHGE sistemi sunulmaktadır. Bu şekilde, hiperspektral görüntülerin modelleme sürecinde iki spektral içerik sözlüğü kullanılmaktadır. İlk sözlük, ilgili coğrafi bölgede nadiren karşılaşılan ve ön plan olarak adlandırılan materyallerle ilgili spektral terimlerden meydana gelmektedir. İkinci sözlük ise coğrafi bölgede yaygın olarak görülen ve arka plan olarak adlandırılan materyallerle ilgili spektral terimleri içerir ve arka plan içeriği olarak adlandırılır. Bu maksatla, önerilen sistem iki ana kısımdan oluşmaktadır. İlk kısım arşivdeki hedef hiperspektral görüntülerini dört küresel tanımlayıcı ile tanımlamaktadır: 1) ön plan ve arka plan materyallerin spekt-

ral özelliklerini temsil eden iki adet ikili tanımlayıcı; 2) bu materyallerin normalize edilmiş oransal toplam varlık bilgisini içeren birer varlık tanımlayıcısı. İkinci kısım, sorgu imzasına en çok benzeyen materyalleri içeren veya sorgu görüntüsüne en çok benzeyen hiperspektral görüntülere spektral ve varlık tanımlayıcı benzerliklerini değerlendiren hiyerarşik bir yöntemle dayalı olarak arşivden erişim sağlamaktadır. Karşılaştırma amaçlı bir hiperspektral görüntü arşivi ile gerçekleştirilen deneyler önerilen sistemin erişim doğruluğu ve zaman bağlamındaki verimliliğini ortaya koymuştur.

Anahtar Kelimeler: uzaktan algılama, hiperspektral görüntüleme, içerik tabanlı anlamsal erişim, öznitelik çıkarımı

To my family and people who encouraged me throughout this long and challenging journey...

ACKNOWLEDGMENTS

I would like to express my deepest gratitude to my advisors, Prof. Dr. Yasemin Yardımcı Çetin, Prof. Dr. Uğur Murat Leloğlu, and thesis committee members Prof. Dr. Begüm Demir and Prof. Dr. Banu Günel Kılıç for their guidance and support through this tough journey. It was a great honor to work under their supervision during my PhD study where I formed my academic vision and intellectual attainments.

Besides my advisors, I would like to thank Prof. Dr. Lorenzo Bruzzone and my dear colleagues for their valuable contributions to this work and hospitality during my visit at the University of Trento, Remote Sensing Laboratory.

I am indebted to my colleagues at METU, Graduate School of Informatics, for the meaning they brought to my academic life. I am always proud of being a member of this precious family. In particular, I am grateful to Dr. Didem Başkurt for her endless support during this period.

I also express my gratitude to one of the key people in my life, Prof. Dr. Akın Cellatoğlu, who guided and encouraged me to pursue my academic career. I always felt lucky to know and have you in my life.

I am grateful to all those who sacrificed their lives, especially Mustafa Kemal Atatürk and his associates, for enabling me to complete this thesis in this country.

Finally, I would like to extend my heartfelt appreciation to my family, particularly my spouse Sibel Sel Ömrüuzun, for their steadfast support and patience throughout my life. Their unwavering commitment has been instrumental in my personal and professional development.

Part of this work was conducted at the University of Trento, Remote Sensing Laboratory and supported by TÜBİTAK-BİDEB 2214-A International Research Fellowship Programme for Ph.D. Students.

TABLE OF CONTENTS

ABSTRACT	iv
ÖZ	vi
DEDICATION	viii
ACKNOWLEDGMENTS	ix
TABLE OF CONTENTS	x
LIST OF TABLES	xiv
LIST OF FIGURES	xv
LIST OF ABBREVIATIONS	xix
CHAPTERS	
1 INTRODUCTION	1
1.1 Prologue	1
1.2 Problem Definition	2
1.3 Purpose of the Study	3
1.4 Structure of the Thesis	6
2 BACKGROUND	7
2.1 Spectral Remote Sensing	7
2.2 Working Principles of Hyperspectral Remote Sensing Systems	12

2.3	Hyperspectral Remote Sensing Systems	16
2.3.1	Airborne Systems	17
2.3.2	Spaceborne Systems	19
2.4	Review of Hyperspectral Remote Sensing Applications from a Content-Oriented Point of View	21
2.4.1	Land-Use Mapping / Classification	21
2.4.2	Environmental Monitoring	22
2.4.3	Precision Agriculture and Forestry	25
2.4.4	Mineralogy and Geology	27
2.4.5	Defense and Security	28
3	RELATED LITERATURE	31
3.1	Single Material Based Content Detection Methods for Hyperspectral Imagery	31
3.1.1	Full-Pixel Content Detection Algorithms	32
3.1.2	Sub-Pixel Content Detection Algorithms	34
3.2	Multiple Material Based Content Detection and Retrieval Methods for Hyperspectral Imagery	36
4	RESEARCH ACTIVITIES CONDUCTED WITHIN THE SCOPE OF THE THESIS	41
4.1	Research Carried on Single Material Based Content Detection	41
4.2	Research Carried on Multiple Material Based Content Detection	42
5	PROPOSED CONTENT-BASED HYPERSPECTRAL IMAGEG RETRIEVAL SYSTEM	47
5.1	Problem Formulation and Notation	50

5.2	Spectral Vocabulary Generation and Representing Hyperspectral Images with Low-Dimensional Descriptors	51
5.2.1	Super-pixel Based Content Segmentation	54
5.2.2	Background Suppression	55
5.2.3	Building Spectral Vocabularies	64
5.2.4	Representation of Hyperspectral Images with Low-Dimensional Descriptors	64
5.3	Retrieving Hyperspectral Images with Low-Dimensional Feature Descriptors	66
6	DATA-SET DESCRIPTION	71
6.1	Data Source	71
6.2	Data Pre-processing	71
6.3	Data Labelling	75
7	EXPERIMENTAL SETUP AND RESULTS	79
7.1	Experimental Setup	79
7.2	Experimental Results	81
7.3	Sample Retrieval Results for the Proposed CBHIR System	81
7.4	Further Performance Analysis of the Proposed CBHIR System	89
7.5	Comparative Performance Analysis	95
8	CONCLUSION AND FUTURE WORK	97
8.1	Conclusion	97
8.2	Future Work	99
	REFERENCES	101

A LIST OF AIRBORNE HYPERSPECTRAL REMOTE SENSING SYSTEMS	117
B LIST OF SPACEBORNE HYPERSPECTRAL REMOTE SENSING SYSTEMS	121
C SYMBOLS AND THEIR DESCRIPTIONS	123
CURRICULUM VITAE	125

LIST OF TABLES

Table 1	Categorization of CBHIR Scenarios	4
Table 2	Performance evaluation of CBHIR systems	45
Table 3	2021 Land Cover statistics by Food and Agriculture Organization (FAO) based on European Space Agency Climate Change Initiative - Land Cover (CCI-LC) Products (Value unit=1000 ha)	49
Table 4	Surface Reflectance-Derived Spectral Indices	61
Table 5	Landsat 9 Mission Operational Land Multispectral Imager 2 (OLI-2) Spectral Bands	62
Table 6	Specifications of sensors of imaging system used during data acquisition	73
Table 7	Fight parameters and corresponding ground resolutions obtained with the sensors	73
Table 8	Content labels for retrieval results, $X_q = X_{125}$	84
Table 9	Content labels for retrieval results, $X_q = X_{1211}$	85
Table 10	Content labels for retrieval results, $X_q = X_{1770}$	86
Table 11	Content labels for retrieval results, $X_q = X_{1914}$	87
Table 12	Content labels for retrieval results, $X_q = X_{2440}$	88
Table 13	Content labels for retrieval results, $X_q = X_{2678}$	89
Table 14	Content labels for retrieval results, $X_q = X_{150}$	90
Table 15	Content labels for retrieval results (down-scaled), $X_q = X_{1211}$	91
Table 16	Content labels for retrieval results (up-scaled), $X_q = X_{1211}$	92
Table 17	Content labels for retrieval results (down-scaled image), $X_q = X_{2440}$	93
Table 18	Content labels for retrieval results (down-scaled image), $X_q = X_{2440}$	94
Table 19	Performance evaluation of CBHIR systems	95

LIST OF FIGURES

Figure 1	Block diagram of a typical CBIR system.	3
Figure 2	Electromagnetic spectrum.	8
Figure 3	Illustrations of remote sensing systems based on use of natural solar energy in the measurement.	9
Figure 4	Spectral response curves of panchromatic and multispectral imaging payloads on WorldView-1 and WorldView-2 missions, respectively. .	10
Figure 5	Illustration of passive optical remote sensing systems and information density in the spectral domain.	11
Figure 6	Spectral signatures of materials dominantly covering the Earth's surface in METU campus.	11
Figure 7	Common hyperspectral remote sensing design approaches.	13
Figure 8	Dispersion unit based spectral selection designs.	14
Figure 9	Tunable filter based spectral selection design.	15
Figure 10	Michelson interferometer.	15
Figure 11	Spectral regions and corresponding detector materials.	16
Figure 12	ARCHER hyperspectral remote sensing system installed on GipsAero GA8.	18
Figure 13	Nano-Hyperspec hyperspectral remote sensing system installed on DJI M600 Pro UAV.	18
Figure 14	EO-1 Mission and a false-color representation of a hyperspectral image acquired by Hyperion payload.	20
Figure 15	Land-use mapping results of classification method proposed in [1] in study area 1.	22
Figure 16	AVIRIS visible-color composite image and example signatures from oil-spill disaster area [2].	23
Figure 17	Multi-temporal hyperspectral imagery acquired over New Orleans (a) September 2010, (b) October 2011, and (c) change detection map generated by the method proposed in [3].	24

Figure 18	(a) Thermal image of a segment of the Long Beach industrial corridor (b) CO ACE detection image.	24
Figure 19	Plant nitrogen retrieval map generated by method proposed in [4].	25
Figure 20	(a) Detection of afforested areas, (b) estimated positions of new trees to be planted [5].	26
Figure 21	Summary of the main deposit types in relation to areas in the spectrum (indicated by the bars) where absorption occurs related to the presence of key alteration minerals [6].	27
Figure 22	Material map of EnGeoMAP 2.0 calculated from airborne HyMAP data [7].	28
Figure 23	(a) RGB composite image of the data set, (b) Camouflage detection result [8].	29
Figure 24	Linear and non-linear mixed pixel models.	37
Figure 25	Mixed pixel signature.	38
Figure 26	Block diagram of the proposed bag-of-endmembers based CBHIR system.	43
Figure 27	Retrieval results of evaluated systems.	46
Figure 28	Terra MODIS MOD12C1 17 land cover classes defined by the IGBP.	48
Figure 29	Dominant and rarely observed content types in remote sensing images.	49
Figure 30	Pseudo-color representation of a remote sensing hyperspectral image X_{1323} (a), illustration of foreground (b) and background (c) image contents.	50
Figure 31	Block diagram of the proposed CBHIR system.	52
Figure 32	Sample super-pixel based content segmentation with hyperSLIC.	56
Figure 33	Candidate background content regions for a hyperspectral remote sensing payload product.	57
Figure 34	Sample hyperspectral images with low and high spectral diversity.	58
Figure 36	Average NDVI scores for different types of background content in hyperspectral imagery.	59
Figure 35	Background content regions designated by the proposed CBHIR system for hyperspectral remote sensing payload products.	60

Figure 37	Foreground-background content segment classification.	63
Figure 38	Illustration of low-dimensional foreground and background content descriptors.	65
Figure 39	Illustration of low-dimensional overall content descriptors.	65
Figure 40	Fingerprint of the area imaged during flight and used in benchmark archive generation.	72
Figure 41	Multi-modal sensor configuration of the imaging system.	73
Figure 42	Proper labelling of hyperspectral images thanks to VHR multispectral imagery acquired during the same flight.	76
Figure 43	Fingerprint of the area imaged during flight and used in benchmark archive generation.	76
Figure 44	Taxonomy of content labels and corresponding number of images labeled under each sub-category.	77
Figure 45	VHR multispectral image portion of the region containing railway ballast material, steel rail, natural vegetation cover, and stabilized road.	82
Figure 46	VHR multispectral image portion of the region containing white tent tarpaulin.	83
Figure 47	VHR multispectral image portion of the region containing water stream, gravel road and vegetation.	83
Figure 48	Content-based retrieval results of the proposed CBHIR system, $\mathbf{X}_q = \mathbf{X}_{125}$.	84
Figure 49	Content-based retrieval result, $\mathbf{X}_q = \mathbf{X}_{1211}$.	85
Figure 50	Content-based retrieval result, $\mathbf{X}_q = \mathbf{X}_{1770}$.	86
Figure 51	Content-based retrieval result, $\mathbf{X}_q = \mathbf{X}_{1914}$.	87
Figure 52	Content-based retrieval result, $\mathbf{X}_q = \mathbf{X}_{2440}$.	88
Figure 53	Content-based retrieval result, $\mathbf{X}_q = \mathbf{X}_{2678}$.	89
Figure 54	Content-based retrieval result, $\mathbf{X}_q = \mathbf{X}_{150}$.	90
Figure 55	Content-based retrieval result (down-scaled), $\mathbf{X}_q = \mathbf{X}_{1211}$.	91
Figure 56	Content-based retrieval result (down-scaled image), $\mathbf{X}_q = \mathbf{X}_{150}$.	92
Figure 57	Content-based retrieval result (down-scaled image), $\mathbf{X}_q = \mathbf{X}_{2440}$.	93

Figure 58 Content-based retrieval result (up-scaled image), $X_q = X_{2440}$... 94

LIST OF ABBREVIATIONS

AAHIS	Advanced Airborne Hyperspectral Imaging System
ACE	Adaptive Cosine Estimator
AHS	Airborne Hyperspectral Scanner
AIS-1	Airborne Imaging Spectrometer-1
AIS-2	Airborne Imaging Spectrometer-2
A-PPI	Automatic Pixel Purity Index
ARCHER	Airborne Real-time Cueing Hyperspectral Enhanced Reconnaissance
ARIES	Australian Resource Information and Environment Satellite
ASAS	Advanced Solid-state Array Spectroradiometer
ASI	Italian Space Agency
AVIRIS	Airborne Visible Infrared Imaging Spectrometer
BSAD	Binary Spectral and Abundance Descriptor
BSD	Binary Spectral Descriptor
CASI	Compact Airborne Spectrographic Imager
CAST	China Association for Science and Technology
CBHIR	Content-Based Hyperspectral Image Retrieval
CBIR	Content-Based Image Retrieval
CCD	Charge-coupled Device
CCI-LC	European Space Agency Climate Change Initiative - Land Cove
CEM	Constrained Energy Minimization
CHRIS	Compact High-Resolution Imaging Spectrometer
CMOS	Complementary Metal-Oxide-Semiconductor

CNSA	China National Space Administration
COIS	Coastal Ocean Imaging Spectrometer
COMPASS	COMPact Airborne Spectral Sensor
CRISM	Compact Reconnaissance Imaging Spectrometer for Mars
CSA	Canadian Space Agency
CSIRO	Commonwealth Scientific and Industrial Research Organisation
DAIS	Digital Airborne Imaging Spectrometer
DBSCAN	Density-Based Spatial Clustering of Applications with Noise
DCGAN	Deep Convolutional Generative Adversarial Network
DESIS	DLR Earth Sensing Imaging Spectrometer
DLR	German Aerospace Center
DoD	United States Department of Defense
DSM	Digital Surface Model
EIHA	Endmember Induction Heuristic Algorithm
EM-Grana	Grana Distance
EM-WSAD	Endmember Matching Algorithm That Weights the Distances Estimated by the SAD
EnMAP	Environmental Mapping and Analysis Program
EO	Earth Observatory
EO-1	Earth Observing-1
EOC	Earth Observation Center
EOS	Earth Observing System
ESA	European Space Agency
EVI	Enhanced Vegetation Index
FAO	United Nations Food and Agriculture Organization

FLAASH	Fast Line-of-sight Atmospheric Analysis of Spectral Hyper-cubes
FODIS	Fiber Optic Downwelling Irradiance Sensor
FTHSI	Fourier Transform Hyperspectral Imager
GHGSat	Greenhouse Gas Satellite
GLCM	Gray Level Co-occurrence Matrix
GLRT	Generalized Likelihood Ratio Test
GPR	Ground Penetrating Radar
GPS/IMU	Global Positioning System/Inertial Measurement Unit
HDOS	Hughes Danbury Optical Systems
HDPU	Hyperspectral Data Processing Unit
HERO	Hyperspectral Environment and Resource Observer
HgCdTe	Mercury Cadmium Telluride (a.k.a. MCT)
HICO	Hyperspectral Imager for the Coastal Ocean
HIRIS	High Resolution Imaging Spectrometer
HIS	Hyperspectral Imager
HISUI	Hyperspectral Imager Suite
HJ-1	Huan Jing-1
HRIS	High-Resolution Imaging Spectrometer
HYDICE	Hyperspectral Digital Imagery Collection Experiment
HyMAP	Hyperspectral Mapper
hyperSLIC	Hyperspectral Simple Linear Iterative Clustering
HyperSEO	HyperSpectral Earth Observer
HySI	Hyper Spectral Imager
HYSIS	Hyperspectral Imaging Satellite
HyspIRI	Hyperspectral Infrared Imager

IFOV	Instantaneous Field of View
IGBP	International Geosphere-Biosphere Programme
IIM	Interference Imaging spectrometer
InGaAs	Indium Gallium Arsenide
ISRO	Indian Space Research Organisation
ISS	International Space Station
İTHGE	İçerik Tabanlı Hiperspektral Görüntü Erişim
JAXA	Japan Aerospace Exploration Agency
JM	Jeffries-Matusita Distance
L1R	Level-1-Radiance
LiDAR	Light Detection and Ranging
LWIR	Long-Wave Infrared
LZW	Lempel–Ziv–Welch
M3	Moon Mineralogy Mapper
MAS	MODIS Airborne Simulator
MASI	Midwave Infrared Airborne Spectrographic Imager
METU	Middle East Tehnical University
MF	Matched Filter
MODIS	MODerate-resolution Imaging Spectroradiometer
MRO	Mars Reconnaissance Orbiter
MSAVI	Modified Soil Adjusted Vegetation Index
μm	Micrometer
MWIR	Mid-Wave Infrared
NA	North American Airlines (IATA code: NA)
NASA	National Aeronautics and Space Administration
NASA/JPL	National Aeronautics and Space Administration/Jet Propulsion Laboratory

NBR	Normalized Burn Ratio
NBR2	Normalized Burn Ratio2
NDMI	Normalized Difference Moisture Index
NDSI	Normalized Difference Snow Index
NDVI	Normalized Difference Vegetation Index
NEMO	Naval Earth Map Observer
NIR	Near Infrared
nm	Nanometer
NSA	China National Space Administration
OHIS	OrbView Hyperspectral Imaging System
OLI-2	Operational Land Multispectral Imager
ONERA	The French Aerospace Lab
OPD	Optical Path Difference
OSP	Orthogonal Subspace Projection
PCA	Principal Component Analysis
PPI	Pixel Purity Index
PRISM	Picosatellite for Remote Sensing and Innovative Space Mis- sions
PRISMA	PRecursore IperSpettrale della Missione Applicativa
Proba	Project for On-Board Autonomy
QUAC	Quick Atmospheric Correction
RADAR	Radio Detecting and Ranging
RAM	Random Access Memory
RGB	- Red-Green-Blue
ROSIS	Reflective Optics System Imaging Spectrometer
RX	Reed-Xiaoli

SAD	Spectral Angular Distance
SAM	Spectral Angle Mapper
SAR	Synthetic Aperture Radar
SASI	Shortwave Infrared Airborne Spectrographic Imager
SAVI	Soil Adjusted Vegetation Index
SCM	Spectral Correlation Mapper
SEBASS	Spatially Enhanced Broadband Array Spectrograph System
SHARK	Selectable Hyperspectral Airborne Remote-sensing Kit
SID	Spectral Information Divergence
SIFT	Scale-Invariant Feature Transform
SLIC	Simple Linear Iterative Clustering
SMIFTS	Spatially Modulated Imaging Fourier Transform Spectrometer
SNR	Signal-to-Noise Ratio
SPECTRA	Surface Processes and Ecosystem Changes Through Response Analysis
SSMA	Spectral Signature Matching Algorithm
SSR	Single Stage Retrieval
STME	Sparse Transfer Manifold Embedding
SUnSAL	Sparse Unmixing via variable Splitting and Augmented Lagrangian
SWIR	Shortwave Infrared
SYSSIPHE	Système Spectro-Imageur de Mesure des Propriétés Hyperspectrales Embarqué
TacSat-3	Tactical Satellite-3
TASI	Thermal Infrared Airborne Spectrographic Imager
TE	Thermoelectric
TRWIS	TRW Imaging Spectrometer

TSHR	Two-stage Hierarchical retrieval
UAV	Unmanned Aerial Vehicle
USAF	United States Air Force
USGS	United States Geological Survey
UVNS	Ultraviolet Visible Near-infrared Shortwave Spectrometer
VCA	Vertex Component Analysis
VHR	Very High Resolution
VNIR	Visible-Near Infrared

CHAPTER 1

INTRODUCTION

1.1 Prologue

In recent years, hyperspectral imaging has become a prominent passive optical remote sensing technology utilized to solve various problems in diverse fields. From recognizing plant diseases in precision agriculture to buried object detection in military operations, hyperspectral imaging has taken place in applications [9] where observing the distinctive spectral features of matters is crucial. Consequently, a continuous increase in the deployment of hyperspectral imaging systems leads to significant growth in the diversity and volume of hyperspectral remote sensing image collections.

Certainly, the most notable feature of hyperspectral imaging, which distinguishes it from other passive optical remote sensing techniques, is the abundance of information provided in the spectral domain. Hyperspectral imaging is a technique that involves capturing a large number of observation channels at consecutive wavelengths. This method enables the precise recognition and discrimination of objects in a scene, making it a valuable tool in various fields. On the other hand, dense spectral information provided in hyperspectral imagery results in a higher amount of data to be processed than other optical imaging techniques. Moreover, the vast amount of data generated in imaging campaigns can pose a challenge when it comes to effectively utilizing hyperspectral images for interpretation and management purposes. Depending on application needs, this fact may limit potential benefits that can be obtained from hyperspectral imagery. Accordingly, one of the critical tasks in remote sensing is the accurate and fast retrieval of hyperspectral images from image collections in the context of spectral properties of the matter.

This thesis comprehensively addresses content-based retrieval of hyperspectral imagery from different perspectives and proposes a promising system, which is established on novel semantic hyperspectral image descriptors that achieve both high accuracy and low computational complexity.

1.2 Problem Definition

Digitalization has exposed people to deal with unique data management and interpretation problems in many fields, especially those associated with intense usage of digital imagery. Particularly in fields where large amounts of images are processed to solve crucial problems, rapid and accurate access to desired images in collections has been a crucial task. Remote sensing is one of those fields in which a substantial amount of digital images are created at very high speed in different formats by diverse systems. Moreover, the repetitive nature of remote sensing image acquisition campaigns results in an exponential increase in the cumulative amount of images created.

Images acquired during remote sensing campaigns are either interpreted by visual inspection of individuals or by computers in a relatively automated way for various purposes, i.e., environmental monitoring, change detection, disaster management, or target detection. Hence, accessing desired images in collections comprising desired (or hidden) content is crucial for remote sensing applications. Moreover, the time required for accessing desired images in the collections may be vital for certain applications.

Initially, images in such collections were manually classified by associated subjective keywords that describe image content and meta tags (e.g., content labels, comments, location, acquisition time, etc.) to ensure easy access to desired images. However, this approach holds two main drawbacks: 1) exponential increase in both diversity and amount of images in the collections requires excessive labor force for keyword assignment, and 2) keyword assignment is an error-prone task, and proposed keywords may not sufficiently describe overall image content.

In order to overcome these drawbacks by retrieving images from collections in an autonomous way, *Content-Based Image Retrieval (CBIR)* paradigm was proposed at the end of the 90s. The simplest definition of CBIR is “*the process of retrieving desired images from a large collection of images on the basis of features...*” [10]. In other words, computer algorithms extract content feature descriptors to retrieve images from digital image collections instead of relying on subjective keywords assigned by individuals. Thus, CBIR systems are designed to optimize the use of image collections by effectively capturing content descriptors within images. This enables users to easily search and retrieve images based on image descriptors, making the process more efficient and streamlined.

The working principle of a CBIR system, whose basic components are illustrated in Figure 1, can be summarized as follows. A typical CBIR system is composed of two essential modules: 1) feature extraction module and 2) retrieval module. The feature extraction module is responsible for obtaining comparable content descriptors from images in the collection and given query image. It is worth noting that descriptors extracted in this phase of the system are fully dependent on characteristic properties (e.g. number of spectral channels or spatial resolution) of the images. In the following phase, the retrieval module performs a similarity assessment between the query image

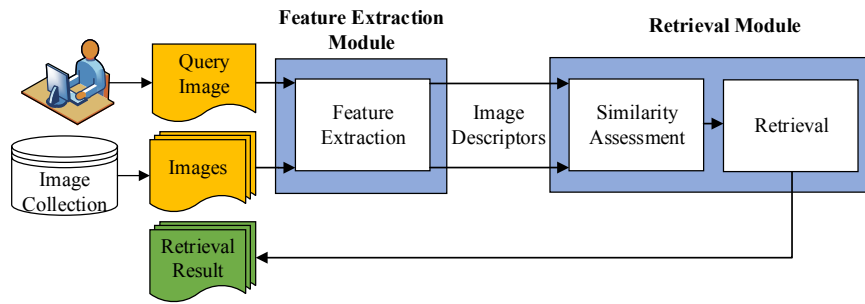


Figure 1: Block diagram of a typical CBIR system.

and each image in the collection, considering the descriptor(s) obtained in the first phase. Finally, a set of most similar images to the given query image is returned to the user.

Hyperspectral imaging is a passive optical remote sensing technology gaining popularity in various industries. Depending on the region of interest in the electromagnetic spectrum, hyperspectral imaging instruments can acquire images characterized by very high spectral resolution that results in hundreds of discrete observation channels. This feature of hyperspectral imagery provides detailed information about the chemical composition of materials in a given scene. Thus, dense spectral information provided in hyperspectral imagery leads to a very high capability for identifying and discriminating objects. Consequently, content-based hyperspectral image retrieval (CBHIR) is the process of querying hyperspectral image collections in the context of materials through the dense information in the spectral domain.

Hyperspectral imaging is a powerful tool that enables us to tackle a diverse range of challenges in remote sensing. Unlike other passive optical imaging instruments, it offers unique capabilities to help us overcome complex problems and achieve better results. However, extensive usage of hyperspectral imaging instruments led to a rapid increase in the number and diversity of hyperspectral image collections. On the other hand, efficient and precise retrieval of hyperspectral images from collections is a key challenge in remote sensing. With the growing popularity of hyperspectral imaging technology, there is a pressing need to develop reliable content-based retrieval systems. However, the high number of observation channels that deliver dense spectral information in hyperspectral imagery requires unique methods and dedicated content-based retrieval systems to retrieve the images from such collections efficiently.

1.3 Purpose of the Study

Compared to other passive optical remote sensing techniques, the most notable feature of hyperspectral imaging is its ability to distinguish objects in a given scene through spectral features observed at consecutive wavelengths. Thus, hyperspectral imaging enables having intense information regarding the chemical structures of the materials forming the scene. Accordingly, distinctive spectral characteristics of the

Table 1: Categorization of CBHIR Scenarios

Scenario	Quantity of Materials	Abundance
1	Single Material	Insignificant
2	Single Material	Significant
3	Multiple Materials	Insignificant
4	Multiple Materials	Significant

objects play a crucial role in the content-based retrieval of hyperspectral imagery. Content-based hyperspectral image retrieval involves searching image collections for images that depict materials with similar spectral features to the query, allowing for efficient and accurate identification of desired images. This fact is the most important point distinguishing hyperspectral image retrieval from conventional image retrieval tasks mainly built on color, shape, and texture descriptors.

Hyperspectral image processing methods provide detailed information on the variety of discrete materials and their abundance in a scene. Depending on the diversity of spectrally distinct materials and their significance, four different CBHIR scenarios can address various retrieval problems, as listed in Table 1.

The first and second scenarios are associated with cases where the CBHIR system is employed to retrieve images containing a specific material defined by the query. These two scenarios are mostly experienced in the form of target content detection applications in which the existence of a specific material represented by the query in the image (either at the pixel or sub-pixel level) is of vital importance. In the second scenario, the retrieval process is enhanced by considering the abundance of the material of interest as a key factor. This helps to ensure a more efficient and effective search for the desired matter.

In scenarios three and four, the hyperspectral images are searched for images that contain more than one significant material whose spectral features are shown in the query. Unlike the third scenario, the fourth scenario also considers the abundance of materials given in the query. Accordingly, as the number of materials queried increases, these two scenarios require specific methods differently from the first and the second ones.

This study proposes a CBHIR system that offers dedicated solutions to each of the four scenarios given in Table 1, where the aim is retrieving hyperspectral images having material(s) in common either by querying via a single material signature or a query image covering multiple materials.

The CBHIR systems proposed in the literature rely on the descriptors related to the spectral signatures of distinct materials that are modeled by endmembers and the corresponding abundances present in the images. After extracting all the endmembers from both the query and the images in the collection, CBHIR systems calculate the similarity between the query and each collection image endmember pairs. Based on the usage scenarios mentioned in Table 1, these systems have three main limitations:

1) they do not provide a complete solution that covers first and second scenarios in Table I where images are retrieved by querying a material represented by a spectral signature and corresponding abundance (if defined), 2) computational cost and retrieval time increases proportionally to the number of endmembers contained in the images that pose a fundamental problem for on-line retrieval; 3) storage of all the endmembers in the auxiliary archive (a database that is exploited by performing analyses on extracted features, and thus it serves as an auxiliary archive complementary to the data archives) is challenging as they are often represented in a very high dimensional feature space. A more compact representation based on global features is required when dealing with large-scale hyperspectral image retrieval. Thus, these systems may be inappropriate for large-scale hyperspectral image retrieval problems.

In addition to the usage scenario limitations, existing CBHIR systems proposed in the literature have additional shortcomings.

1. Spectral information redundancy due to the relatively high amount of some content types (e.g., terrestrial barren lands, grasslands, sparsely natural vegetated areas) in the archive images that causes poor retrieval performance.
2. CBHIR methods that model hyperspectral images by only endmembers may not accurately extract the endmembers from the images, or pure material signatures may not exist in the scene. These issues may lead to describing image content with inappropriate and/or insufficient spectral features.
3. Strategies (i.e., bag-of-endmembers) that aim at combining and clustering all endmembers to generate a global spectral vocabulary to model hyperspectral images may ignore spectral signatures (endmember) of rarely seen content in case of using an inappropriate clustering method or setting parameters of clustering method inaccurately.

To overcome these problems and to provide a single complete solution to all scenarios defined in Table I, we claim that a CBHIR system should have the following critical functions: 1) characterizing each hyperspectral image with global hyperspectral image representations that can both describe and summarize image content and 2) effectively assessing similarities between defined global descriptors. To this end, we introduce a novel semantic CBHIR system that consists of two modules. The first module is devoted to representing each hyperspectral image with four low-dimensional global feature descriptors: 1) two spectral descriptors (which represent spectral characteristics of distinct foreground and background content); 2) two abundance descriptors (which model fractional abundance of corresponding materials in a given image). This is achieved by differentiating foreground and background content to derive a compact and distinctive representation of hyperspectral imagery. It is worth noting that the proposed global features represent a suitable alternative to the direct use of endmembers when considering scenarios in which very large amounts of endmembers have to be processed, stored, and compared.

The proposed solution, built on global hyperspectral image descriptors, offers a good compromise between efficiency and accuracy, especially considering large-scale on-

line hyperspectral image retrieval. Then, the second module is devoted to retrieving images similar to the query regarding materials included in the image by assessing the similarities of spectral and abundance descriptors. This is achieved based on a hierarchical retrieval strategy, where a predefined number of images are initially selected according to similarities based on the spectral descriptors. Then, among the selected images, those with the highest similarity in abundance descriptors are selected as the final result set. Thanks to this strategy, global features computed by summarizing content signatures into a fixed-dimensional feature vector are effectively employed in the context of large-scale hyperspectral image retrieval.

Experiments carried out on a large-scale real multi-label benchmark hyperspectral image collection demonstrate that the proposed system is capable of accurately retrieving hyperspectral images that comprise materials with low computational complexity either queried via a single material signature or a query image depicting one or more materials as well as their fractional abundances.

Novelties of the proposed system consist of 1) design and development of a semantic approach that can summarize spectral features of distinct materials and their corresponding abundance in hyperspectral images; 2) employment of a novel off-line feature extraction approach working in background that allows real-time retrieval of hyperspectral imagery; 3) use of hierarchical image retrieval strategy to employ abundance information for improving retrieval accuracy of the system.

1.4 Structure of the Thesis

The thesis is organized as follows. After Chapter [1](#), where the definition and proposed solution to the problem are introduced, Chapter [2](#) discusses the hyperspectral imaging phenomenon in detail and scrutinizes the retrieval problem from different aspects. In Chapter [3](#), a comprehensive review of CBHIR systems previously proposed in the literature is presented. Chapter [4](#) summarizes the research activities performed within the scope of the thesis except for the proposed novel CBHIR system. Chapter [5](#) explains the problem formulation and elaborates on the proposed CBHIR system. Chapter [6](#) introduces the multi-label hyperspectral image collection used in the experiments and explains the details of the experimental setup. Chapter [7](#) addresses the comparative experimental results. Finally, Chapter [8](#) concludes the study, points out the future works to be conducted on the proposed system for ensuring performance improvements, and draws the conclusion of this work.

CHAPTER 2

BACKGROUND

2.1 Spectral Remote Sensing

In the broadest sense, remote sensing is the science of obtaining information regarding any object or phenomenon through analysis of the data acquired by an instrument that is not physically in touch or contact. However, in the present context, remote sensing refers to all methods of obtaining information about any phenomenon (earth, lunar, and planetary surfaces, oceans, atmosphere, etc.) through investigating the data acquired by airborne (e.g., satellite or aircraft) sensor systems those are capable of sensing electromagnetic radiation reaching from the target surface.

Electromagnetic radiation is a sinusoidal wave carrying a certain quanta of energy that propagates through space at the speed of light. In remote sensing, electromagnetic radiation is broadly characterized by the wavelength (λ) notion that refers to the distance between two consecutive peaks of the sinusoidal. The amount of energy defined by certain radiation is inversely proportional to its wavelength. In other words, electromagnetic radiation having lower wavelengths has higher frequency and energy.

Electromagnetic spectrum defines the range of all possible electromagnetic radiation that can be observed and categorizes them with respect to their wavelengths (or frequencies) within several regions, such as visible, infrared, microwave, or radio waves (please see Figure 2). For instance, wavelengths lying through 400 nm and 700 nm are regarded as *visible* where the human eye is sensitive to electromagnetic radiation only in this region that defines the color spectrum for human perception. It is worth noting that the sensitivity of remote sensing systems is not limited to visible regions. Therefore, various detector materials are used to sense and quantify electromagnetic radiation in other spectral regions for different purposes.

In remote sensing, electromagnetic radiation that reaches from the target surface to the imaging system may originate in three ways: 1) thermal radiation self-emitted by matters, 2) naturally available solar radiation reflected by matters, or 3) auxiliary radiation (illumination) reflected from matters that are priorly emitted by the imaging system.

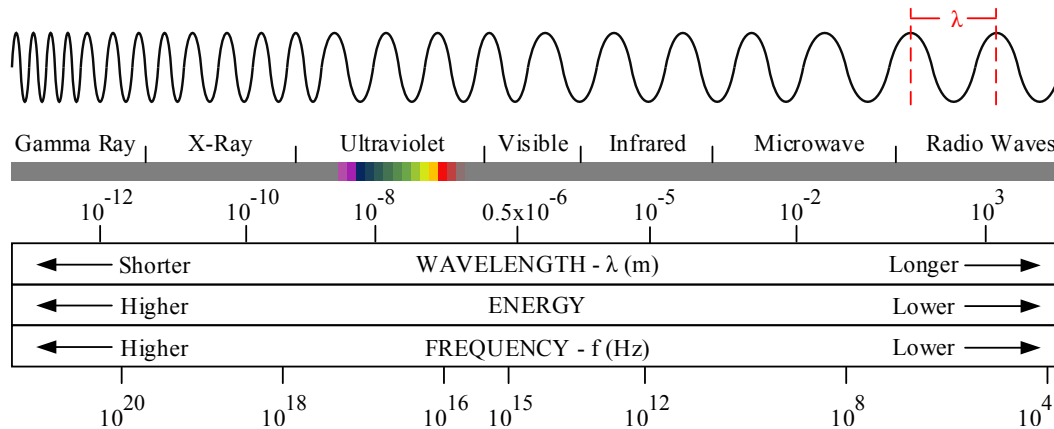


Figure 2: Electromagnetic spectrum.

Depending on the use of the auxiliary illumination in the measurement process, imaging systems utilized in remote sensing are grouped under two categories: active and passive systems. In active remote sensing, synthetic radiation required for illumination is generated by the imaging system and emitted towards the target surface. Subsequent to the illumination phase, which is performed at specific wavelengths, reflected or backscattered energy from matters existing on (or beneath) the target surface is measured to generate the image (Figure 3 (a)). SAR, GPR, and LiDAR are commonly used imaging systems in active remote sensing that provide useful information regarding the physical features (e.g., roughness, strictness, and structural forms) of the matter.

Contrary to active systems, passive remote sensing imaging systems do not use any auxiliary illumination and measure the amount of solar radiation reflected or thermal radiation self-emitted by the matters (Figure 3 (b)). This is achieved by quantifying electromagnetic radiation reaching from the target surface by means of detectors that are sensitive in narrow or broad sections of the electromagnetic spectrum.

Spectral remote sensing is a branch of passive remote sensing that focuses on how matters interact with naturally available solar energy. Measured energy at the imaging sensor is determined by spectral characteristics of the matters with respect to what extent the materials absorb, transmit or reflect the incident solar radiation as a function of wavelength through the electromagnetic spectrum. Depending on how molecules consume the energy, a certain amount of incident solar radiation is absorbed by the matter at different portions of the electromagnetic spectrum, and the rest of the energy is either transmitted or reflected back to the atmosphere. For instance, chlorophyll pigment, which gives green color to plant leaves, causes absorption of most of the incident solar radiation in the visible region (400-700 nm) for photosynthesis and strongly reflects the energy at near-infrared (700-1100 nm) region of the electromagnetic spectrum. Similarly, matters in a gaseous state generally transmit energy in VNIR, NIR, and SWIR spectral regions, and they can show high energy reflection or absorption characteristics at specific wavelengths of MWIR or LWIR regions. Thus,

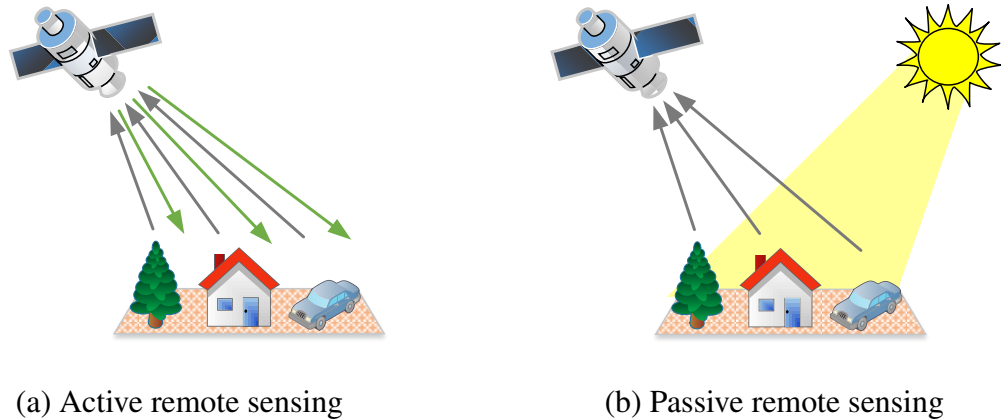


Figure 3: Illustrations of remote sensing systems based on use of natural solar energy in the measurement.

spectral remote sensing enables having detailed information about the chemical structures of the matter by observing how they interact with the incident solar radiation at miscellaneous wavelengths.

According to several observation channels in the resulting image, spectral remote sensing systems are divided into three categories. Panchromatic imaging systems have a single-channel detector sensitive to a broad section of the electromagnetic spectrum. Spectral response (sensitiveness) plot of a typical panchromatic imaging payload (WorldView-1) as a function of wavelengths in visible and near-infrared regions is indicated in black in Figure 4. Accordingly, panchromatic remote sensing systems generate a single-channel digital image in that each pixel of the image is represented by a grayscale intensity value determined by a weighted average of sensed energy through a particular spectral region that is defined by the quantum efficiency of the sensor material. On the other hand, as shown in Figure 4, multispectral passive optical remote sensing systems (e.g., WorldView-2) use multi-channel (typically ranges between 3 and 12) detectors that each channel is sensitive to a specific portion of the electromagnetic spectrum. Consequently, images acquired by multispectral remote sensing systems are composed of more than one channel, and a particular pixel is represented by a sequence of numbers whose elements correspond to a gray level intensity value at a specific observation channel. Thus, the most outstanding difference between these two passive remote sensing systems is increasing information density in the spectral domain as illustrated in Figure 5 (a) and (b). This advantage of the multispectral systems brings chrominance and enables differentiation of image pixels with respect to spectral features characterized at each observation channel.

Hyperspectral imaging is yet another relatively new generation of passive optical remote sensing technology that measures reflected or emitted energy from the matter on the target surface at frequent intervals through a specific region of the electromagnetic spectrum. In other words, a hyperspectral image comprises tens (or hundreds) of

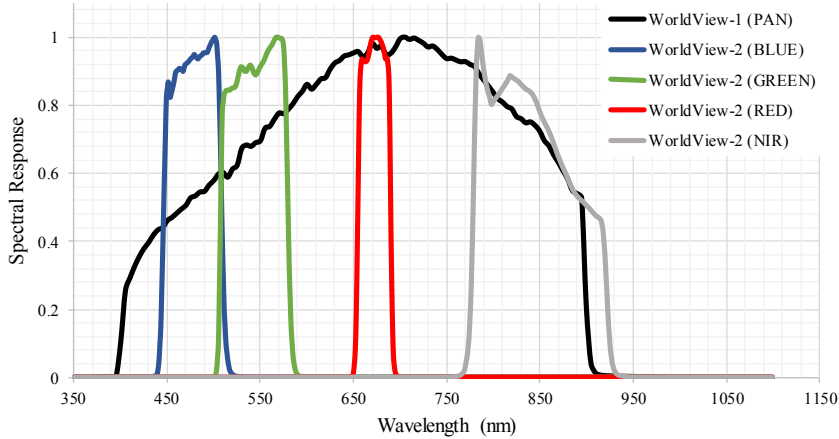


Figure 4: Spectral response curves of panchromatic and multispectral imaging payloads on WorldView-1 and WorldView-2 missions, respectively [11, 12].

inherently registered observation channels at successive wavelengths. Consequently, sequentially ordered observation channels, so-called hyperspectral cubes, give intense spectral information about the matters in the scene.

Like multispectral imagery, hyperspectral image pixels are represented by a sequence of numbers whose elements correspond to a gray-level intensity value measured at a specific wavelength section. The sequence of values observed along the spectral dimension of a hyperspectral image pixel generates a discrete signal called *spectral signature* or *chemical fingerprint* (Figure 5(c)). This signature represents distinctive spectral features of the matter(s) present in a pixel at each wavelength where the observation is performed. Hence, spectral signatures provide useful information about the chemical structures of the materials that have never been achieved by other spectral imaging systems. Accordingly, in the literature, hyperspectral imaging is also called chemical imaging or imaging spectroscopy.

Spectral signatures of materials dominantly covering the Earth’s surface in the Middle East Technical University (METU) campus, extracted from a hyperspectral image acquired by the National Aeronautics and Space Administration (NASA) Earth Observatory-1 (EO-1) Hyperion mission, are given in Figure 6. The figure visually compares two spectral remote sensing systems (multispectral and hyperspectral) regarding spectral resolution and spatial coverage.

It is worth noting that apart from the number of observation channels in the resulting image, there are two essential differences between multispectral and hyperspectral sensing: 1) none of the multispectral observation channels may cover a particular section within the spectral region of interest, 2) two or more multispectral observation channels may overlap in particular sections of the electromagnetic spectrum where the image is acquired. Accordingly, these drawbacks of multispectral remote sensing may cause a loss of spectral information. On the other hand, hyperspectral remote sensing overcomes these drawbacks by fully covering the portion of the elec-

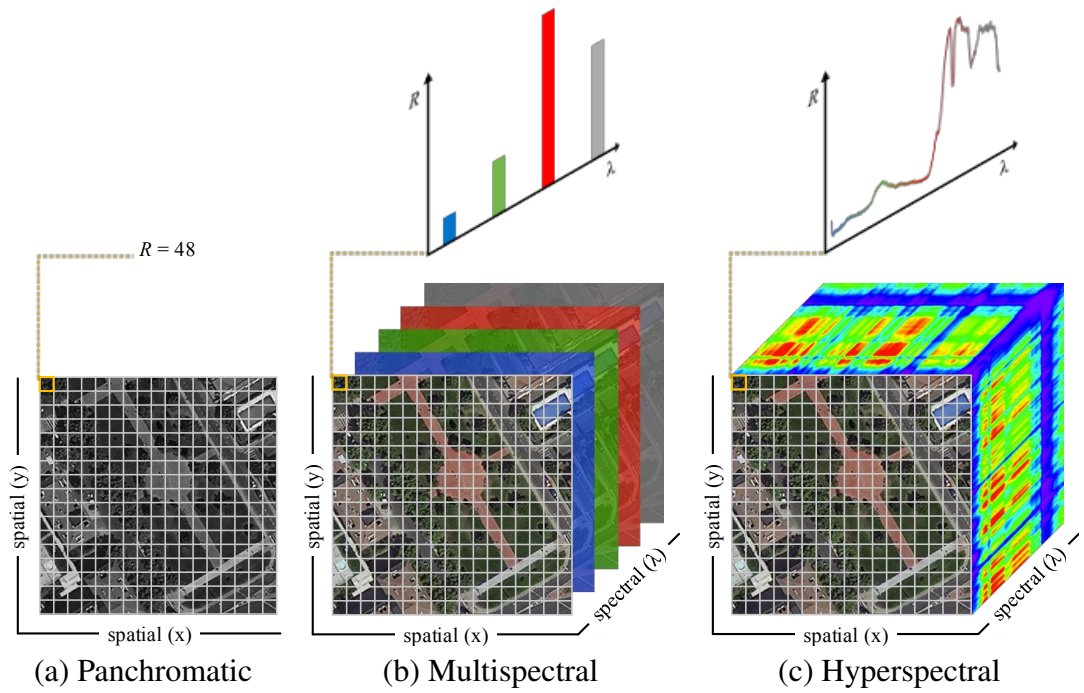


Figure 5: Illustration of passive optical remote sensing systems and information density in the spectral domain.

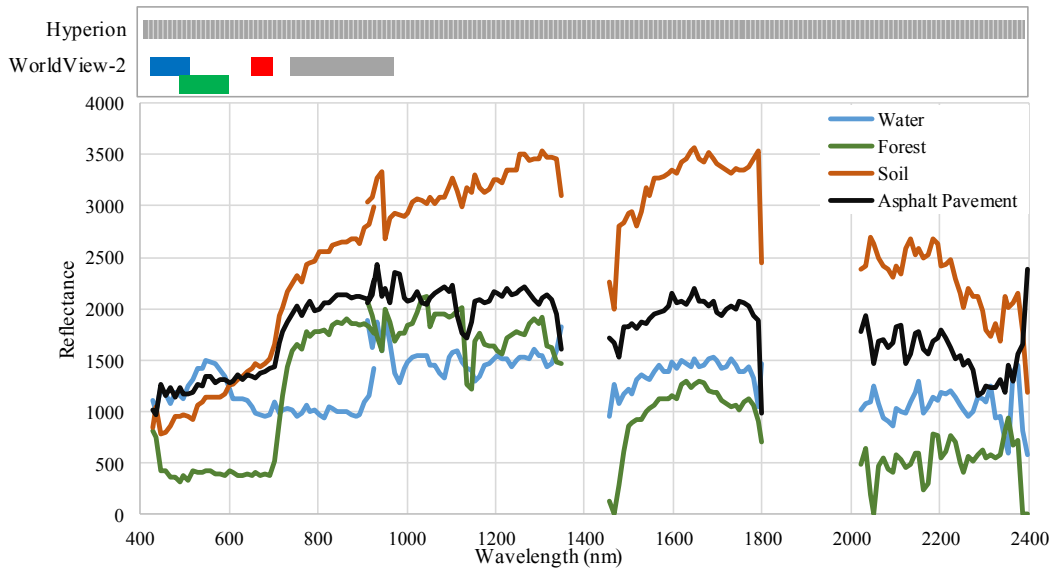


Figure 6: Spectral signatures of materials dominantly covering the Earth's surface in METU campus. Particular spectral bands corresponding to atmospheric absorption windows have been removed from the plot due to the low signal-to-noise ratio (SNR).

tromagnetic spectrum with non-overlapping and consecutive observation channels. Thus, hyperspectral imaging enables achieving higher success in the discrimination and identification of the matters in a given scene with respect to their spectral features as compared to other spectral imaging techniques.

2.2 Working Principles of Hyperspectral Remote Sensing Systems

This subsection of the thesis is devoted to scrutinizing how hyperspectral remote sensing systems generate such qualified imagery that enables detailed information regarding the chemical and physical (i.e., texture and shape) structures of the matters in the scene by achieving high resolution in both spatial and spectral domain. In this context, hyperspectral remote sensing systems are reviewed according to design principles that determine how the target surface is imaged in spatial and spectral domains.

Spatial Scanning

Considering the number of pixels acquired at a time in each spatial dimension, three common approaches in hyperspectral remote sensing system design are illustrated in Figure 7. Whisk-broom systems, a.k.a. across-track or spotlight scanners, use a single detector and acquire one pixel at a time by means of a rotating mirror. As soon as one particular pixel is acquired, the rotating mirror looks at the target surface from a different angle to acquire the neighboring pixel(s). On the other hand, push-broom systems, a.k.a. along-track scanners, scan the target surface using a single-dimensional array of detectors, which can acquire one line of pixels at a time as the imaging system moves along the flight direction. The hyperspectral imaging systems in the third group are called snapshot (a.k.a. framing or staring) designs that are able to acquire multiple pixels in each spatial dimension at a time using a two-dimensional array of detectors without any need to scan the target surface by means of the movement of the imaging system.

The most remarkable advantage of whisk-broom design over other hyperspectral imaging system designs is the less number of detectors to be kept radiometrically calibrated. However, the moving parts of the whisk-broom design make these systems more complex and vulnerable. As a variant of the whisk-broom design, push-broom is the most common hyperspectral imaging payload design used for airborne and satellite platforms. Push-broom systems cover a wider area on the target surface than whisk-broom design. Accordingly, push-broom systems look at a particular area on the ground for a longer period of time than whisk-broom systems, which ensures higher exposure time and SNR performance. However, since each individual element of the detector array has different spectral response characteristics, they must be calibrated. Otherwise, uncalibrated individual detectors may cause stripes on the resulting image. On the other hand, snapshot design allows acquiring multiple pixels along each spatial dimension simultaneously. Similar to push-broom design, snapshot design requires calibration of each detector array element. In addition to that, 2D fo-

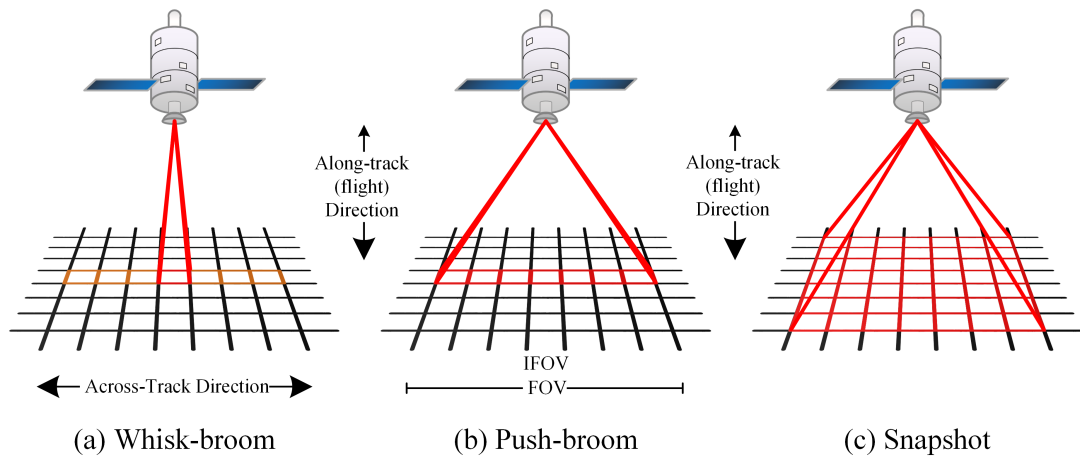


Figure 7: Common hyperspectral remote sensing system design approaches.

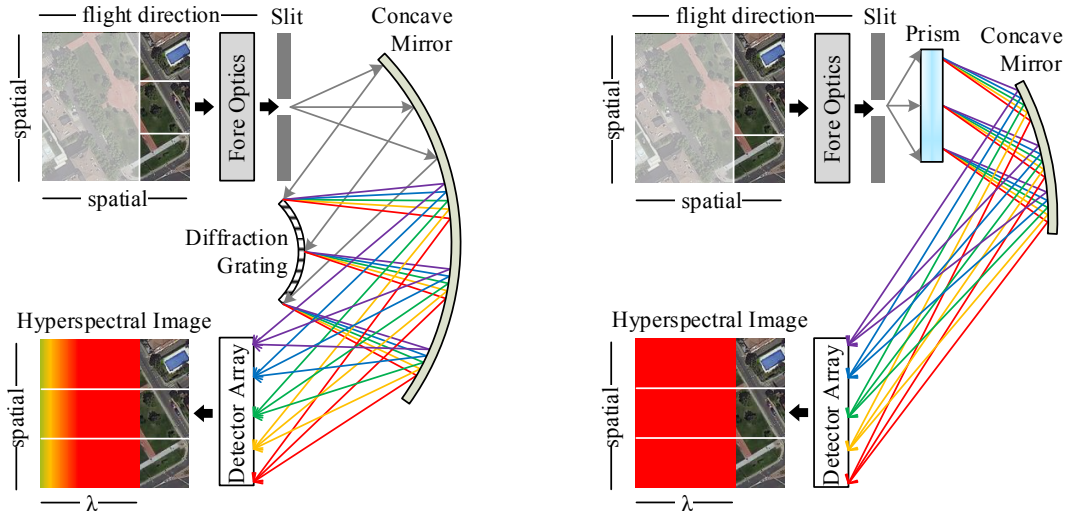
cal plane arrays that are used in snapshot systems offer limited spectral sensitivity and provide less spectral resolution as compared to other system designs.

It is also worth noting that the spatial dimension of the image acquired by a whisk-broom or push-broom system in an across-track direction is defined by the rotation range of the mirror and the number of detectors in the sensor array, respectively. On the other hand, these systems can acquire the desired amount of pixels (scan lines) in the second spatial dimension along the flight direction. Despite the snapshot design allowing acquiring multiple pixels in two dimensions, the spatial dimensions of the resulting image are limited to a number of sensors on the detector array.

Spectral Selection

Yet another key point distinguishing hyperspectral remote sensing systems is the spectral selection technique that enables imaging of the target scene at consecutive and non-overlapping wavelengths with high resolution in the spectral domain to build a hyperspectral data cube. There are three common spectral selection techniques adopted in hyperspectral remote sensing system design: 1) separating the electromagnetic radiation reaching from the target surface into different wavelengths using a dispersing element, 2) consecutively imaging the target surface at different wavelengths in a snapshot manner in the time domain using a tunable band-pass filter, 3) quantifying the electromagnetic radiation at a specific wavelength at a time using a moving beam splitter based design called interferometer to form the hyperspectral imagery.

Hyperspectral remote sensing systems adopting the first approach use a *diffraction grating* or *prism* based *dispersing element* that separates the electromagnetic radiation reaching from the target surface into different wavelengths (please see Figure 8). Subsequently, the dispersed electromagnetic radiation for a certain spot or spatial scan line is reflected on a single detector or an array of sensitive detectors in a particu-



(a) Diffraction grating-based spectral selection

(b) Prism based spectral selection

Figure 8: Dispersion unit based spectral selection designs.

lar spectral region of interest. Accordingly, the amount of energy reflected or emitted by the matter(s) present within the IFOV of the imaging system is quantified at different wavelengths. These spectral selection approaches are used in whisk-broom and push-broom designs in which the system disperses the electromagnetic radiation from the target surface, builds up the image as the imaging system moves through the along-track direction, and scans succeeding lines.

The second spectral selection technique used in hyperspectral imaging system design is the *tunable filter* that enables imaging of the target surface at different wavelengths in the time domain. In other words, the adjustable band-pass filter used in the design allows a certain frequency of incoming electromagnetic radiation from the target surface to reach the detector array and blocks other frequencies depending on the given input voltage. Accordingly, detectors quantify incoming radiation from the target surface at a specific frequency for all the spatial pixels concurrently. The same process is repeated in the time domain for the other frequencies (i.e. wavelengths) by adjusting the filter's passband for acquiring the other observation channels to form the hyperspectral image. This spectral selection technique is broadly used in snapshot hyperspectral imaging system design that ensures the time required to adjust the tunable filter to form the hyperspectral image. Despite the snapshot system design enabling imaging of the target surface in two spatial dimensions, the tunable filters in front of the detector arrays suffer from some drawbacks, such as low throughput, low spectral resolution, and limited spectral coverage.

Hyperspectral remote sensing systems in the third group perform spectral selection using an optical design called *interferometer*. As illustrated in Figure 10, an interferometer splits the incoming electromagnetic radiation reaching from the target surface into two separate beams to create an optical path difference (OPD) between them. In

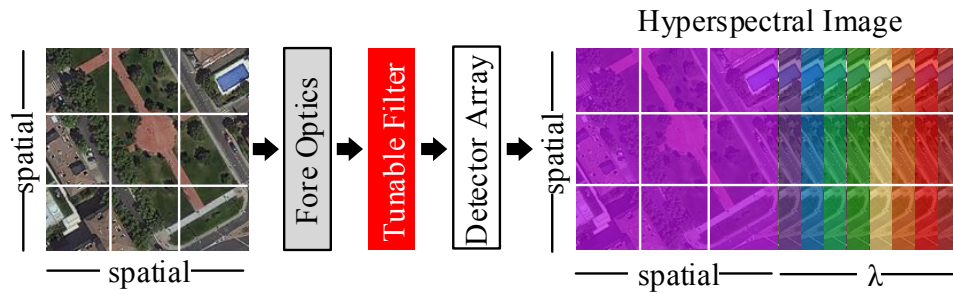


Figure 9: Tunable filter based spectral selection design.

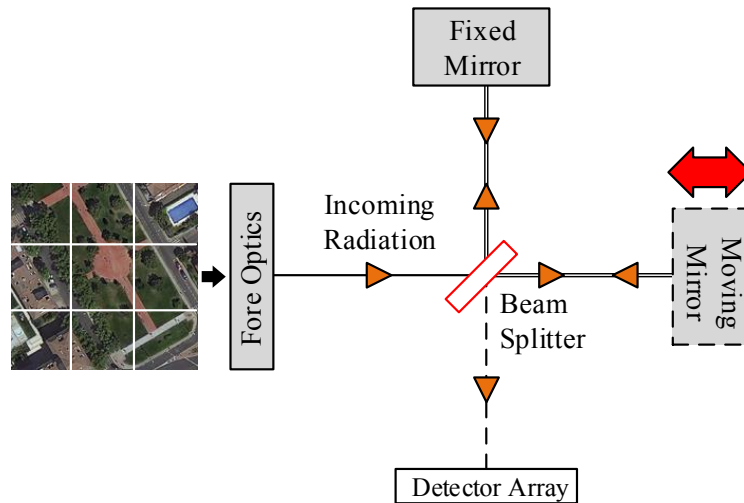


Figure 10: Michelson interferometer.

the next step, two beams are reflected back to interfere with the beam-splitter, and a combination of the two beams called an interferogram, is measured by the detector. In order to generate the OPD, one of the two beam's phases is altered before the interference. The phase difference between two beams caused by the OPD either strengthens or attenuates the resulting interferogram. In other words, the resulting interferogram gets brighter as the phases of two beams are closer. Similarly, the interferogram is attenuated as the phase shift between two beams increases. In the final step, the interferogram obtained in the spatial domain as a result of the continuous movement of the mirror is converted to the frequency domain by applying the Fourier Transform. Accordingly, the interferogram is decomposed into frequency components, and each individual frequency in the incoming electromagnetic radiation reaching from the target surface can be quantified. Michelson and Sagnac are the most common interferometer designs used in hyperspectral remote sensing systems.

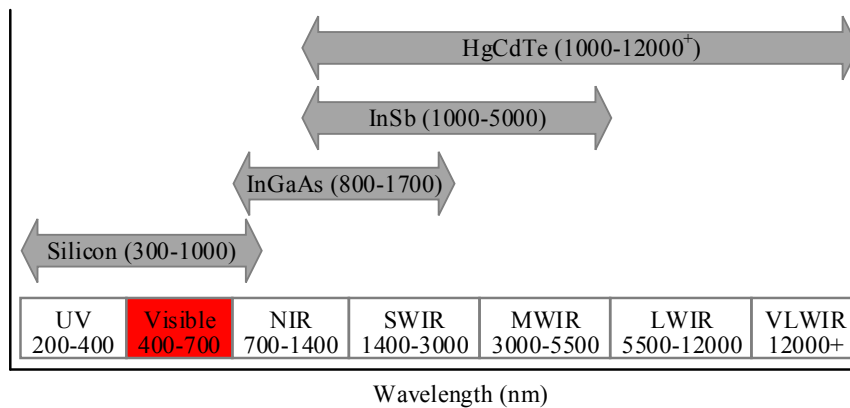


Figure 11: Spectral regions and corresponding detector materials.

Detector Materials

Hyperspectral imaging is performed in a broad section of the electromagnetic spectrum (i.e., 100 nm to 12+ μm) that covers ultraviolet, visible, near-infrared, and thermal infrared regions. However, depending on the spectral region in which the imaging is carried out, passive optical remote sensing systems need to employ different detectors manufactured with specific materials sensitive to particular spectral regions. The underlying reason for employing different imaging detectors is the dynamic sensitivity of the materials used in the detectors in different spectral regions. The spectral sensitivity of the detector materials is either defined by the *quantum efficiency* or the *spectral response*. The quantum efficiency of a detector material is the ratio of the incident photon to the converted electron as a function of the wavelength. Similarly, the spectral response defines the sensitivity of the sensor material to incoming radiation as a function of the wavelength (please see Figure 4). Figure 11 presents commonly used detector materials in hyperspectral imaging systems and the spectral ranges where the materials show sufficient spectral sensitivity characteristics for detector production.

2.3 Hyperspectral Remote Sensing Systems

Hyperspectral remote sensing of diverse surfaces (e.g., earth, lunar, or planetary) has been performed using instruments carried on low or high-altitude platforms since the early 1980s. Depending on the requirements of the imaging campaign (e.g., periodicity, distance to target surface, spatial resolution, spectral region, etc.), hyperspectral remote sensing systems perform image acquisition either on spaceborne (satellites or space stations) or airborne (manned or unmanned aircraft) platforms. This section of the thesis is devoted to 1) presenting a comprehensive review of the hyperspectral imaging systems used in the history of remote sensing and 2) drawing attention to

the necessity of novel CBHIR systems considering the volume and diversity of image archives generated by these instruments.

2.3.1 Airborne Systems

The history of hyperspectral remote sensing systems flying on low and medium-altitude airborne platforms began in 1982 with the deployment of the National Aeronautics and Space Administration/Jet Propulsion Laboratory's (NASA/JPL) 128-band SWIR (900-2400 nm) Airborne Imaging Spectrometer-1 (AIS-1) instrument [13]. In the following years, NASA/JPL has developed succeeding hyperspectral imaging systems Airborne Imaging Spectrometer-1 (AIS-2) [13], Advanced Solid-state Array Spectroradiometer (ASAS) [14], and Airborne Visible Infrared Imaging Spectrometer (AVIRIS) [15], which operate in either VNIR or VNIR-SWIR regions of the electromagnetic spectrum. Among these, AVIRIS has been a well known instrument that acquires 224 band hyperspectral imagery of the Earth's surface in VNIR-SWIR (400-2450 nm) region. The AVIRIS archive, continuously updated since 2006 with gigabytes of new hyperspectral images, is available at AVIRIS Data Portal [16]. Consequently, hyperspectral images acquired by AVIRIS have been used by researchers in a wide range of fields, e.g., geology, land management, agriculture, and atmospheric studies, to solve diverse problems.

Since the beginning of 1990s, numerous governmental or non-governmental initiatives have also started to develop and deploy hyperspectral remote sensing systems. For instance, Hyperspectral Digital Imagery Collection Experiment (HYDICE) by Hughes Danbury Optical Systems (HDOS) [17, 18], Système Spectro-Imageur de Mesure des Propriétés Hyperspectrales Embarqué (SYSIPHE) by The French Aerospace Lab (ONERA) [19], TRW Imaging Spectrometer (TRWIS) A-B-II-III by TRW TRWIS-A [13, 20, 21], Advanced Airborne Hyperspectral Imaging System (AAHIS) by Sets Technology [22], Airborne Hyperspectral Scanner (AHS) by Daedalus Enterprise Inc. [13], Digital Airborne Imaging Spectrometer (DAIS) & Reflective Optics System Imaging Spectrometer (ROSIS) by German Aerospace Center (DLR) [23, 24], Spatially Modulated Imaging Fourier Transform Spectrometer (SMIFTS) by University of Hawaii [13], Airborne Real-time Cueing Hyperspectral Enhanced Reconnaissance (ARCHER) by US Air Force [25], COMPASS by the US Government [26], Compact Airborne Spectrographic Imager (CASI) by ITRES [27], and SEBASS by Aerospace Corp. [28, 29] pioneered airborne hyperspectral remote sensing systems developed for different purposes. Due to the common drawbacks of the systems (i.e., size, weight, and storage requirements) and the lack of unmanned platforms offering enough payload capacity, all these hyperspectral remote sensing systems were only able to operate on manned aircraft platforms (e.g., Lockheed ER-2, Convair CV-580, GippsAero GA8, Cessna 208). In 2019, Visratek and Headwall Photonics jointly developed and deployed yet another VNIR-SWIR (400-2500 nm) very high-resolution airborne hyperspectral imaging system in Turkey for medium-altitude flights that offers fully autonomous mission control and configuration.



Figure 12: ARCHER hyperspectral remote sensing system installed on GippsAero GA8 [30].

In the 2000s, advances in optics, electronics, and computing technologies have led to the development of new-generation hyperspectral remote sensing systems. This evolution has been mostly observed in increasing spectral and spatial resolutions versus reducing the dimensions and weights of the instruments. For instance, the Nano-Hyperspec (400 nm - 1000 nm) 270 band / 640 pixel VNIR push-broom hyperspectral imager, which was designed for small Unmanned Aerial Vehicles (UAV), developed by Headwall Photonics weight less than 650 gr, including a data storage unit. Therefore, in addition to manned aircraft, hyperspectral imagers have found a chance to fly on alternative platforms, i.e., single-rotor, multi-rotor, or fixed-wing UAVs. Accordingly, this progress has led to the mass deployment of hyperspectral imaging systems in a short time for different purposes ranging from precise detection of plant disease to buried explosive detection.

On the other hand, mass deployment of these systems causes the emergence of diverse hyperspectral imagery collections to be stored and processed. For instance, the above-stated hyperspectral remote sensing system (Nano-Hyperspec) acquires hyperspectral imagery of a ~ 32 km² area in 60 minutes on a multi-rotor UAV flying (Figure 13) at 500 m altitude with 57,6 km/h of cruise speed. Such a flight results in over 29 gigabytes of raw hyperspectral image data. Accordingly, effective management of the hyperspectral image collections and rapid access to the desired information in these collections have become an important issue as these systems become more widely used.



Figure 13: Nano-Hyperspec hyperspectral remote sensing system installed on DJI M600 Pro UAV.

Appendix A presents a comprehensive list of the hyperspectral imaging systems developed for airborne applications by providing their technical and operational specifications.

2.3.2 Spaceborne Systems

Subsequent to successful imaging campaigns performed with airborne platforms, hyperspectral remote sensing systems have been also deployed with satellite missions for different purposes. In 1997, NASA successfully launched the first satellite mission equipped with a hyperspectral remote sensing instrument. Interferometer-based push-broom hyperspectral payload on the LEWIS mission observed the Earth's surface in the VNIR-SWIR (400 nm - 2500 nm) region with 384 discrete spectral channels. It is worth noting that the imager was not the first hyperspectral imaging system development initiative for a spaceborne mission [31]. Priorly, NASA, European Space Agency (ESA), and Commonwealth Scientific and Industrial Research Organisation (CSIRO) initiated three unachieved spaceborne hyperspectral imaging system development projects named HIRIS [32, 33], HRIS [34], and ARIES [35], respectively.

In 2000, two successful satellite missions MightySat II and EO-1 were launched by USAF and NASA, respectively. MightySat II was launched with an interferometer-based push-broom payload named FTHSI, which could acquire 256-band hyperspectral imagery in the VNIR (400 nm - 1000 nm) region [36]. On the other hand, NASA's multi-payload EO-1 mission was launched with a grating-based 220 band push-broom VNIR-SWIR (400 nm - 2500 nm) hyperspectral remote sensing instrument named Hyperion [37]. Since NASA has made all EO-1 mission payload data freely available to download on the Earth Explorer web portal [38], Hyperion's historical archive has been the first and ever-growing publicly available hyperspectral image resource for researchers. Moreover, the EO-1 mission has allowed individuals and organizations to issue data acquisition requests to have hyperspectral imagery of a specific area in one of the next possible re-visits if the area lies within the coverage of the satellite. Consequently, Hyperion hyperspectral imagery has been extensively used for various applications ranging from mineral mapping to water quality assessment. The EO-1 mission was decommissioned in 2017, but all historical image archives are still accessible on the Earth Explorer portal.

The following year, ESA successfully launched a Project for On-Board Autonomy (Proba) mission carrying Compact High-Resolution Imaging Spectrometer (CHRIS) VNIR (415 nm - 1050 nm) hyperspectral imaging payload [39, 40]. Unlike the hyperspectral instruments on the previous satellite missions, images acquired by CHRIS are composed of either 18 or 62 spectral bands depending on targeted spatial resolution. Like Hyperion, ESA allows access to CHRIS historical hyperspectral image archive at Earth Online web portal [41].

In addition to space missions that aim to acquire hyperspectral imagery of the Earth's surface, other successful missions have observed planetary or lunar surfaces with hyperspectral instruments. Mars Reconnaissance Orbiter (MRO) was launched in 2005



Figure 14: EO-1 Mission and a false-color representation of a hyperspectral image acquired by Hyperion payload [42].

by NASA and John Hopkins University to search for mineralogical evidence of water on Mars with Compact Reconnaissance Imaging Spectrometer for Mars (CRISM) hyperspectral imaging system. CRISM is a grating-based VNIR-SWIR-MWIR (400 nm - 3900 nm) hyperspectral imaging system that observes the surface of Mars at 544 distinct spectral channels.

Two years later, China launched Chang'e-1 mission to observe the Moon's surface with Interference Imaging spectrometer (IIM) hyperspectral remote sensing system [43, 44]. The IIM instrument on Chang'e-1 acquired 32-band hyperspectral imagery of the Moon's surface with 25.6 m of spectral resolution from a 200 km lunar orbit. The space missions to obtain hyperspectral imagery of the Moon's surface have continued with Indian Space Research Organisation's (ISRO) Chandrayaan-1 satellite. The mission was launched with two hyperspectral imagers named HySI [45, 46] and M³ [46, 47], which were sensitive in VNIR (421-964 nm) and VNIR-SWIR-MWIR (400 nm - 3000 nm) regions, respectively.

In 2008, China launched another satellite mission with a hyperspectral imaging instrument to observe the Earth's surface. The HIS payload on the HJ-1 satellite is an interferometer-based instrument and is able to acquire hyperspectral imagery at 115 distinct spectral channels in the VNIR (459 nm - 956 nm) region [48, 49].

Along with civil usage, hyperspectral imagery has been extensively utilized in defense and security applications. The Tactical Satellite-3 (TacSat-3), launched in 2009 by the United States Department of Defense (DoD), is a military-purpose hyperspectral

imaging mission. Grating based Artemis instrument on TacSat-3 has acquired 400 bands hyperspectral imagery in VNIR and SWIR (400 nm - 2500 nm) region [50, 51].

Satellites are not the only platforms that orbit in space with hyperspectral instruments. In 2011, China National Space Administration (CNSA) integrated a hyperspectral imaging system into the Tiangong-1 space station. The HIS instrument on Tiangong-1 acquired 128 bands of hyperspectral imagery of the Earth's surface in VNIR and SWIR (400 nm-2500 nm) regions [48, 49]. It has been known that DLR also carries out a project to integrate push-broom DLR Earth Sensing Imaging Spectrometer (DESI) hyperspectral imaging instruments into the ISS [52, 53, 54]. In December 2019, the Hyperspectral Imager Suite (HISUI) mission of Japan Space Systems with two Micro-Hyperspec series hyperspectral imagers (VNIR and SWIR) developed by Headwall Photonics launched by Space X's Dragon spacecraft to ISS [55, 56]. The system delivers hyperspectral imagery with 185 spectral channels over a 20 km swath width with 20 x 30 meter spatial resolution.

Apart from large-scale satellites and space stations, cubesats have also been used for spaceborn hyperspectral imaging missions in the recent years. For instance, Greenhouse Gas Satellite (GHGSat) launched Claire's mission in 2016 to observe greenhouse and air quality gas emissions with a VNIR hyperspectral instrument. The Micro-Hyperspec instrument on Claire is sensitive in the VNIR (400-1000 nm) region and acquires 325 bands of hyperspectral imagery [57, 58, 59].

In addition to the aforementioned spaceborne missions that are either on duty or expired for various reasons, other satellite missions with hyperspectral imaging payloads are in the design or production phase.

2.4 Review of Hyperspectral Remote Sensing Applications from a Content-Oriented Point of View

Thanks to incomparable dense spectral information provided by hyperspectral imaging systems regarding the matters that constitute a scene, images acquired with those systems have been used in various remote sensing applications. This section of the thesis is dedicated to scrutinizing the utilization of hyperspectral remote sensing imagery in diverse applications from a content-oriented point of view by providing real-life application examples.

2.4.1 Land-Use Mapping / Classification

One of the principal applications that utilize hyperspectral remote sensing imagery is the precise mapping of land use. Ranging from understanding the Earth's ecosystem to city or regional planning, accurate and up-to-date classification of land-cover types provides quantitative information regarding how a particular region of the Earth is fragmented either naturally or in a planned manner into diverse sections (urban area, agricultural area, forest, water bodies etc.) for different purposes.



Figure 15: Land-use mapping results of classification method proposed in [1] in study area 1.

Since very dense spectral and spatial information provided by hyperspectral imagery allows accurate discrimination of matters in a scene, a remarkable number of methods have been proposed in the literature for land-use classification. A novel approach proposed in [60] performs multi-label land-use classification in hyperspectral imagery. In [1], authors proposed a framework for land-use classification that combines spectral, shape, and texture features extracted from hyperspectral imagery with height features from Digital Surface Models (DSM). Yet another study that proposes an alternative land-use mapping method combines hyperspectral imagery with LiDAR data to improve classification accuracy [61].

Accordingly, a proper CBHIR system may allow decision-makers to accurately access desired hyperspectral imagery in a certain archive using a query that embodies/represents spectral features of similar land-use classes.

2.4.2 Environmental Monitoring

Environmental monitoring is another remote sensing application that intensively benefits from hyperspectral imagery. As a broad definition, environmental monitoring describes activities performed to observe change and quality of the environment and includes, but is not limited to, land monitoring and coastal/oceanic monitoring for different purposes such as change detection, risk assessment, or post-disaster management.

A method for mapping the thickness of oil spills using hyperspectral imagery was proposed in [2]. The proposed method was verified with AVIRIS hyperspectral imagery acquired in the Gulf of Mexico on May 17, 2010, over the Deepwater Horizon oil spill disaster area. As shown in Figure 16, high-resolution spectral imagery allows accurate mapping of oil spill spread and thickness. In [62], hyperspectral remote sens-

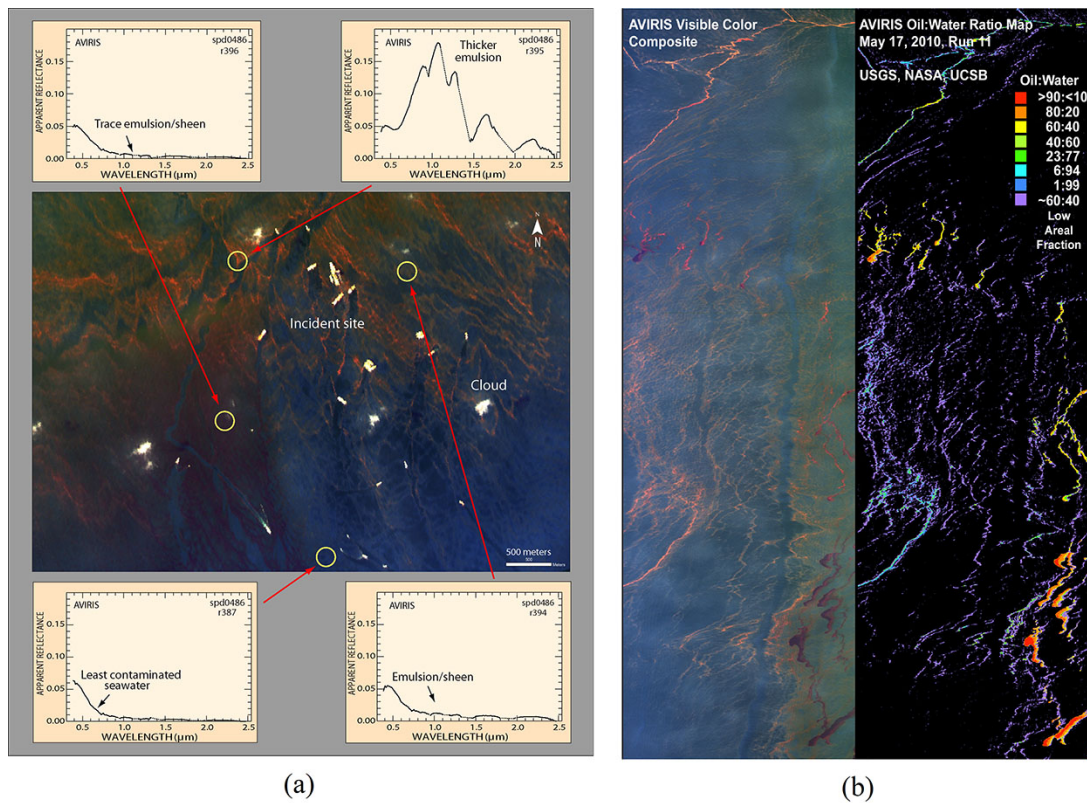


Figure 16: AVIRIS visible-color composite image and example signatures from oil-spill disaster area [2].

ing imagery has been used to near-real-time monitor the formation of algal blooms, which are toxic to human health and the ecosystem, in Lake Erie. In [63], off-nadir hyperspectral imagery acquired by CHRIS/PROBA platform was used to map tropical dry forest succession in Brazil.

In [64], a novel unsupervised change detection method for multi-temporal hyperspectral imagery was proposed. The proposed method focuses on change in each individual band of hyperspectral images and creates hyperspectral change vectors using this information. Yet another method that aims at detecting changes in multi-temporal hyperspectral remote sensing imagery using sparse unmixing was proposed in [3] and verified using real and synthetic data sets.

Despite hyperspectral remote sensing imagery being widely used for detecting changes originating on the Earth's surface, it has also been used for real-time risk-assessment purposes such as detecting or monitoring hazardous matters. In [65], an airborne hyperspectral imaging system, which operates between $3.3 \mu\text{m}$ and $5.4 \mu\text{m}$, was introduced for industrial emissions monitoring.

Fast and accurate access to hyperspectral images embodying critical content is important for monitoring, early response, and risk assessment. Thus, a proper CBHIR

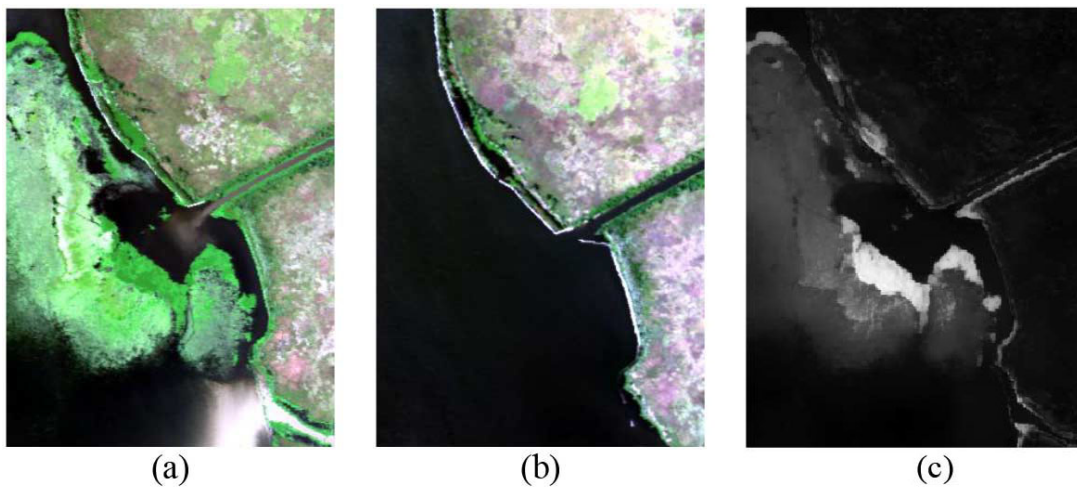


Figure 17: Multi-temporal hyperspectral imagery acquired over New Orleans (a) September 2010, (b) October 2011, and (c) change detection map generated by the method proposed in [3].

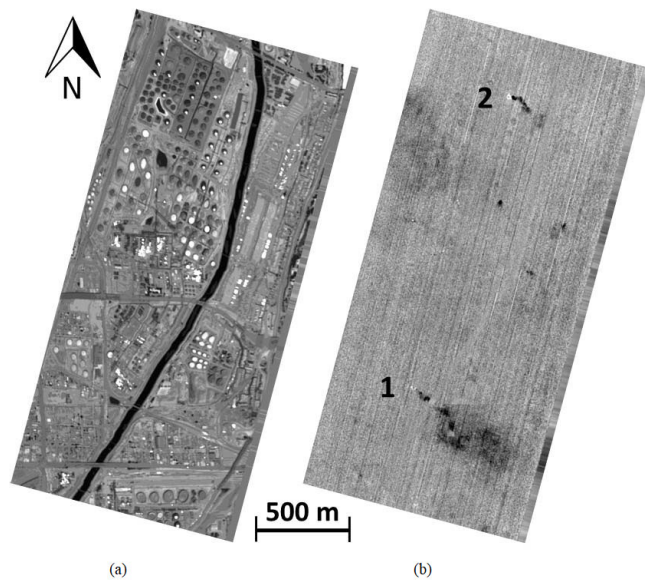


Figure 18: (a) Thermal image of a segment of the Long Beach industrial corridor (b) CO ACE detection image [65].

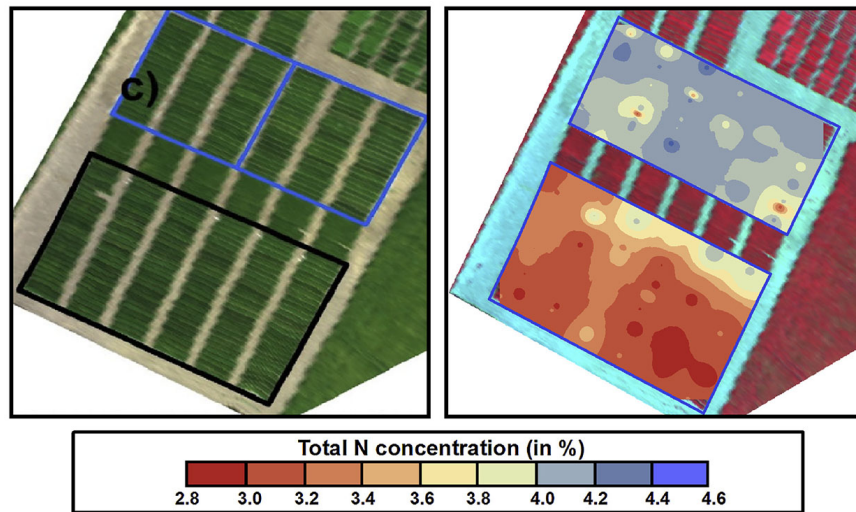


Figure 19: Plant nitrogen retrieval map generated by the method proposed in [4].

system may contribute to more effective usage of hyperspectral imagery in environmental monitoring.

2.4.3 Precision Agriculture and Forestry

Considering the continuous increase in demand on fruitful food resources around the World, precision agriculture (or farming) gains more importance with each passing day. Ranging from crop disease mapping to yield assessment, precision agriculture has been intensively using spectral remote sensing imagery for decades. Measured energy reflecting from agricultural fields at specific wavelengths provides useful information regarding plant diversity, health, soil moisture, and fruitfulness. Thus, hyperspectral imagery is a useful data resource for precision agriculture-related applications. Beyond that, recent developments in imaging technology enable acquiring hyperspectral imagery at very high resolution that allows analysis of leaves or fruits of each individual plant in the field.

In [66], a method was proposed for mapping sugarcane plants infected with mosaic virus in hyperspectral imagery acquired with a UAV platform. In [67], the winter wheat leaf area index is estimated in airborne hyperspectral imagery using vegetation indices. Yet another study on winter wheat plants proposed optimized spectral indices for mapping powdery mildew, yellow rust, and aphid diseases [68]. In [4], nitrogen retrieval of plants after water, which is an important factor that limits crop yield, is studied on VNIR and SWIR hyperspectral imagery (see Figure 19). A method proposed in [69] enables the generation of spectral-temporal response surfaces for precision agriculture applications using hyperspectral imagery.

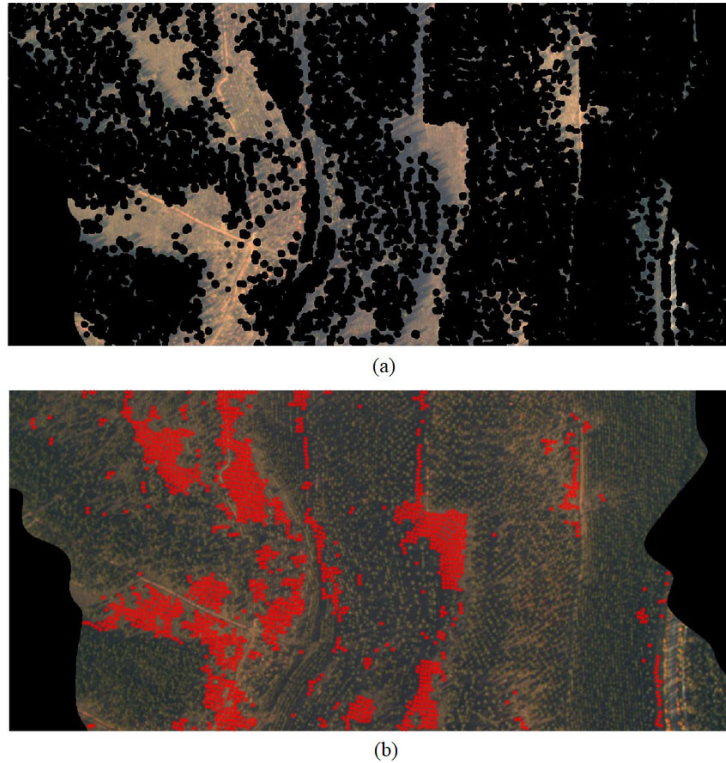


Figure 20: (a) Detection of afforested areas, (b) estimated positions of new trees to be planted [5].

Precision forestry is another application that utilizes dense spectral information provided by hyperspectral remote sensing imagery for effective forest management. In [5], a supportive method was proposed for the afforestation planning process of partially forested areas. The proposed semi-supervised method identifies afforested regions in airborne hyperspectral imagery and estimates proper locations for new trees considering the canopy area of the mature plant (see Figure 20). In [70], a method for fusing hyperspectral imagery and LiDAR data for forest monitoring in the southwestern United States was proposed.

All these studies and methods mainly benefit from certain differences in spectral signatures of matters (i.e., plant species, diseases, or pests) that constitute hyperspectral imagery acquired over an agricultural or forested area. Considering the acreage of those areas, an accurate CBHIR system may enhance the effectiveness of hyperspectral imagery in precision agriculture and forestry, such as detecting infected plants or locating certain types of trees that show similar spectral characteristics with plants in a given query image.

2.4.4 Mineralogy and Geology

Mineralogy and geology is another field that intensively uses spectral information for various purposes ranging from drill core analysis to mapping mineral deposits. The dense spectral information provided by hyperspectral imagery enables the identification of minerals due to energy reflection or absorption characteristics they possess at specific wavelengths. Beyond that, accurate identification of critical (e.g., alteration) minerals has also been used to localize deposits [6]. Since distinctive spectral features of minerals and rocks are mainly observed at wavelengths that lie beyond the visible range, mineralogy and geology applications often benefit from infrared hyperspectral remote sensing imagery.

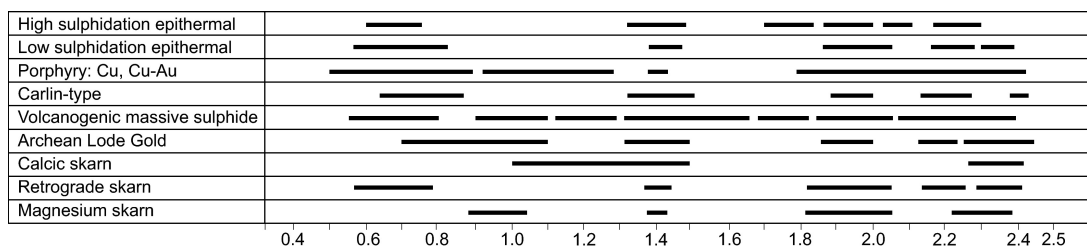


Figure 21: Summary of the main deposit types in relation to areas in the spectrum (indicated by the bars) where absorption occurs related to the presence of key alteration minerals [6].

There have been many studies related to mineral mapping proposed in the literature. Hydrothermal alteration mapping of Bodie, California, was performed using AVIRIS hyperspectral imagery in [71]. In [72], the performance of an airborne (AVIRIS) and a spaceborne (EO-1 Hyperion) hyperspectral imaging system is compared for mineral mapping. Yet another mineral mapping method that used thermal hyperspectral imagery was proposed in [73]. The effect of improving the spatial resolution of hyperspectral imagery for mineral mapping was discussed in [74]. EnMAP Geological Mapper (EnGeoMAP) 2.0 algorithm was proposed in [7] for automated hyperspectral mineral identification (see Figure 22). In [75], a novel workflow for volcano mapping and monitoring that integrates hyperspectral imaging with LiDAR was proposed. In [76], a novel feature extraction method was proposed for mining area classification in hyperspectral remote sensing imagery.

In addition to mineral mapping, hyperspectral imagery has been used to map hydrocarbons, the main constituents of oil and natural gas. In [77], an algorithm for hyperspectral detection of hydrocarbons called the Hydrocarbon Index was proposed. The author reviews oil-gas reservoir detection approaches using hyperspectral remote sensing imagery in [78].

Considering the benefits of spectral information in detecting and identifying minerals, a proper CBHIR system might be a useful tool for mineralogy and geology applications in terms of rapid and accurate access to hyperspectral images with minerals showing similar spectral characteristics with a given query.

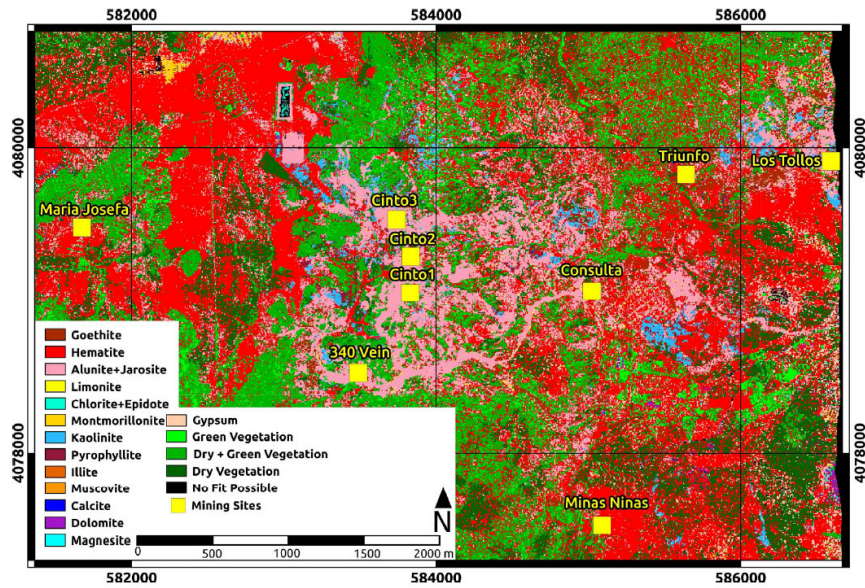


Figure 22: Material map of EnGeoMAP 2.0 calculated from airborne HyMAP data [7].

2.4.5 Defense and Security

Since chemical fingerprints called spectral signatures of the matter allow rapid and remote detection and identification, defense and security applications also intensively benefit from hyperspectral imagery. Utilization of hyperspectral imagery in defense and security can be categorized under two groups: 1) signature-based detection applications and 2) anomaly detection applications [79].

Signature-based detection aims to determine the existence of a phenomenon (i.e., any target, clue, or residual) in a scene by pair-wise matching spectral signatures of known matters (namely spectral library) with image pixel signatures either at the pixel or sub-pixel level. To this end, the proposed methods in the literature mainly use spectral distance or matched filter-based approaches. In [8], a constrained energy maximization-based military camouflage detection method is proposed (see Figure 23). A linear unmixing-based sub-pixel target detection workflow is presented in [80]. A supervised metric learning-based sub-pixel target detection method is proposed in [81]. In [82], an airborne hyperspectral imaging system is introduced for detecting gaseous and solid targets. In [83], a novel method for detecting targets using sparse representation of hyperspectral image is proposed. In [84], sparse transfer manifold embedding (STME) is introduced for encoding discriminating features of the targets in hyperspectral imagery to increase detection performance.

On the other hand, anomaly detection aims at finding suspicious image pixels whose spectral characteristics are extraordinarily different than surrounding pixels in an image. One of the most well-known anomaly detection algorithms for multi-band imagery called Reed-Xiaoli (RX) was published in [85] and performance of the original

method was enhanced by other studies, i.e., [86, 87], in the course of time. In [88], a method was introduced for detecting buried objects in thermal infrared imagery. A novel method that fuses hyperspectral imagery with high-resolution multispectral imagery for target detection is proposed in [89]. A comprehensive review of landmine detection methods using hyperspectral imagery can be found in [90]. An algorithm that detects vehicles in shadow areas using hyperspectral and LiDAR data is introduced in [91].

Even if the pure spectral signature of the target does not exist or the featured spectral characteristics of the target are not known, a proper CHBIR system may allow easy and fast access to hyperspectral images with similar matters whose spectral characteristics are defined by the query image.

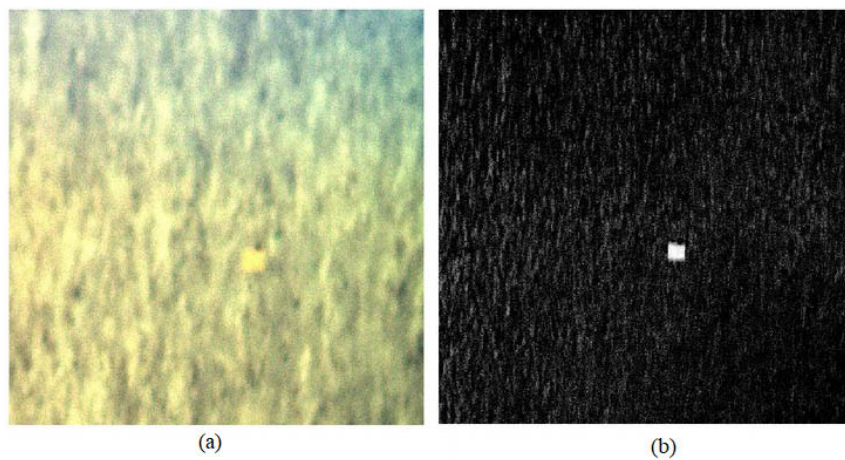


Figure 23: (a) RGB composite image of the data set, (b) Camouflage detection result [8].

CHAPTER 3

RELATED LITERATURE

This chapter of the thesis is dedicated to presenting a comprehensive review of literature related to content detection and content-based retrieval in hyperspectral imagery. The following subsections elaborate on the related literature in a systematic way by scrutinizing methods in line with CBHIR strategies defined in Table 1, such that content detection and retrieval methods are grouped with respect to the type of query: single material or multiple materials.

3.1 Single Material Based Content Detection Methods for Hyperspectral Imagery

Single material-based content detection in hyperspectral imagery refers to the process of searching a given query signature \mathbf{x}_q through image pixels \mathbf{x}_n of all hyperspectral images \mathbf{X}_n in an archive \mathbf{X} and considered as a binary hypothesis test:

$$H_0: \text{Content absent}$$
$$H_1: \text{Content present}$$

The detection process is performed either at full-pixel or sub-pixel level. In full-pixel level content detection, phenomena represented by the query signature are searched through image pixels of \mathbf{X}_n , assuming each image pixel belongs to one class. Sub-pixel level content detection, on the other hand, assumes that pixel signatures of \mathbf{X}_n might originate in a mixture of one or more material classes due to low spatial resolution of the imager or other external parameters, i.e., multiple scattering of the incident light, as explained in Section 3.2. Thus, \mathbf{x}_q must be searched through all \mathbf{x}_n as a resulting mixture component or as an interfered form of its original form.

Finally, a CBHIR system retrieves the images with pixel(s) that satisfy H_1 considering the user-defined threshold.

3.1.1 Full-Pixel Content Detection Algorithms

The full-pixel content detection algorithms calculate one-by-one similarity between given query signature \mathbf{x}_q and image pixel signatures \mathbf{x}_n of an archive image \mathbf{X}_n . In case \mathbf{X}_n has one or more pixels that satisfy H_1 with respect to a user-defined threshold, \mathbf{X}_n is considered as an image that covers material depicted by the query spectral signature. The following sub-sections discuss details of full-pixel content detection algorithms that are widely used in the literature.

Spectral Angle Mapper (SAM)

Spectral Angle Mapper is one of the most well-known and widely used content detection algorithms at full-pixel level in the literature that treats query signature \mathbf{x}_q and any image pixel \mathbf{x}_n of \mathbf{X}_n as two vectors and calculates the angle between them. Even though SAM is a simple and effective way to measure the similarity between two spectral signatures, the illumination-invariant nature of the method has often been criticized.

$$\text{SAM}_{(\mathbf{x}_q, \mathbf{x}_n)} = \cos^{-1} \left[\frac{\mathbf{x}_q^T \mathbf{x}_n}{\sqrt{(\mathbf{x}_q^T \mathbf{x}_q)} \sqrt{(\mathbf{x}_n^T \mathbf{x}_n)}} \right] \quad (1)$$

Spectral Correlation Mapper (SCM)

To overcome SAM's drawback of distinguishing correlation between two given spectral signatures, another full-pixel content detection algorithm called Spectral Correlation Mapper (SCM) was proposed in [92].

As defined in Equation [2], SCM calculates a similarity between given two signatures in the range of -1 and 1. The SCM approaches 1 as the correlation between channel values of \mathbf{x}_q and \mathbf{x}_n are higher. Similarly, as the correlation between channel values of \mathbf{x}_q and \mathbf{x}_n decreases, SCM approaches to -1.

$$\text{SCM}_{(\mathbf{x}_q, \mathbf{x}_n)} = \frac{\sum_{s=1}^S (\mathbf{x}_q^s - \bar{\mathbf{x}}_q) (\mathbf{x}_n^s - \bar{\mathbf{x}}_n)}{\sqrt{\sum_{s=1}^S (\mathbf{x}_q^s - \bar{\mathbf{x}}_q)^2 \sum_{s=1}^S (\mathbf{x}_n^s - \bar{\mathbf{x}}_n)^2}} \quad (2)$$

Spectral Information Divergence (SID)

Spectral Information Divergence (SID) is yet another well-known method to measure similarity between given two spectral signatures \mathbf{x}_q and \mathbf{x}_n . As a stochastic approach,

SID models two signatures as random variables with probability distributions. Initially, \mathbf{x}_q and \mathbf{x}_n are normalized to range [0,1] by applying equations 3 and 4 to calculate desired probability vectors \mathbf{q} and \mathbf{p} , respectively.

$$\mathbf{q}_s = \mathbf{x}_q^s / \sum_{s=1}^S \mathbf{x}_q^s \quad (3)$$

$$\mathbf{p}_s = \mathbf{x}_n^s / \sum_{s=1}^S \mathbf{x}_n^s \quad (4)$$

Then, SID is calculated as

$$\text{SID}(\mathbf{x}_q, \mathbf{x}_n) = D(\mathbf{x}_q|\mathbf{x}_n) + D(\mathbf{x}_n|\mathbf{x}_q) \quad (5)$$

where $D(\mathbf{x}_q|\mathbf{x}_n)$ and $D(\mathbf{x}_n|\mathbf{x}_q)$ are relative entropy of \mathbf{x}_q with respect to \mathbf{x}_n and vice versa, respectively and calculated as defined in equations 6 and 7.

$$D(\mathbf{x}_q|\mathbf{x}_n) = \sum_{s=1}^S \mathbf{q}_s \log(\mathbf{q}_s/\mathbf{p}_s) \quad (6)$$

$$D(\mathbf{x}_n|\mathbf{x}_q) = \sum_{s=1}^S \mathbf{p}_s \log(\mathbf{p}_s/\mathbf{q}_s) \quad (7)$$

Jeffries-Matusita Distance (JM)

Jeffries-Matusita Distance (JM) is yet another stochastic approach to enhance the illumination invariance nature of SAM while determining the similarity between \mathbf{x}_q and \mathbf{x}_n . Similar to SID, JM is calculated based on probability distributions of given two vectors (see Equations 3 and 4) as defined in equation 8.

$$\text{JM}(\mathbf{x}_n, \mathbf{x}_q) = \sqrt{\sum_{s=1}^S (\sqrt{\mathbf{q}_s} - \sqrt{\mathbf{p}_s})^2} \quad (8)$$

Hybrid Methods

Hybrid methods have been proposed in the literature to combine different content detection methods and overcome the drawbacks of their standalone usage.

In [93], SID-SAM method was proposed to combine deterministic SAM and stochastic SID as a new hyperspectral discrimination measure as defined in equation 9.

$$\text{SID-SAM}(\mathbf{x}_q, \mathbf{x}_n) = \text{SID}_{\tan}(\mathbf{x}_q, \mathbf{x}_n) \cdot \text{SID}_{\sin}(\mathbf{x}_q, \mathbf{x}_n) \quad (9)$$

where

$$\text{SID}_{\tan}(\mathbf{x}_q, \mathbf{x}_n) = \text{SID}(\mathbf{x}_q, \mathbf{x}_n) \cdot \tan(\text{SAM}(\mathbf{x}_q, \mathbf{x}_n)) \quad (10)$$

$$\text{SID}_{\sin}(\mathbf{x}_q, \mathbf{x}_n) = \text{SID}(\mathbf{x}_q, \mathbf{x}_n) \cdot \sin(\text{SAM}(\mathbf{x}_q, \mathbf{x}_n)) \quad (11)$$

Similarly, SID-SCM was defined in [94] by replacing SAM in SID-SAM. In [95], yet another hybrid method was proposed called JM-SAM as defined in equation 12.

$$\text{JM-SAM}(\mathbf{x}_q, \mathbf{x}_n) = \text{JM-SAM}_{\tan}(\mathbf{x}_q, \mathbf{x}_n) \cdot \text{JM-SAM}_{\sin}(\mathbf{x}_q, \mathbf{x}_n) \quad (12)$$

where

$$\text{JM-SAM}_{\tan}(\mathbf{x}_q, \mathbf{x}_n) = \text{JM}(\mathbf{x}_q, \mathbf{x}_n) \cdot \tan(\text{SAM}(\mathbf{x}_q, \mathbf{x}_n)) \quad (13)$$

$$\text{JM-SAM}_{\sin}(\mathbf{x}_q, \mathbf{x}_n) = \text{SID}(\mathbf{x}_q, \mathbf{x}_n) \cdot \sin(\text{SAM}(\mathbf{x}_q, \mathbf{x}_n)) \quad (14)$$

3.1.2 Sub-Pixel Content Detection Algorithms

Apart from full-pixel level content detection, some single material content detection problems in hyperspectral imagery require sub-pixel level analysis on the assumption that pixel signatures \mathbf{x}_n of any hyperspectral image \mathbf{X}_n may originate in as a combination of spectral signatures of multiple materials. This phenomenon may be caused by various reasons, e.g., insufficient spatial resolution of the imager, atmospheric effects, or multiple scattering of incident light from surrounding objects.

The following subsections of the thesis present a detailed review of sub-pixel-level content detection algorithms.

Generalized Likelihood Ratio Test

The Generalized Likelihood Ratio Test (GLRT) algorithm considers the sub-pixel level content detection problem as a Gaussian interference of other signatures (e.g.,

neighboring materials, atmospheric effects, or additive noise) to query spectral signature \mathbf{x}_q , where background covariance matrix Σ is known.

$$\text{GLRT}(\mathbf{x}_q, \mathbf{x}_n) = \frac{\left((\mathbf{x}_q - \bar{\mathbf{x}}_q)^T \Sigma^{-1} (\mathbf{x}_n - \bar{\mathbf{x}}_n) \right)^2}{\left((\mathbf{x}_q - \bar{\mathbf{x}}_q)^T \Sigma^{-1} (\mathbf{x}_q - \bar{\mathbf{x}}_q) \right) \cdot \left(1 + (\mathbf{x}_n - \bar{\mathbf{x}}_n)^T \Sigma^{-1} (\mathbf{x}_n - \bar{\mathbf{x}}_n) \right)} \quad (15)$$

Adaptive Cosine Estimator

As a derivative of GLRT, the Adaptive Cosine Estimator (ACE) is invariant to scaling of \mathbf{x}_q and \mathbf{x}_n and performs better content to background (or interference) separation as compared to GLRT.

$$\text{ACE}(\mathbf{x}_q, \mathbf{x}_n) = \frac{(\mathbf{x}_q^T \Sigma^{-1} \mathbf{x}_n)^2}{(\mathbf{x}_q^T \Sigma^{-1} \mathbf{x}_q) (\mathbf{x}_n^T \Sigma^{-1} \mathbf{x}_n)} \quad (16)$$

Matched Filter

Matched Filter (MF) is another widely used sub-pixel level content detection method that assumes both H_0 and H_1 have equal covariance matrix Σ .

$$\text{MF}(\mathbf{x}_q, \mathbf{x}_n) = \frac{(\mathbf{x}_q - \bar{\mathbf{x}}_q)^T \Sigma^{-1} (\mathbf{x}_n - \bar{\mathbf{x}}_n)}{(\mathbf{x}_q - \bar{\mathbf{x}}_q)^T \Sigma^{-1} (\mathbf{x}_q - \bar{\mathbf{x}}_q)} \quad (17)$$

Constrained Energy Minimization

Constrained Energy Minimization is yet another filter-based approach for sub-pixel level content detection that aims at minimizing the energy originating from the background while maximizing the output of queried content signature.

$$\text{CEM}(\mathbf{x}_q, \mathbf{x}_n) = \frac{\mathbf{x}_q^T \Sigma^{-1} \mathbf{x}_n}{\mathbf{x}_q^T \Sigma^{-1} \mathbf{x}_q} \quad (18)$$

Orthogonal Subspace Projection

Orthogonal Subspace Projection (OSP) is a two-step sub-pixel level content detection. In the first step, algorithms create an orthogonal subspace projection to eliminate non-content pixels. In the following step, OSP applies MF to maximize the energy of pixels containing query signature.

$$\text{OSP}(\mathbf{x}_q, \mathbf{x}_n) = \frac{\mathbf{x}_q^T \mathbf{P}_U^\perp \mathbf{x}_n}{\mathbf{x}_q^T \mathbf{P}_U^\perp \mathbf{x}_q} \quad (19)$$

where $\mathbf{P}_U^\perp = \mathbf{I}_{SxS} - \mathbf{U}\mathbf{U}^\#$ is the orthogonal subspace, \mathbf{U} and $\mathbf{U}^\# = (\mathbf{U}^T \mathbf{U})^{-1} \mathbf{U}^T$ are the background and right pseudoinverse of background, respectively [96].

3.2 Multiple Material Based Content Detection and Retrieval Methods for Hyperspectral Imagery

Hyperspectral imagery stands out among all other remote sensing methods due to the spectral characteristics of the matters observed at hundreds of distinct channels. This dense spectral and spatial information can be a valuable resource to describe the phenomenons in the scene. However, hyperspectral imagery contains highly redundant information, and it requires dedicated methods to extract proper features that can sufficiently model the image content.

Despite the increasing resolution of hyperspectral imaging systems in both spatial and spectral domains, there are times when one spatial pixel of a hyperspectral image may cover multiple physical phenomena due to insufficient spatial resolution of the imaging system. As a result, the spectral signature measured at such a discrete region (as shown in Figure 25) is a combination of the spectral signatures of blended matters in proportion to their abundance in the pixel and/or scattered energy from those matters.

One important step in utilizing hyperspectral remote sensing imagery is to find the pure spectral signatures of the materials, known as endmembers, and decompose mixed pixel signatures based on these endmembers to determine the abundances of these materials at a given pixel. This process is known as spectral unmixing. Spectral unmixing is essentially a type of blind source separation process that aims to identify endmembers and their corresponding abundances in pixel signatures.

In literature, spectral unmixing methods are considered either linear or nonlinear. As illustrated in Figure 24(a), linear unmixing methods assume that mixed pixel signatures measured by hyperspectral imaging systems are originated in i) combination of two or more endmember signatures in proportion to their abundances in a pixel, and ii) additive noise at each spectral band. According to this definition, spectral signa-

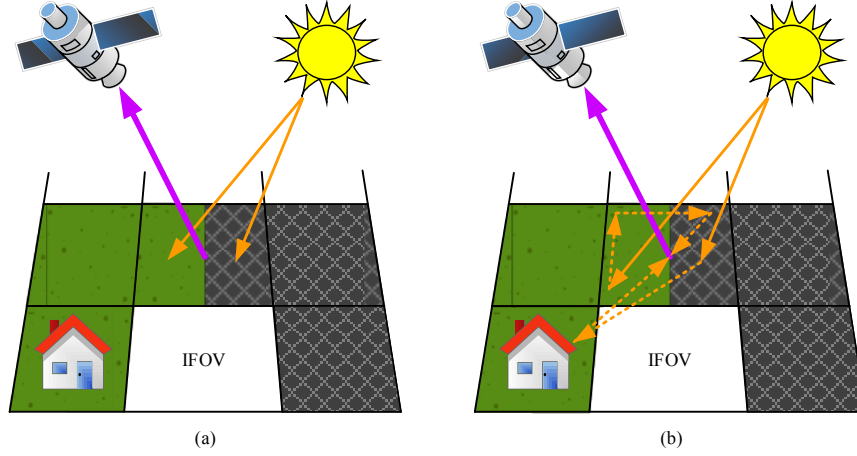


Figure 24: Linear and non-linear mixed pixel models.

ture \mathbf{x}_n^p of p -th spatial pixel of any hyperspectral image \mathbf{X}_n , which is composed of M endmembers can be defined as:

$$\mathbf{x}_n^p = \sum_{m=1}^M \mathbf{e}_n^m \cdot \alpha_n^p + \eta \quad (20)$$

where, \mathbf{e}_n^m , α_n^p and η are m -th endmember of hyperspectral image \mathbf{x}_n , fractional abundance of matter represented by m -th endmember in \mathbf{x}_n^p and additive noise, respectively.

In linear unmixing, the abundance of endmembers in \mathbf{x}_n^p have to satisfy two constraints: i) sum-to-one, ii) non-negativity. While sum-to-one constraint requires that cumulative abundance of all endmembers in \mathbf{x}_n^p must be equal to 1, non-negativity constraint enforces abundance of all endmembers in \mathbf{x}_n^p to be greater than or equal to 0.

Since the pure signature of the matters in a scene so, called endmembers, may not exist in a hyperspectral image due to insufficient spatial resolution of the imaging system or any other reason, certain linear methods make use of auxiliary endmember signature archives during the unmixing process.

On the other hand, nonlinear unmixing methods assume that mixed pixel spectral signatures originate in scattered energy from different matters that constitute the scene either at the microscopic or intimate level, as illustrated in Figure 24(b). Thus, non-linear unmixing is considered as an ill-posed problem and is usually not preferred in a solution of real-life spectral unmixing problems.

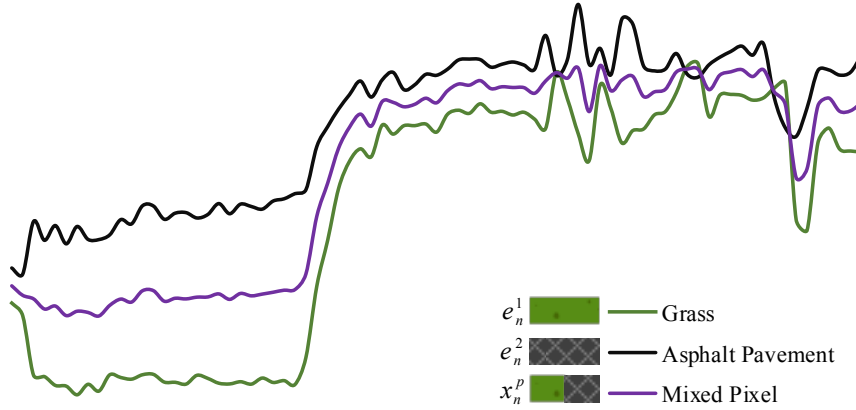


Figure 25: Mixed pixel signature.

All CBHIR systems proposed in the literature, except [97], adopt spectral unmixing-based strategies for two main purposes: 1) to reveal spectral characteristics of the matters that constitute the scene, 2) to get rid of information redundancy in the hyperspectral imagery. Thus, state-of-the-art CBHIR systems intensively use endmembers in conjunction with their proportions in the pixel signatures to model hyperspectral images in different ways.

CBHIR systems proposed in [98, 99, 100] model hyperspectral images with endmembers obtained via Pixel Purity Index (PPI), N-FINDR, and A-PPI linear unmixing algorithms, respectively. In the retrieval phase, all three systems utilize one-to-one endmember matching based Spectral Signature Matching Algorithm (SSMA) to assess the similarity between the hyperspectral images. SSMA attempts to match each query image endmember with one of the archive image endmembers, considering a given Spectral Angular Distance (SAD) threshold. Subsequently, the relative abundance difference for each matched endmember pair is calculated to generate a feature vector for signature comparison. Differently from [98, 99], CBHIR system proposed in [100] employs the SSMA with SID-SAD based hybrid distance. In [101], an updated version of the CBHIR system proposed in [98] implements a distributed hyperspectral imaging repository on a cloud computing platform.

In [102], an endmember matching-based distance for content-based hyperspectral image retrieval is proposed. The proposed distance mutually maps each individual endmember that belongs to one image to an endmember of the other image by considering SAD between them. Finally, the sum of the L-2 norm of vectors arising from minimum SAD between matched endmember pairs gives the Grana Distance between two hyperspectral images. The study evaluates the retrieval performance of the proposed hyperspectral image distance with Endmember Induction Heuristic Algorithm (EIHA) and N-FINDR linear unmixing algorithms. In [103], the same research group introduces an alternative CBHIR system that utilizes both endmembers and their abundances. The proposed system assesses the similarity of two hyperspectral images by calculating the sum of SAD between each endmember pair arising

from the Cartesian product of two endmember sets. It is worth noting that the proposed system weights the distance between each endmember pair, considering their abundances.

In [97], yet another CBHIR approach is proposed that copes with spectral and spatial information redundancy in hyperspectral imagery with a data compression strategy. To this end, each hyperspectral image is converted to a text stream (either pixel-wise or band-wise) and then encoded with the Lempel–Ziv–Welch (LZW) algorithm to obtain a dictionary that models the image. In the retrieval phase, the level of similarity between two hyperspectral images is assessed by dictionary distances that consider common and independent elements in corresponding dictionaries.

In [104], a hyperspectral imagery repository with retrieval functionality is introduced. The repository catalogs hyperspectral images with endmembers obtained via either N-FINDR or OSP linear unmixing algorithms in conjunction with their abundances. The user interacts with the system by choosing one or more spectral signatures from the library, already available in the repository, as a query. In the retrieval phase, the repository evaluates the level of similarity between query endmember(s) and cataloged image endmembers, considering the SAD. The repository also allows users to refine retrieval results by filtering the images with respect to predefined abundance thresholds for the endmembers in the query.

CBHIR system proposed in [105] constructs feature extraction strategy on sparse linear unmixing. This approach, which utilizes Sparse Unmixing via variable Splitting and Augmented Lagrangian (SunSAL) algorithm, aims at obtaining image endmembers employing spectral signatures already available in a library within the system. Consequently, the system skips some time-consuming steps (e.g., estimating the number of endmembers) in the spectral unmixing chain. However, this CBHIR approach requires a large built-in library that accommodates spectral signatures of all possible materials for a proper feature extraction phase. In the retrieval phase, the proposed system evaluates the similarity of two images considering the SAD between image endmembers.

In [106], hyperspectral images are characterized with two descriptors. The spectral descriptors corresponding to endmembers are obtained via the N-FINDR algorithm. In addition, the proposed system uses Gabor filters to compute a texture descriptor to model the image. In the retrieval phase, the system considers the sum of spectral and texture descriptor distances to assess the similarity between two hyperspectral images. To this end, the distance between spectral and textural descriptors of two images is calculated by adopting the Significance Credit Assessment method introduced in [103] and squared Euclidean distance between Gabor filter vectors, respectively. Similar to [106], the CBHIR system proposed in [107] characterizes hyperspectral images with two descriptors: spatial and spectral. The spatial descriptor is computed with a saliency map that combines four features: the first component of the Principal Component Analysis (PCA), orientation, spectral angle, and visible spectral band opponent. On the other hand, the spectral descriptor corresponds to a histogram of spectral words. The spectral words are obtained by clustering endmembers extracted from all the images in the archive. In the retrieval phase, the similarity between fea-

ture descriptors is calculated with squared Euclidean distance to assess the similarity between two images.

In [108], a CBHIR system is proposed to secure hyperspectral imagery retrieval by encrypting the image descriptors. The system characterizes hyperspectral images with spectral and texture descriptors. Scale-Invariant Feature Transform (SIFT) key-point descriptors of the RGB representation of the image and the endmembers extracted by the A-PPI linear unmixing algorithm are clustered with the k-means algorithm to obtain the spectral descriptor. This step defines spectral words that correspond to cluster centers. The proposed system employs the Gray Level Co-occurrence Matrix (GLCM) method to compute the texture descriptor to obtain contrast, correlation, energy, and entropy values. In the retrieval phase, these two descriptors are combined to model the images, and Jaccard distance is used to assess the similarity between the two images. Yet another CBHIR system that models the images with spectral and texture descriptors is introduced in [109]. The system obtains the spectral descriptors with endmembers extracted with A-PPI unmixing algorithm. To obtain the texture descriptors, the system adopts GLCM based method introduced in [108]. In the retrieval phase, the proposed system uses SID-SAM-based distance and Image Euclidean Distance to evaluate the similarity of spectral and texture descriptors, respectively.

In addition to the methods mentioned above, there is also a method that utilizes artificial neural networks. The method proposed in [110] suggests a model that provides pixel-based retrieval using Deep Convolutional Generative Adversarial Network (DCGAN). For this purpose, an artificial neural network model is trained with a combination of spectral and spatial vectors obtained using manually selected pure material signatures from hyperspectral images and neighboring pixel signatures.

CHAPTER 4

RESEARCH ACTIVITIES CONDUCTED WITHIN THE SCOPE OF THE THESIS

In the scope of the thesis, several studies were conducted on different datasets to detect single and multiple contents in hyperspectral images. This section provides detailed information about these studies. To ensure compatibility with Chapter 3, the first part presents studies conducted on detecting a single content, while the second part introduces studies that focus on the detection of multiple contents in a sequential manner.

4.1 Research Carried on Single Material Based Content Detection

As the details are presented in Chapter 3, single material-based content detection in hyperspectral imagery refers to the process of searching for a particular query signature, represented by \mathbf{x}_q , within the image pixels of a single hyperspectral image or all hyperspectral images in an archive, represented by \mathbf{X}_n .

The first research conducted within this context focused on detecting a specific gas emission in LWIR hyperspectral images. Remote sensing hyperspectral imaging for gas detection has various applications, such as investigating gas leaks, factory chimney emissions, and exhaust gases from motor vehicles. In the study, a method was proposed to reduce the blackbody effect in infrared hyperspectral images to enhance the performance of methane vapor detection within the image obtained by LWIR hyperspectral sensor [111].

Following the observation of the positive impact of the proposed blackbody effect correction method on content detection in LWIR hyperspectral images, the research activities within the scope of the thesis continued with a hyperspectral unmixing approach. In this context, an endmember-based method was adapted to detect the presence of gases in LWIR hyperspectral images by separating them from the background and other materials [112]. The method tested on the data used in the previous study showed the contribution of the Vertex Components Analysis (VCA) unmixing algorithm to the detection performance of gas emission, background, and other object hyperspectral signatures.

4.2 Research Carried on Multiple Material Based Content Detection

Following the research activities detailed in the previous section aimed at single material-based content-based retrieval, research activities for multiple material-based retrieval in remote sensing hyperspectral image archives were conducted in line with the ultimate research goal of the thesis.

To achieve our goal, relevant studies available in the literature, whose details are provided in Chapter 3, were reviewed. Then, these CBHIR systems were implemented in the MATLAB environment, and the following limitations were identified.

1. Computational cost increases as the number of endmembers extracted from the images increases.
2. The storage of all the endmembers extracted from images is a challenging task due to the high dimensionality of the hyperspectral imagery.

To overcome these specified limitations, a CBHIR system was proposed to store material information associated with each hyperspectral image efficiently and reduce the computational complexity at the access stage.

The CBHIR system characterizes hyperspectral images using spectral and abundance descriptors independent of the number of endmembers and spatial pixels. This reduces the time and computational power required for the retrieval process.

Problem Formulation and Notation

Let $\mathbf{X} = \{\mathbf{X}_1, \mathbf{X}_2, \dots, \mathbf{X}_N\}$ be an archive of N hyperspectral images, where \mathbf{X}_n is the n -th image in the archive. The proposed CBHIR system aims at retrieving a set $\mathbf{X}^R \subset \mathbf{X}$ of R images that are most similar to the query image \mathbf{X}_q in terms of materials present in it. To this end, the proposed system is characterized by two main modules: 1) representation of each hyperspectral image with two low-dimensional descriptors (which are obtained via a novel bag-of-endmembers approach); and 2) retrieval of hyperspectral images by using a computationally cost-effective strategy (which is achieved based on a hierarchical retrieval strategy). The block diagram of the proposed CBHIR system is illustrated in Figure 26.

Representation of Hyperspectral Images with Low-Dimensional Descriptors

In the first module, each hyperspectral image $\mathbf{X}_n, n = 1, 2, \dots, N$ is modeled in an off-line manner with two low-dimensional descriptors: 1) a binary spectral descriptor π_n that describes spectral characteristics of distinct materials present in \mathbf{X}_n ; and 2) an

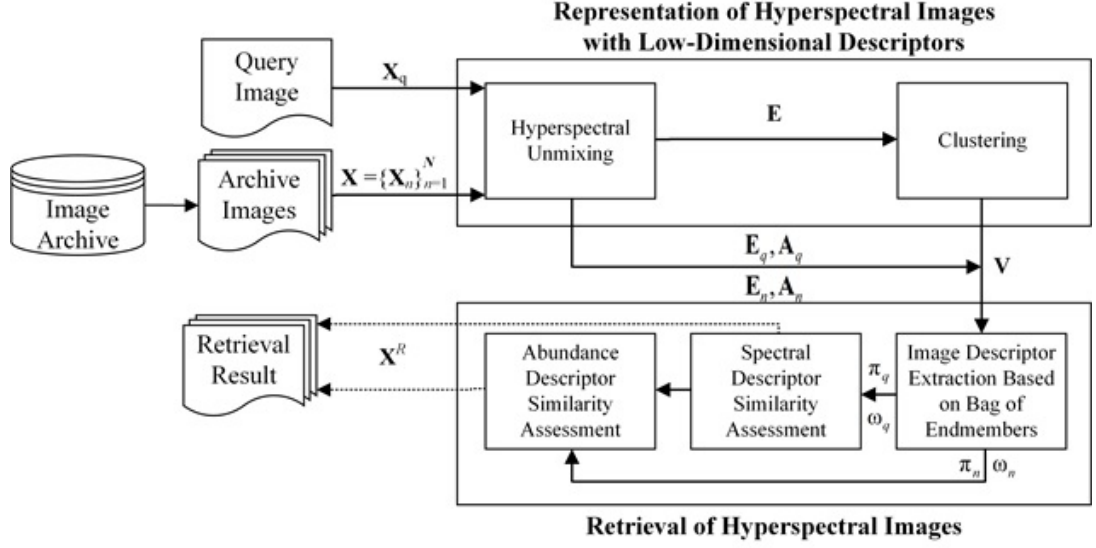


Figure 26: Block diagram of the proposed bag-of-endmembers based CBHIR system.

abundance descriptor ω_n that characterizes the fractional abundances of corresponding materials in \mathbf{X}_n . Spectral and abundance descriptors of the query image \mathbf{X}_q are calculated online.

To extract these descriptors from both query and archive hyperspectral images, we introduce a novel bag-of-endmembers based approach. To this end, we initially apply unmixing to each \mathbf{X}_n to obtain the signatures of spectrally distinct materials. Then, a bag \mathbf{B} of endmembers is initially constructed by the endmembers extracted from the hyperspectral images in the archive. Subsequently, this bag is clustered into \mathbf{K} clusters to obtain a spectral codebook \mathbf{V} .

Finally, hyperspectral image descriptors π_n and ω_n are calculated to represent each image with two low-dimensional vectors.

Retrieval of Hyperspectral Images

In the second module, the set \mathbf{X}^R of the most similar images to \mathbf{X}_q is selected by a novel hierarchical retrieval strategy, which initially identifies the candidate set of similar images based on only spectral descriptors and then exploits the abundance descriptors to enhance the retrieval performance.

In the first step, the similarity between \mathbf{X}_q and each \mathbf{X}_n is computed concerning the binary spectral descriptors π_q and π_n , $n = 1, 2, \dots, N$ only by estimating Hamming distance between them.

In the case of considering Scenario 3 (given in Table 1) for retrieval, \mathbf{X}^H is considered as the final set of retrieved images (i.e. $\mathbf{X}^H = \mathbf{X}^R$) and the algorithm stops at this

step. If Scenario 4 is considered for retrieval, \mathbf{X}^H is forwarded to the next step where we take into account the similarities between the fractional abundance of materials defined in abundance descriptors ω_n of images in \mathbf{X}^H and ω_q of the query by the Euclidean distance measure. Finally, the set $\mathbf{X}^R \subset \mathbf{X}$ of R images with the highest similarity to the abundance descriptors of ω_q is chosen.

Data-Set Description

A benchmark hyperspectral image archive was constructed to evaluate the retrieval performance of the proposed CBHIR system. To this end, a Level-1-Radiance (L1R) hyperspectral data product with 220 spectral bands acquired by EO-1 Hyperion in August 2015 in Ankara, Turkey, was selected. After removing spectral bands associated with low signal-to-noise, 119 were considered. The selected test site is a section of 3402x252 pixels with a spatial resolution of 30 m. The data product was divided into 216 patches of 63x63 pixels to construct the benchmark archive. Each hyperspectral image patch in the archive is annotated with 1) multiple low-level land-cover class labels and 2) single high-level land-use category labels (associated with the most significant content of the image). The number of land-cover classes associated with each image varies between 3 and 17, while in total, 29 different land-cover classes are defined concerning the whole archive. To annotate each image with appropriate land-cover class labels, very high-resolution (VHR) satellite images acquired in the same geographical area were used.

The dataset can be accessed at the following URL: <https://www.bigearth.eu/datasets>.

Comparative Performance Evaluation of the Proposed CBHIR System

The proposed system was separately evaluated for Scenario 3 and Scenario 4 in the experiments given in [1]. When Scenario 3 is considered, single-stage retrieval (SSR) is applied to the images represented by the binary spectral descriptors (BSD). This method is denoted as the proposed BSD-SSR). When Scenario 4 is considered, the proposed two-stage hierarchical retrieval (TSHR) algorithm is applied to the images' binary spectral and abundance descriptors (BSAD). This method is denoted as the proposed (BSAD-TSHR). To evaluate the performance of the proposed BSD-SSR and the BSAD-TSHR, two state-of-the-art methods were considered for comparison: 1) the endmember matching algorithm based on the Grana Distance [102] (denoted as EM-Grana), and 2) the endmember matching algorithm that weights the distances estimated by the SAD between each endmember pair by their abundances [103] (denotes as EM-WSAD).

The experimental results show that the proposed BSAD-TSHR, which considers both spectral and abundance descriptors, obtained significantly better metric values in the considered archive than the EM-Grana and EM-WSAD.

Table 2: Performance evaluation of CBHIR systems

CBHIR SYSTEM	Method	Accuracy (%)	Precision (%)	Recall (%)	Hamming Loss	Retrieval Time (ms)
Previously Proposed BoE Based System	BSD-SSR	69.19	83.87	80.30	4.02	0.095
	BSAD-TSHR	71.70	85.74	82.14	3.66	0.138
Em-Grana		63.93	82.32	73.89	4.64	85.325
EM-WSAD		56.75	77.71	70.14	5.78	10622.500

Although the proposed CBHIR system increases the retrieval performance compared to other systems in the literature, significant shortcomings have been identified in modeling hyperspectral images with an endmember-based approach. In Chapter 5, a novel CBHIR system is introduced to overcome these shortcomings.



Wild grass covered soil, bare soil, tree, red roof tile, metal roofing, white roofing, dark membrane, unpaved road, asphalt road, grass
(a)



Wild grass covered soil, bare soil, tree, red roof tile, metal roofing, white roofing, unpaved road, grass



Wild grass covered soil, bare soil, tree, Crop Type A, Crop Type B, red roof tile, metal roofing, white roofing, yellow roofing, unpaved road, asphalt road, grass
(b)



Wild grass covered soil, bare soil, tree, red roof tile, metal roofing, blue roofing, yellow roofing, concrete roofing, unpaved road, asphalt road, grass



Wild grass covered soil, bare soil, tree, red roof tile, metal roofing



Wild grass covered soil, bare soil, tree, Crop Type A, Crop Type B, asphalt road, grass



Wild grass covered soil, bare soil, red roof tile, metal roofing, white roofing, unpaved road, asphalt road, highway, grass

(c)



Wild grass covered soil, bare soil, tree, Crop Type A, Crop Type B, red roof tile, metal roofing, white roofing, dark membrane, asphalt, grass



Wild grass covered soil, bare soil, tree, red roof tile, metal roofing, white roofing, green roofing, blue roofing, dark membrane, concrete roofing, unpaved road, asphalt road, grass
(d)



Wild grass covered soil, bare soil, tree, red roof tile, metal roofing, white roofing, green roofing, blue roofing, dark membrane, unpaved road, asphalt road, grass, artificial grass

Figure 27: (a) query image, (b) images retrieved by EM-Grana, (c) images retrieved by the EM-WSAD and (d) images retrieved by the proposed CBHIR system.

CHAPTER 5

PROPOSED CONTENT-BASED HYPERSPECTRAL IMAGE RETRIEVAL SYSTEM

Unlike the existing hyperspectral image retrieval systems reviewed in Chapter 3, which dominantly measure the similarity between two hyperspectral images by employing endmember matching-based methods, the proposed system in this thesis addresses content-based hyperspectral image retrieval with a semantic approach by considering both spectral and spatial information. The proposed system assumes that hyperspectral remote sensing payload data products (airborne or spaceborne) are composed of two types of content: i) foreground and ii) background. It is worth noting that, to avoid terminological confusion, two definitions are used within the scope of the thesis: hyperspectral remote sensing payload data product and hyperspectral image. The hyperspectral remote sensing data product represents hyperspectral data obtained by the payload on the air or space platform covering an area on the Earth, and the hyperspectral image represents the patches that form the benchmark archive by dividing the data product into manageable small pieces.

The claim being made in this thesis is that when modeling hyperspectral remote sensing images, it is important to consider the varying prevalence of different types of material that make up the land cover in a territory covered by the data product. Specifically, certain types of material are much more common than others. These include areas with sparse natural vegetation, cultivated or uncultivated lands, terrestrial barren lands, and water bodies. In contrast, material classes such as artificial surfaces, urban areas, mining areas, and areas of materials with semantically remarkable spectral features are less prevalent. Failing to consider the prevalence of these material classes when creating content-based models for hyperspectral remote-sensing images can have significant consequences. For example, it can result in errors in accurately modeling certain content types that are relatively less common. This fact also makes it difficult to access related images due to the limitations of the models that are being used. Therefore, it is crucial to consider the prevalence of different material classes when modeling hyperspectral remote-sensing images in order to ensure accurate and reliable results.

The approach forming the basis of the proposed CBHIR system's semantic feature extraction method in this thesis is also supported by various institutions' studies on land cover diversity. The main MODerate-resolution Imaging Spectroradiometer (MODIS) Land Cover Classification product categorizes land cover into 17 classes defined by the International Geosphere-Biosphere Programme (IGBP). These classes

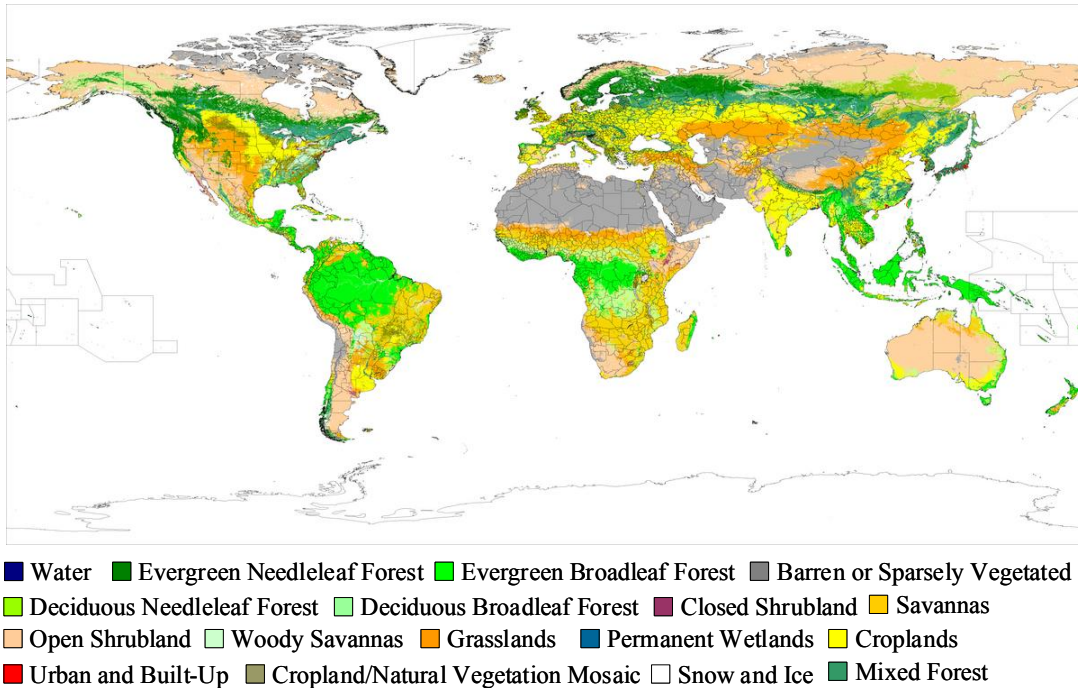


Figure 28: Terra MODIS MOD12C1 17 land cover classes defined by the IGBP [113].

consist of 11 natural vegetation categories and three developed land categories, one of which includes a mix of natural vegetation, permanent snow or ice, barren or sparsely vegetated areas, and water bodies [113]. According to the classification map presented in Figure 28, it is apparent that certain land cover classes (i.e., Urban and Built-Up) possess relatively smaller surface areas when compared to the other dominant categories.

Similarly, the United Nations Food and Agriculture Organization (FAO) releases statistics on land cover globally, including Turkey [114]. The data reveals the distributions of various land cover classes, summarized in Table 3. It becomes apparent that certain land cover classes, such as tree-covered areas and terrestrial barren land, are more prevalent than others, like artificial surfaces (including urban and related areas), which have a significantly lower presence.

A similar situation is observed in the dataset used in the performance analysis section of the study, which is further elaborated in Chapter 5 with details. As given in Figure 29, remote sensing images comprise dominant and rarely seen content types.

In this study, where the proposed CBHIR system aims to be a reliable solution for the effective management of remote sensing hyperspectral image archives, hyperspectral image contents are divided into two groups in an unsupervised manner based on spectral features and extensiveness of dominant content types at the territorial level. Thus, hyperspectral image contents representing phenomena intensely present by nature in that portion of the Earth, e.g., sparse natural vegetation, cultivated or uncultivated lands, terrestrial barren lands, and large water bodies, are grouped as background

Table 3: 2021 Land Cover statistics by Food and Agriculture Organization (FAO) based on European Space Agency Climate Change Initiative - Land Cover (CCI-LC) Products (Value unit=1000 ha)

Land Cover Type	Value (World)	% (World)	Value (Türkiye)	% (Türkiye)
Artificial surfaces (including urban and associated areas)	60497.24	0.41%	671.21	0.86%
Herbaceous crops	1904136.38	12.94%	29778.27	38.06%
Woody crops	222476.44	1.51%	5351.88	6.84%
Grassland	1815006.92	12.34%	14179.79	18.13%
Tree-covered areas	4268269.01	29.02%	14995.66	19.17%
Mangroves	18426.19	0.13%	NA	NA
Shrub-covered areas	1605658.84	10.92%	7021.07	8.97%
Shrubs and/or herbaceous vegetation, aquatic or regularly flooded	193169.63	1.31%	207.7	0.27%
Sparsely natural vegetated areas	889080.29	6.04%	3153.12	4.03%
Terrestrial barren land	1912986.33	13.00%	1445.73	1.85%
Permanent snow and glaciers	1437574.48	9.77%	NA	NA
Inland water bodies	382913.86	2.60%	1427.3	1.82%



Figure 29: Dominant and rarely observed content types in remote sensing images.

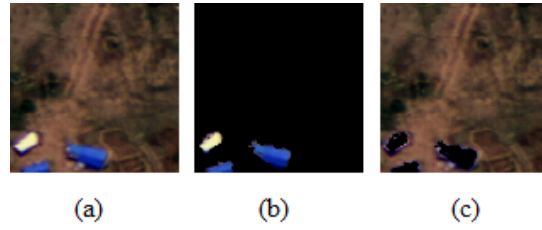


Figure 30: Pseudo-color representation of a remote sensing hyperspectral image \mathbf{X}_{1323} (a), illustration of foreground (b) and background (c) image contents.

content. On the other hand, the proposed CBHIR system claims that foreground content represents pixels or pixel segments that present remarkable differences in terms of spectral features in that particular region of the Earth and have an importance in terms of human perception, e.g., man-made objects, rarely seen minerals or anomalies as illustrated in Figure 30. Thus, such a categorization of content in hyperspectral remote sensing imagery enables the employment of suitable retrieval strategies to enhance the system’s overall performance.

The proposed method is constructed on this semantic approach to overcome the following shortcomings of existing CBHIR methods in the literature.

1. Poor retrieval performance issues that are caused by spectral information redundancy due to the relatively high amount of background content in the archive images.
2. CBHIR methods that model hyperspectral images by only endmembers may not accurately extract the endmembers from the images, or pure material signatures may not exist in the scene. These issues may lead to describing image content with inappropriate and/or insufficient spectral features.
3. Strategies (e.g., bag-of-endmembers) that aim at combining and clustering all endmembers to generate a global spectral vocabulary to model hyperspectral images may ignore spectral signatures (endmember) of rarely seen content in case of using an inappropriate clustering method or setting parameters of clustering method inaccurately.

The following sections of this chapter elaborate the proposed system in a systematic way.

5.1 Problem Formulation and Notation

Let $\mathbf{X} = \{\mathbf{X}_1, \mathbf{X}_2, \dots, \mathbf{X}_N\}$ be an archive of N hyperspectral images, where \mathbf{X}_n is the n -th image in the archive. The proposed CBHIR system aims at efficiently

retrieving a set $\mathbf{X}^R \subset \mathbf{X}$ of R hyperspectral images that contain similar content depicted by a query image \mathbf{X}_q or spectral signature \mathbf{x}_q provided by the user. A list of all mathematical symbols used throughout the thesis is given in Appendix C.

The proposed CBHIR system has two main modules: 1) an offline module to represent hyperspectral images with low-dimensional descriptors and 2) an online module to retrieve hyperspectral images using a computationally efficient hierarchical algorithm.

As illustrated in Figure 31, the proposed CBHIR system performs semantic feature extraction and representation of hyperspectral images with low-dimensional descriptors in the background in an offline manner. Contrary to existing CBHIR systems in the literature, thanks to the low-dimensional descriptors obtained in this offline module, the proposed CBHIR system allows online retrieval of hyperspectral images. These novel feature representation and retrieval approaches are elaborated in the following sub-sections.

5.2 Spectral Vocabulary Generation and Representing Hyperspectral Images with Low-Dimensional Descriptors

Spectral vocabulary generation and representing hyperspectral images with low dimensional descriptors steps of the proposed CBHIR system aim at representing each hyperspectral image \mathbf{X}_n in \mathbf{X} by four low-dimensional descriptor vectors: two binary spectral descriptors ϕ_n^f and ϕ_n^b to represent the spectral characteristics of foreground and background content, respectively and two abundance descriptors α_n^f and α_n^b to hold fractional abundance of corresponding content in the image \mathbf{X}_n . In addition to ϕ_n^f and ϕ_n^b , proposed system uses descriptor $\phi_n = (\phi_n^f, \phi_n^b)$ to represent spectral features of overall image content. Similarly, descriptor $\alpha_n = (\alpha_n^f, \alpha_n^b)$ represents fractional abundance of corresponding content in the image \mathbf{X}_n . In order to calculate these descriptors, we introduce a novel unsupervised spectral vocabulary generation approach as detailed in the following subsections.

The proposed CBHIR system is constructed on a semantic approach that argues hyperspectral remote sensing payload data products consist of two types of content: i) foreground and ii) background. Thus, this assumption requires a reliable method to sensitively identify foreground and background pixels or pixel groups (segments) in a hyperspectral remote sensing image. To this end, the proposed CBHIR system employs a territorial background content representation-based method to differentiate foreground and background image contents covering that specific region of the Earth.

Uncovering regional spectral features of background content begins with identifying regions that fully or massively contain materials that represent spectral features of the phenomenon intensely present by nature in that portion of the Earth, e.g., terrestrial barren land, natural vegetation, or cultivated areas. To identify reference background images in the archive, the proposed CBHIR system benefits from two indicators: a)

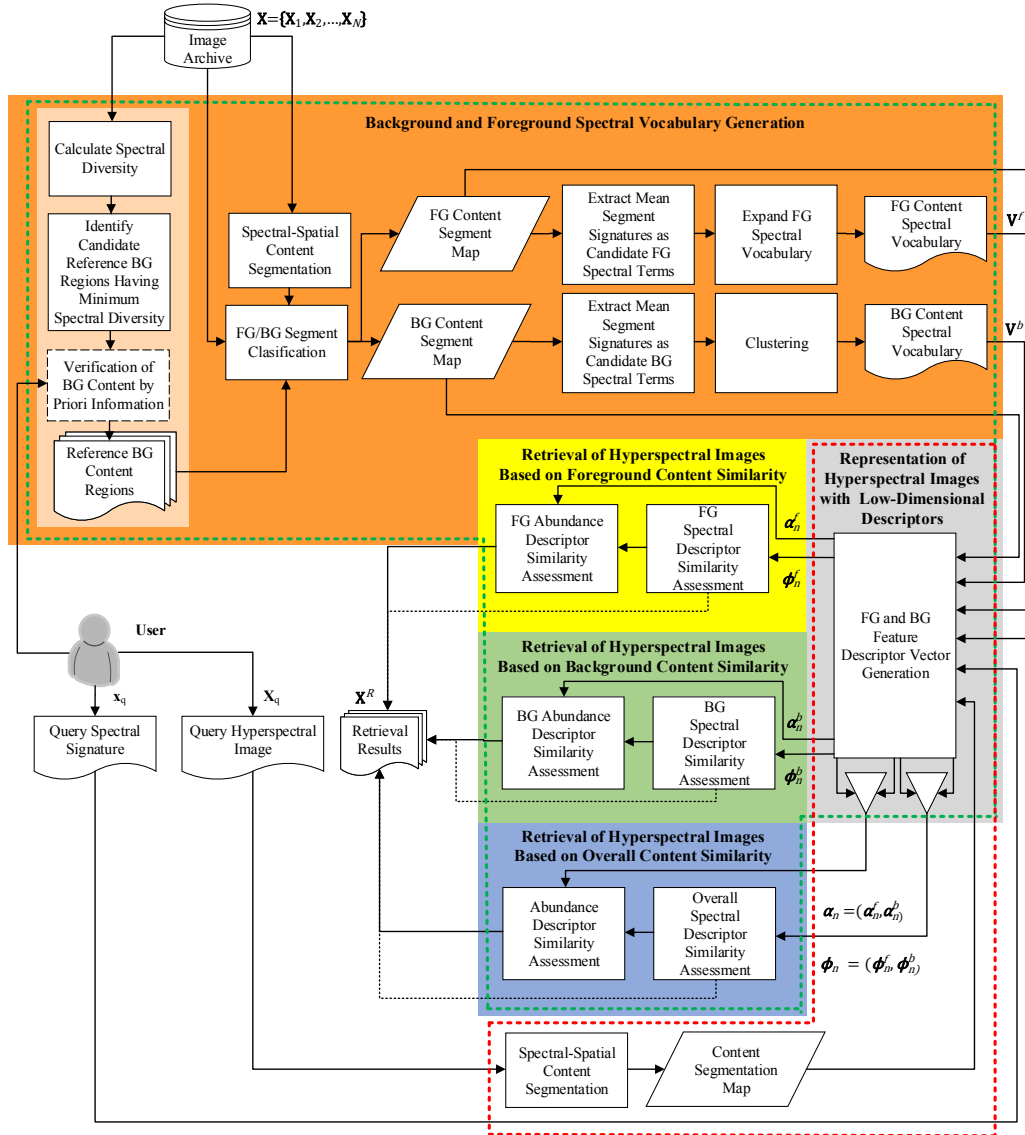


Figure 31: Block diagram of the proposed CBHIR system.

spectral diversity and b) known spectral characteristics of background contents in that region of the Earth.

In hyperspectral remote sensing imagery, background contents are identifiable by their ubiquitous presence across wide regions, resulting in little spectral variation in that region of the data product. This distinct feature enables the easy identification and extraction of such background contents from remote sensing imagery. The proposed method attempts to discover portions of the data product representing background content related to the specific geographical territory by performing a sliding window-based method. Then, candidate territorial background regions are identified by considering minimum intra-spectral diversity.

In addition to the low spectral diversity, the use of prior information is also crucial in determining background contents in hyperspectral remote sensing payload data products. For instance, sparse natural vegetation, cultivated or uncultivated agricultural lands, terrestrial barren areas, and water bodies can be easily detected in hyperspectral imagery depending on the wavelength range of the imaging payload. Therefore, in addition to the spectral diversity criterion, auxiliary methods (e.g., Surface Reflectance-derived Spectral Indices) play a critical role in identifying such background contents. At this point, it is important to note that in the absence of identified areas defining the background of a specific geographic territory, all contents in that territory are assumed as foreground by the proposed CBHIR system.

Subsequent to the identification of territorial background content regions, a superpixel-based segmentation, which was specifically developed for hyperspectral imagery, is applied to each hyperspectral image \mathbf{X}_n in \mathbf{X} . This step aims to identify hyperspectral image pixels (so-called segments) in the same image with similar spectral features and spatial relations. The superpixel-based segmentation step generates the initial content segment map for each hyperspectral image \mathbf{X}_n . In this way, the first crucial step is performed to extract semantic information about the content and to eliminate redundant spectral information in hyperspectral image \mathbf{X}_n . The proposed CBHIR system uses this content segment map to compress \mathbf{X}_n to eliminate highly redundant spectral information in hyperspectral imagery because of pixels having spatial relations. This is achieved by modeling each particular content segment with the mean spectral signature of that segment.

Determining pixel segments within each hyperspectral image and the classification of these segments either as foreground or background is followed by building the corresponding spectral vocabularies for these two types of content. To create these two types of content vocabularies, a foreground content vocabulary is obtained using the signatures obtained from foreground content segments, and a background content vocabulary is obtained by clustering the average spectral signatures obtained from background content segments. Thus, the foreground content in hyperspectral images is modeled with the highest precision, while on the other hand, the background content is modeled using a spectral-spatial compression method with a low-dimensional vocabulary.

The following step calculates low-dimensional foreground and background feature descriptors to bring online retrieval capability to the proposed CBHIR system. This is achieved by representing each hyperspectral image with four feature vectors: two binary spectral descriptors ϕ_n^f and ϕ_n^b to represent the spectral characteristics of foreground and background content, respectively and two abundance descriptors ϕ_n^f and ϕ_n^b to hold fractional abundance of corresponding content in the image. In addition to ϕ_n^f and ϕ_n^b , proposed system uses descriptor $\phi_n = (\phi_n^f, \phi_n^b)$ (or ϕ_q) to represent spectral features of overall image content. Similarly, descriptor $\alpha_n = (\alpha_n^f, \alpha_n^b)$ (or α_q) represents fractional abundance of corresponding content in the image \mathbf{X}_n (or \mathbf{X}_q).

Details of each step summarized above are given in the following sections.

5.2.1 Super-pixel Based Content Segmentation

As introduced in previous sections, the proposed CBHIR system benefits from spectral content vocabularies to retrieve hyperspectral images from the archive effectively in an online manner. Accordingly, discovering material diversity in the archive to generate the foreground and background content vocabularies is a crucial step for the proposed CBHIR system.

To this end, a superpixel-based segmentation is performed on each hyperspectral image \mathbf{X}_n in \mathbf{X} to group image pixels with similar spectral features and spatial relations that belong to a phenomenon in the scene. However, an effective method is required to perform such a segmentation that can handle high-dimensional spectral information with low computational complexity.

In order to overcome this, the proposed CBHIR system benefits from a novel superpixel-based segmentation algorithm dedicated to hyperspectral imagery [115], which is a derivative of the Simple Linear Iterative Clustering (SLIC) method [116]. This superpixel-based segmentation algorithm, namely Hyperspectral Simple Linear Iterative Clustering (hyperSLIC) in this thesis, is designed to cluster pixels in local regions rather than globally, which means that spatial correlation and spectral similarity are naturally considered during the segmentation process. Details of the hyperSLIC algorithm are given below.

The hyperSLIC algorithm begins by assigning a pre-defined number of super-pixel centers at equal distances. In order to streamline the clustering search process, hyperSLIC sets a defined local neighborhood around each cluster center. This neighborhood is a rectangular region with a width of w and a height of h . Limiting the search to only the surrounding $w \times h$ pixels for each cluster center greatly reduces the computational complexity compared to traditional clustering algorithms. During the main loop step, the algorithm employs the SID-SAM and Euclidean spectral and spatial distance criteria, respectively, to cluster each pixel in the local neighborhood for every cluster center. Following each iteration of the clustering algorithm, the cluster centers are updated to enhance the accuracy of subsequent iterations.

Images presented in Figure 32 have been taken from the dataset described in detail in Chapter 5. These images have undergone a segmentation process using the hyperSLIC algorithm. The minimum segment size for this process was set to 4x4 pixels, meaning that the image was divided into smaller segments, with each segment being at least 4x4 pixels. This step helps identify the image's content segments, which will be further analyzed in the feature extraction process. It is worth noting that the target segment size in the hyperSLIC algorithm should be chosen carefully, considering the ground sampling distance of the imaging system.

5.2.2 Background Suppression

Segmentation of hyperspectral imagery with a proper algorithm (i.e., hyperSLIC) results in identifying semantically (both spectral and spatial) related content pixels. This is a helpful step in dealing with highly redundant spectral information in hyperspectral imagery. On the other hand, the relatively high proportion of background content in the discovered segments poses a problem for efficient and quick retrieval of desired content.

In order to overcome this problem, the proposed CBHIR system introduces a novel background suppression-based method to make foreground content more easily identifiable. This method examines each content segment in the images with respect to spectral features of the territorial background content and identifies each segment's dissimilarity to spectral features of the territorial background regions.

Hyperspectral remote sensing image archives contain vast amounts of spectral data representing various content types. Among these content types, some are repetitive across multiple images and are commonly known as background. Due to their recurring presence, these images tend to have similar spectral content, with little variation between them, as given in Figure 34.

This unique feature simplifies the identification of background contents from remote-sensing images. Therefore, the proposed method examines each hyperspectral remote sensing payload data product in the archive to determine specific regions representing background content by considering spectral diversity. Candidate territorial background regions are identified based on minimum intra-spectral diversity from these regions.

In addition to spectral diversity, territorial background regions can be optionally examined with respect to known spectral characteristics of background content in that region of the Earth.

Details of the proposed background suppression method are given in the following subsections.

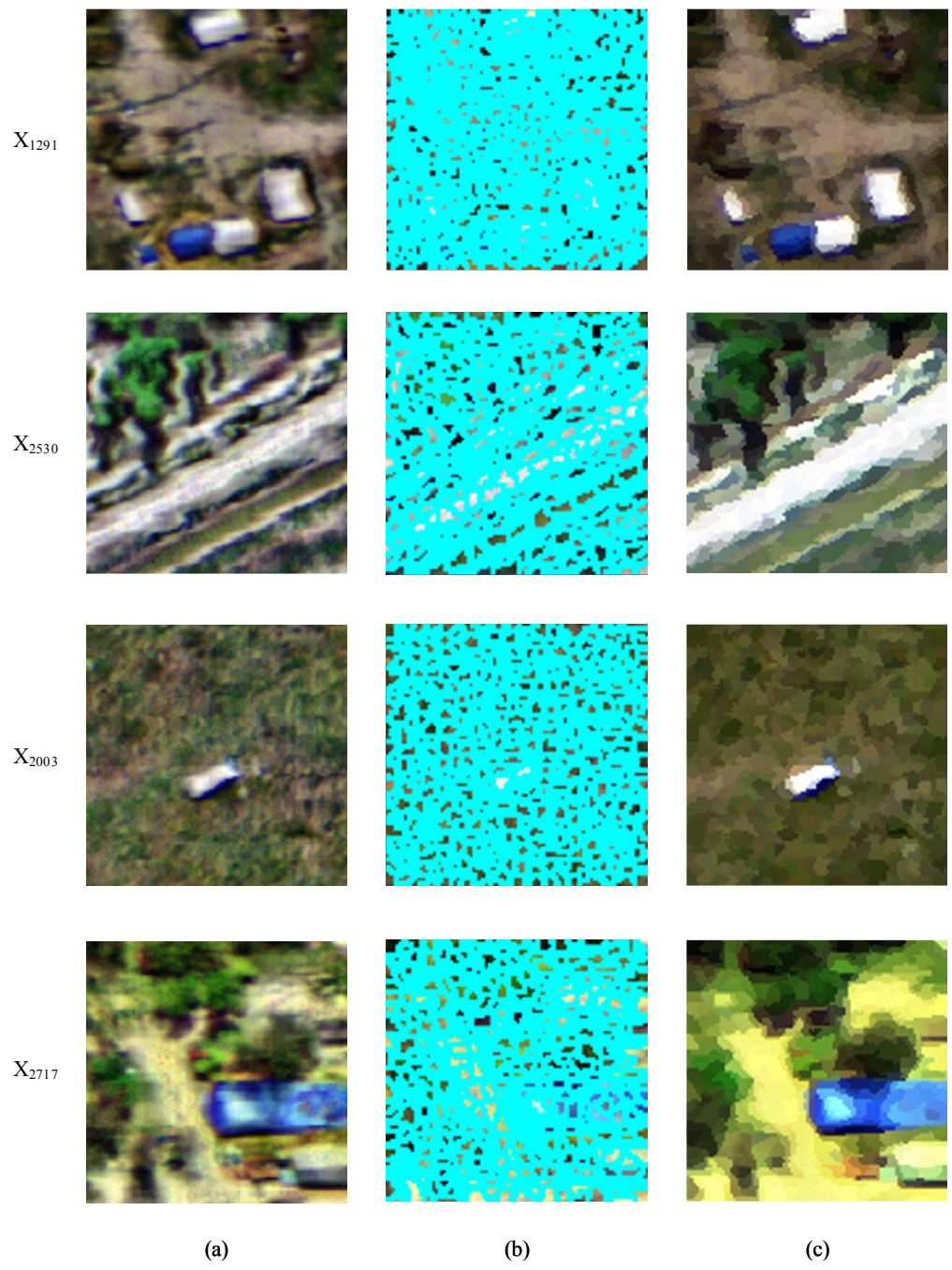


Figure 32: Sample super-pixel based content segmentation with hyperSLIC. a) False-color original image, b) hyperSLIC super-pixel based content segmentation, $w \times h = 4 \times 4$, c) False-color compressed image

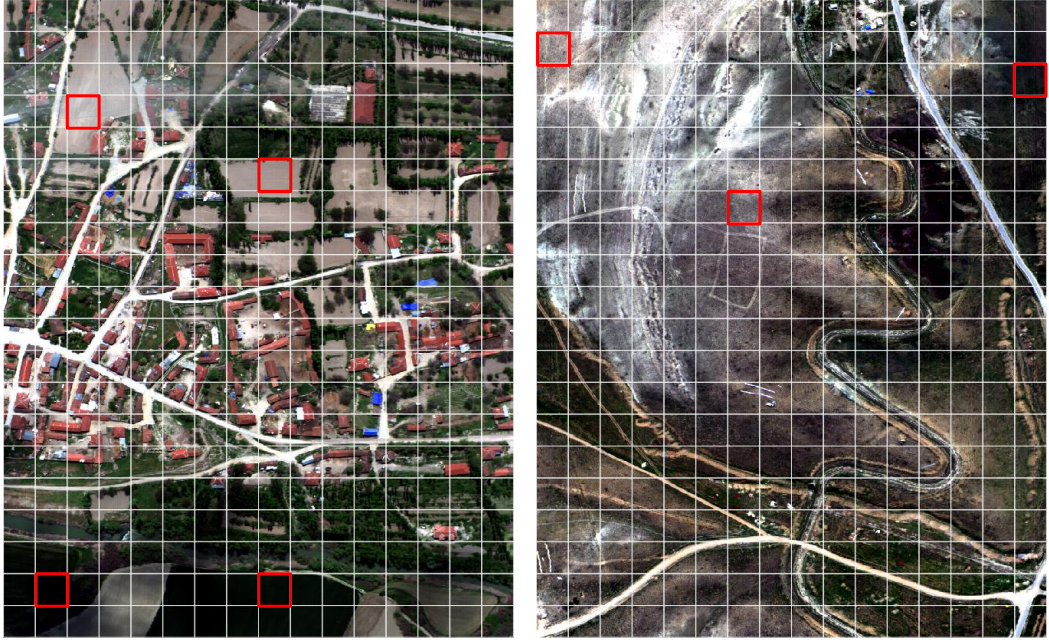


Figure 33: Candidate background content regions for a hyperspectral remote sensing payload product.

Discovering Spectral Diversity of Candidate Territorial Background Content

The proposed CBHIR system benefits from two indicators: a) spectral diversity and b) optional apriori information to identify territorial background regions in the data products to use these regions in the background suppression process. In the first step of the background suppression algorithm, spectral diversity $\sigma_{\mathbf{x}_n}$ for each individual hyperspectral image that has been created from the same hyperspectral remote sensing data product, which covers a specific region on the Earth, is calculated. The reason for adopting a regional approach in determining background contents is that hyperspectral images, which are spatially close to each other, tend to have similar hyperspectral background contents.

The proposed algorithm assumes that hyperspectral images that have the smallest intra-spectral diversity are more capable of representing background and can be used as reference background imagery for further steps, as illustrated in Figure 33. In order to identify these reference background images, the intra-spectral diversity of each image is calculated by measuring the average spectral angular distance as given in Equation 21.

$$\sigma_{\mathbf{x}_n} = \frac{1}{P^2} \sum_{i=1}^P \sum_{j=1}^P \cos^{-1} \left(\frac{\mathbf{x}_n^i \cdot \mathbf{x}_n^j}{\|\mathbf{x}_n^i\| \|\mathbf{x}_n^j\|} \right) \quad (21)$$

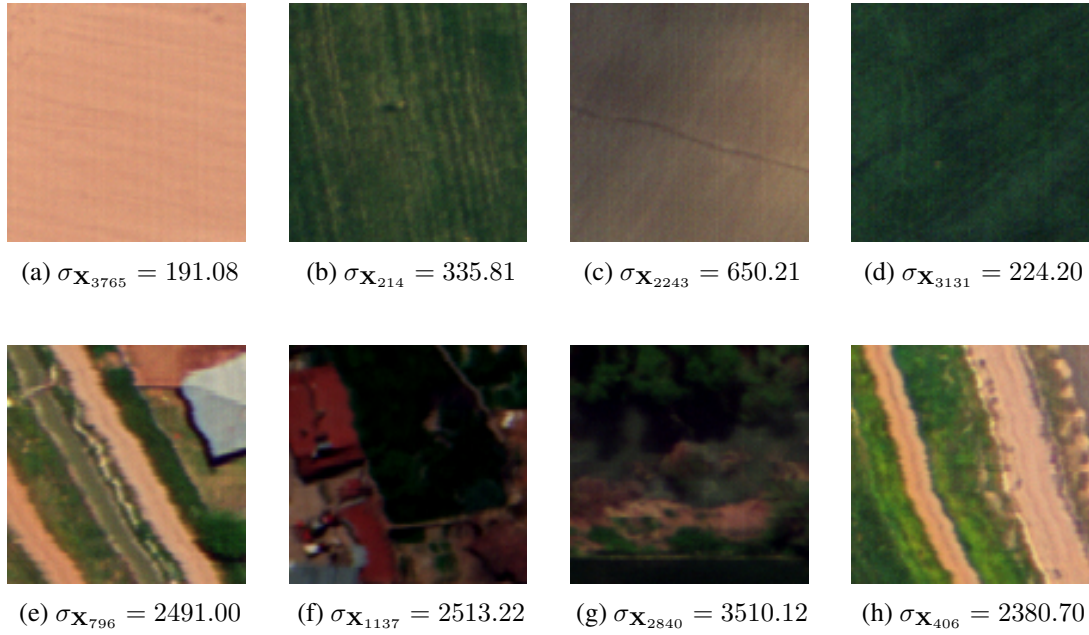


Figure 34: Sample hyperspectral images with low and high spectral diversity.

where P is the total number of pixels in image \mathbf{x}_n . \mathbf{x}_n^i and \mathbf{x}_n^j represent i -th and j -th pixels of \mathbf{x}_n . Equation 21 was inspired by Spectral Angular Mapper (SAM) [117], and the nonlinearity of the equation in calculating the dissimilarity of two spectral signatures enables better discrimination of low and high spectral diversity in image content.

In Figure 34, pseudo-RGB images extracted from sample hyperspectral images, with low and high material diversity, and corresponding average spectral angular distances are given. As illustrated in Figure 34, internal spectral diversity in a hyperspectral image goes up as the diversity of materials is increased.

Identifying Reference Background Regions with Minimum Spectral Diversity

Subsequent to the calculation of intra-spectral diversity for each image created from the same data product covering a specific region on the Earth, a specific number of hyperspectral images are identified as reference background images in this step. To this end, hyperspectral image \mathbf{X}_n in the archive with minimum intra-spectral diversity is identified as the first reference background image. Later on, the next hyperspectral image with minimum intra-spectral diversity is chosen as a candidate reference background image. A hyperspectral image is labeled as a reference background image if the spectral dissimilarity between the mean spectral signature of this image and the previously identified background images is bigger than a threshold defined by the user. This process is terminated if the desired number of hyperspectral images are identified as reference background images. In this way, the proposed system scans

through the images created from the same hyperspectral remote sensing data product and prevents identifying similar reference background images to better model the background content.

Verification Territorial Background Content via Surface Reflectance-Derived Spectral Indices

In the proposed method, in addition to spectral diversity in hyperspectral remote sensing images, an optional input for determining the content of an image in terms of background land cover in a specific geographic region is the known spectral characteristics of commonly seen land-cover content types. For this purpose, widely accepted spectral indices in the literature play a significant role. Appropriate indices within the wavelength range of hyperspectral imaging can enhance the selection of accurate background images for that archive.

For instance, the Normalized Difference Vegetation Index (NDVI) is an important tool used to measure the amount and health of vegetation in an area. The values of NDVI range from -1.0 to 1.0, with negative values indicating clouds and water, while positive values close to zero indicate bare soil or areas with little to no vegetation. Higher positive values of NDVI (0.1 - 0.5) indicate areas with sparse vegetation, while values of NDVI greater than 0.6 indicate areas with dense green vegetation.

Figure 36 illustrates the average NDVI values obtained from example images that exhibit significant background content in the hyperspectral dataset used in this study. Therefore, the use of appropriate surface reflectance-derived spectral indices score is considered to be a crucial input in determining the background content in the geographical area being examined.

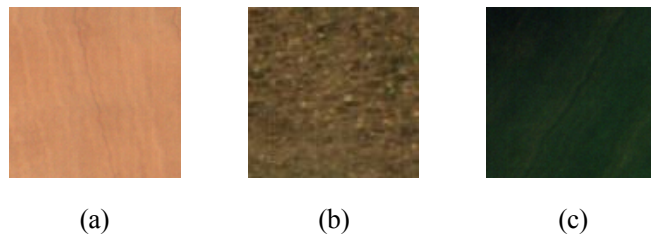


Figure 36: Average NDVI scores for different types of background content in hyperspectral imagery. a) Dominant Content: Plowed soil $\overline{\text{NDVI}}_{114} = 0.045$, b) Dominant Content: Sparsely natural vegetated areas $\overline{\text{NDVI}}_{2007} = 0.298$, c) Dominant Content: Field containing dense green vegetation $\overline{\text{NDVI}}_{2261} = 0.887$

Table 4 lists the indices used by the United States Geological Survey (USGS) to identify different land cover types in images obtained by Landsat missions with multispectral imagers. Although these indices are formulated for multispectral images in Landsat missions, they are also suitable for use with hyperspectral images. Table 5 presents the wavelength ranges and central wavelengths of images obtained from the

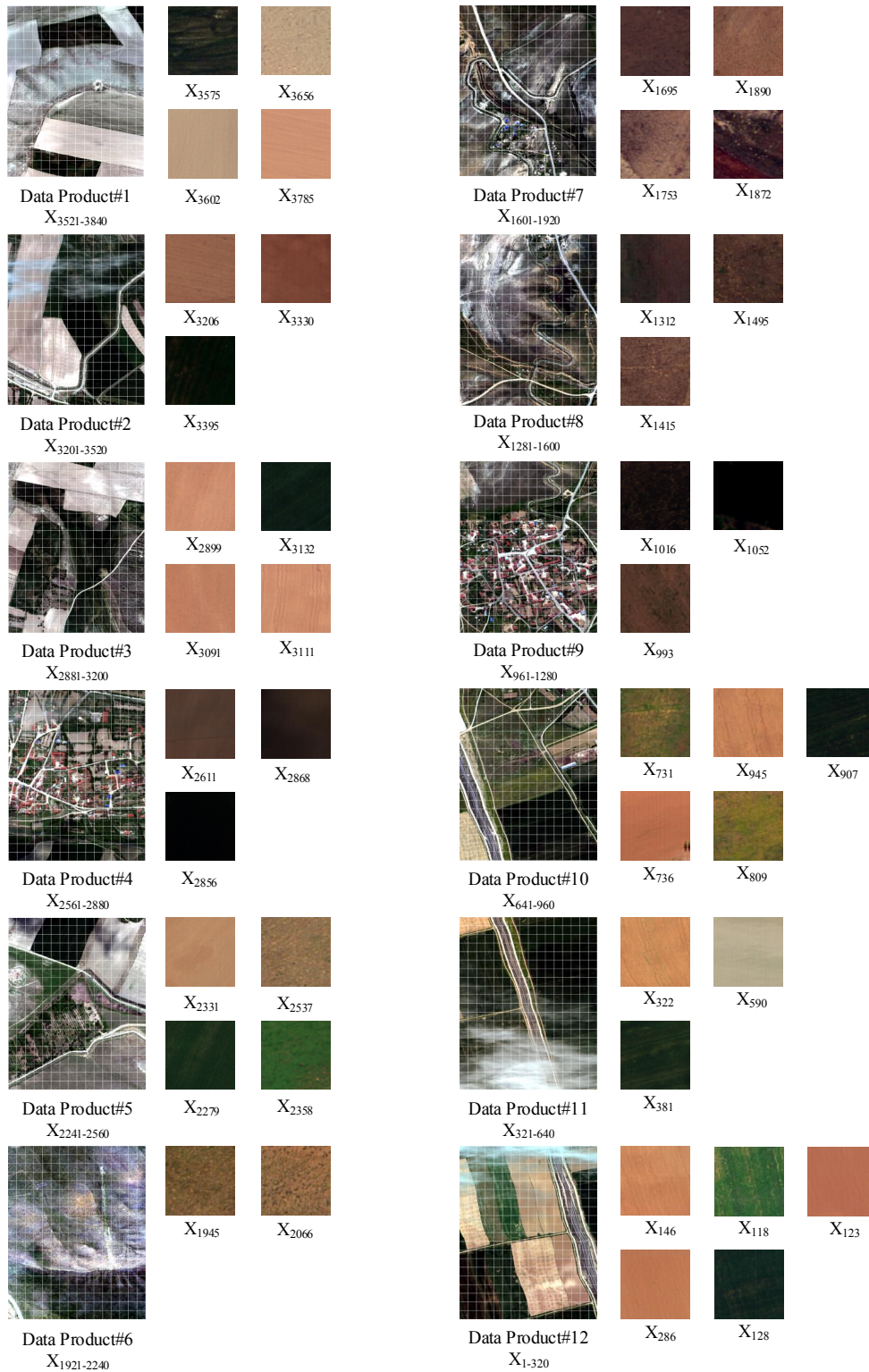


Figure 35: Background content regions designated by the proposed CBHIR system for hyperspectral remote sensing payload products.

Table 4: Surface Reflectance-Derived Spectral Indices

Surface Reflectance-Derived Spectral Index	Equation	Purpose
Normalized Difference Vegetation Index (NDVI)	$(NIR - R) / (NIR + R)$	Quantifying vegetation greenness can be done using NDVI, which is useful for assessing changes in plant health and understanding vegetation density.
Enhanced Vegetation Index (EVI)	$G \cdot ((NIR - R) / (NIR + C1 \cdot R - C2 \cdot B + L))$	EVI can be used to measure vegetation greenness. EVI corrects for atmospheric conditions and canopy background noise, and is more sensitive in areas with dense vegetation.
Soil Adjusted Vegetation Index (SAVI)	$((NIR - R) / (NIR + R + L)) \cdot (1 + L)$	SAVI helps to correct NDVI values in areas with low vegetation cover by taking into account the effect of soil brightness.
Modified Soil Adjusted Vegetation Index (MSAVI)	$\left(2 \cdot NIR + 1 - \sqrt{(2 \cdot NIR + 1)^2 - 8 \cdot (NIR - R)}\right) / 2$	MSAVI minimizes the effect of bare soil on the SAVI.
Normalized Difference Moisture Index (NDMI)	$(NIR - SWIR) / (NIR + SWIR)$	NDMI is used to determine vegetation water content.
Normalized Burn Ratio (NBR)	$(NIR - SWIR) / (NIR + SWIR)$	NBR is utilized to detect and assess the severity of burned areas.
Normalized Burn Ratio 2 (NBR2)	$(SWIR1 - SWIR2) / (SWIR1 + SWIR2)$	NBR2 can be used to highlight vegetation's water sensitivity and may be helpful in post-fire recovery studies.
Normalized Difference Snow Index (NDSI)	$(G - SWIR1) / (G + SWIR1)$	NDSI refers to the normalized difference between the green spectral bands and the shortwave infrared (SWIR).
R: Spectral band corresponding red color in visible range G: Spectral band corresponding green color in visible range B: Spectral band corresponding blue color in visible range NIR: Spectral band corresponding near-infrared SWIR1: Spectral band in shortwave-infrared range SWIR2: Spectral band in shortwave -infrared range L: Soil brightness correction factor defined as 0.5 to accommodate most land cover types		

multispectral imager on the Landsat 9 mission. In hyperspectral images, the indices mentioned in Table 4 can be easily calculated using the band closest to the central wavelength specified in Table 5.

Please see Figure 35 for hyperspectral images identified as reference background images for each hyperspectral remote sensing data products introduced in Chapter 5.

Identifying Foreground-Background Content Segments

As illustrated in the block diagram of the proposed CBHIR system (please see Figure 31), foreground and background content in a hyperspectral image are discriminated based on a background suppression-based approach. Thus, this method requires a reliable method to distinguish foreground and background contents using the reference hyperspectral images with materials representing the regional spectral features of the background for that specific territory.

Mahalanobis distance is a measure used to quantify the dissimilarity between a sample and a distribution. It considers the correlations between variables, making it particularly useful when dealing with multivariate data such as hyperspectral imagery.

Table 5: Landsat 9 Mission Operational Land Multispectral Imager 2 (OLI-2) Spectral Bands

Band	Minimum Lower Band Edge (nm)	Minimum Upper Band Edge (nm)	Center Wavelength (nm)
1 - Coastal/Aerosol	433	453	443
2 - Blue	450	515	4782
3 - Green	525	600	562
4 - Red	630	680	655
5 - NIR	845	885	865
6 - SWIR1	1560	1660	1610
7 - SWIR2	2100	2300	2200
8 - Panchromatic	500	680	590
9 - Cirrus	1360	1390	1375

Mahalanobis distance is widely employed in various fields, including statistics, pattern recognition, and machine learning.

Mahalanobis distance accounts for the correlation between different variables in the distribution, which is reflected in the use of the inverse covariance matrix. This is important because it normalizes the distance in each dimension by the variability in that dimension and the relationships with other dimensions. In other words, it scales each variable by its standard deviation and adjusts for the correlations between variables.

Mahalanobis distance has the following key features:

Scale Normalization: Mahalanobis distance normalizes the scale of each variable, preventing one variable with a large scale from dominating the distance metric. Thus, Mahalanobis distance is very suitable for hyperspectral image analysis.

Multivariate Nature: Unlike Euclidean distance, Mahalanobis distance considers correlations between variables, making it suitable for datasets with multiple dimensions.

Covariance Matrix: The covariance matrix captures the spread and orientation of the data points in the multivariate space.

In the proposed method, the analysis of how closely a content segment resembles the spectral characteristics of reference background image contents is calculated using the Mahalanobis distance-based scoring approach. In other words, to determine whether a content segment belongs to the foreground or background class, the spectral signature of the segment is compared against a set of pre-defined reference background images. If the spectral features of the segment/pixel noticeably deviate from the spectral features of all the background images, it is classified as foreground content.

The Mahalanobis distance between a spectral signature and a distribution is defined as follows:

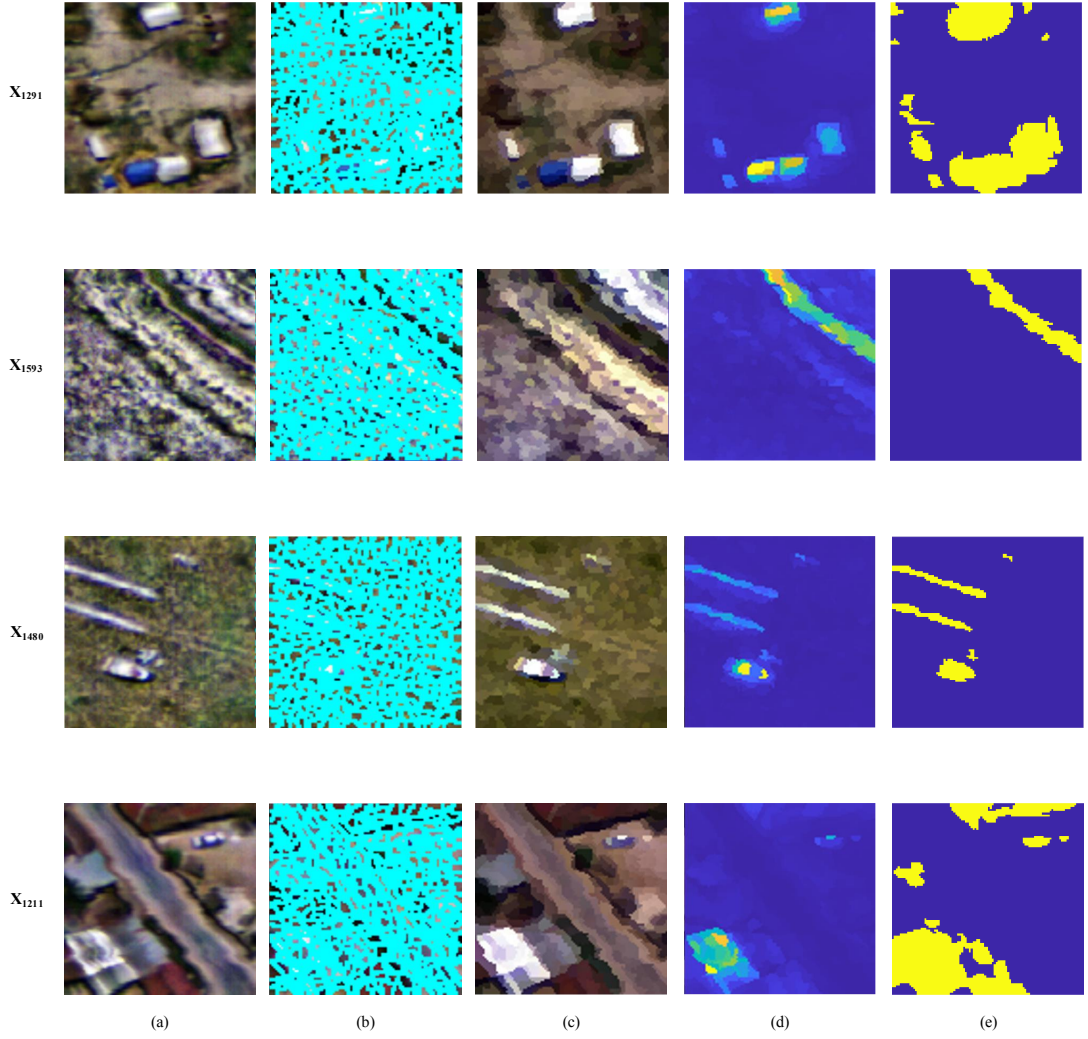


Figure 37: Foreground-background content segment classification. a) False-color original image, b) Segmentation map, c) segmented image, d) Mahalanobis score map, e) Foreground-background segment classification map.

$$\delta(\mathbf{x}_n^s) = (\mathbf{x}_n^s - \boldsymbol{\mu}_B)^T \boldsymbol{\Gamma}_B^{-1} (\mathbf{x}_n^s - \boldsymbol{\mu}_B) \quad (22)$$

where \mathbf{x}_n^s , $\boldsymbol{\mu}_B$, and $\boldsymbol{\Gamma}_B^{-1}$ represent mean spectral signature vector of s -th content segment in image \mathbf{X}_n , sample mean, and sample covariance matrix of territorial background image \mathbf{B} that is a combination of reference background images identified for that specific geographical region, respectively.

As a result, the similarities of content segments to the background within archive images can be measured in an unsupervised manner, as illustrated in Figure [37](#).

5.2.3 Building Spectral Vocabularies

To enhance the semantic significance of emphasized foreground contents in the thesis and minimize the redundant spectral information related to the background content, two distinct methods are used to create foreground and background content vocabularies. The foreground content vocabulary includes the spectral signatures of previously identified foreground content segments as is, while a clustering-based approach is used to create the background content vocabulary. This approach helps reduce the density of repeated background content information. By differentiating between foreground and background contents in the images within the archive, we can create specialized vocabularies related to each content type.

Creating the background content vocabulary through the clustering process is a meticulous procedure. Research conducted in the context of the thesis has revealed the advantages of utilizing the DBSCAN (Density-Based Spatial Clustering of Applications with Noise) [118] clustering method over other methods, including k-means and kernel k-means.

DBSCAN is a clustering algorithm that groups together data points that are close to each other and have a sufficient number of nearby neighbors. DBSCAN is particularly useful for identifying clusters of arbitrary shapes in spatial data in n-dimensional space and works as described below.

1. Initialization:

Choose an arbitrary data point that has not been visited and retrieve its ϵ -neighborhood (a set of data points within a specified distance ϵ from the chosen point).

2. Core Point, Border Point, and Noise:

If the number of data points within the ϵ -neighborhood is greater than or equal to a predefined threshold (MinPts), the chosen point is considered a core point. If a point is not a core point but lies within the ϵ -neighborhood of a core point, it is considered a border point. If a point is neither a core nor a border point, it is classified as noise.

3. Growing a Cluster: If a data point is a core point, a cluster is formed by recursively adding all directly reachable points within the ϵ -neighborhood to the cluster.

4. Repeat: Repeat the process until all data points have been visited.

5.2.4 Representation of Hyperspectral Images with Low-Dimensional Descriptors

The proposed CBHIR system represents each hyperspectral image X_n in \mathbf{X} by four low-dimensional descriptor vectors: two binary partial spectral descriptors ϕ_n^f and ϕ_n^b to represent the spectral characteristics of foreground and background content, re-

	V ₁	V ₂	V ₃	V ₄	V ₅	V ₆	V ₇	V ₈
ϕ_n^f	1	0	0	1	1	0	1	1
α_n^f	0.03	0	0	0.08	0.11	0	0.06	0.01

	V ₁	V ₂	V ₃	V ₄	V ₅	V ₆	V ₇	V ₈
ϕ_n^b	1	0	1	1	0	1	0	1
α_n^b	0.12	0	0.19	0.02	0	0.43	0	0.24

Figure 38: Illustration of low-dimensional foreground and background content descriptors (where $|\mathbf{V}^f| = 8$ and $|\mathbf{V}^b| = 8$).

	V ₁	V ₂	V ₃	V ₄	V ₅	V ₆	V ₇	V ₈	V ₉	V ₁₀	V ₁₁	V ₁₂	V ₁₃	V ₁₄	V ₁₅	V ₁₆
ϕ_n	1	0	0	1	1	0	1	1	1	0	1	1	0	1	0	1
α_n	0.03	0	0	0.08	0.11	0	0.06	0.01	0.12	0	0.19	0.02	0	0.43	0	0.24

Figure 39: Illustration of low-dimensional overall content descriptors (where $|\mathbf{V}^f| = 8$ and $|\mathbf{V}^b| = 8$).

spectively and two partial abundance descriptors α_n^f and α_n^b to hold fractional abundance of corresponding content in the image \mathbf{X}_n , as illustrated in Figure 38.

In addition to ϕ_n^f and ϕ_n^b , proposed system uses the overall descriptor $\phi_n = (\phi_n^f, \phi_n^b)$ (or ϕ_q) to represent spectral features of overall image content. Similarly, descriptor $\alpha_n = (\alpha_n^f, \alpha_n^b)$ (or α_q) represents fractional abundance of corresponding content in the image \mathbf{X}_n (or \mathbf{X}_q), please see Figure 39.

At this point, it is important to underline that while the first part of the low-dimensional descriptors describes the image content that defines materials having a significant difference compared to the background in terms of spectral characteristics (e.g., artificial materials, anomalies), the second part defines the background content commonly seen in archive images.

To compute foreground spectral image descriptors, initially a spectral distance matrix $\mathbf{D}_{\phi_n^f, \mathbf{V}^f} = [d_{s,\psi}; s = 1, \dots, S; \psi = 1, \dots, \Psi]$ is constructed, where $d_{s,\psi}$ denotes a spectral distance estimated between s -th foreground segment mean signature extracted from the image \mathbf{X}_n and ψ -th spectral term in foreground content vocabulary \mathbf{V}^f . This can be estimated by any distance measure, whereas in this work, we consider the well-known spectral angular distance. Then, the distance matrix $\mathbf{D}_{\phi_n^f, \mathbf{V}^f}$ is quantized by setting the minimum element of each row to 1 and the remaining elements to 0. In this way, each image foreground segment mean signature is associated with a spectral term in the vocabulary \mathbf{V}^f considering the degree of spectral similarity. Then, $\mathbf{D}_{\phi_n^f, \mathbf{V}^f}$ is compressed into a fixed-size binary descriptor to obtain ϕ_n^f by applying Boolean OR operator along each column.

Similarly, a distance matrix $\mathbf{D}_{\phi_n^b, \mathbf{V}^b} = [d_{s,\omega}; s = 1, \dots, S; \omega = 1, \dots, \Omega]$ is constructed, where $d_{s,\omega}$ denotes a spectral distance estimated between s -th background segment's mean signature extracted from the image \mathbf{X}_n and ω -th spectral term in background content vocabulary \mathbf{V}^b . Then, the distance matrix $\mathbf{D}_{\phi_n^b, \mathbf{V}^b}$ is quantized in the same way to obtain fixed-size descriptor ϕ_n^b .

Accordingly, $\phi_n^f = [\phi_n^{f_1}, \dots, \phi_n^{f_\Psi}]$ and $\phi_n^b = [\phi_n^{b_1}, \dots, \phi_n^{b_\Omega}]$ are defined as Ψ and Ω dimensional binary spectral descriptors, where each element of the vector (i.e., descriptor) indicates existence of a unique material in hyperspectral image represented by the ψ -th and ω -th spectral term in the spectral vocabularies \mathbf{V}^f and \mathbf{V}^b , respectively. Obtained binary spectral descriptors have two main advantages: 1) they enable real-time search and accurate retrieval; and 2) they reduce the amount of memory required for storing hyperspectral image descriptors in the archives.

To calculate the foreground abundance descriptor α_n^f for \mathbf{X}_n , normalized fractional abundance of each foreground spectral term in \mathbf{V}^f is computed as given in Equation [23](#).

$$\alpha_n^{V_\psi^f} = \frac{c_n^{V_\psi^f}}{P} \quad (23)$$

where, $c_n^{V_\psi^f}$ and P corresponds to the cumulative number of pixels in segments labeled as ψ -th spectral term in foreground content vocabulary \mathbf{V}^f and total number pixels in \mathbf{X}_n , respectively.

Similarly, background abundance descriptor α_n^b for \mathbf{X}_n , normalized fractional abundance of each foreground spectral term in \mathbf{V}^b is computed as given in Equation [24](#).

$$\alpha_n^{V_\omega^b} = \frac{c_n^{V_\omega^b}}{P} \quad (24)$$

In addition to ϕ_n^f and ϕ_n^b , proposed system uses descriptor $\phi_n = (\phi_n^f, \phi_n^b)$ (or ϕ_q) to represent spectral features of overall image content. Similarly, descriptor $\alpha_n = (\alpha_n^f, \alpha_n^b)$ (or α_q) represents fractional abundance of corresponding content in the image \mathbf{X}_n (or \mathbf{X}_q), please see Figure [39](#).

5.3 Retrieving Hyperspectral Images with Low-Dimensional Feature Descriptors

The proposed novel CBHIR system allows users to perform hyperspectral retrieval with a hierarchical algorithm. Furthermore, the proposed hierarchical algorithm significantly reduces the image retrieval time since 1) it filters out a high number of irrelevant images (with respect to the spectral characteristics of distinct materials present

in the query image) at the first step by considering simple bitwise operations on low-dimensional spectral descriptors, and 2) in the second step the reduced set \mathbf{X}^H of images is queried only to retrieve the set $\mathbf{X}^R \subset \mathbf{X}^H$ of images with the highest similarities in terms of spectral characteristics of distinct materials and their fractional abundances present in the query image. It is worth noting that due to the considered two-step strategy, the proposed algorithm can be performed by either considering or neglecting the evaluation of the similarities among the abundances of materials. Accordingly, the proposed strategy meets the diverse needs of CBHIR applications defined in Table I.

This novel approach models hyperspectral image content with spectral terms referenced in the global foreground and background spectral vocabularies. Therefore, the proposed CBHIR system enables single material query based hyperspectral image retrieval as well. To this end, instead of a query hyperspectral image, the user is asked to provide a spectral signature representing material to be queried in the archive. Similar to multiple material-based retrieval, the proposed CBHIR system retrieves hyperspectral images in the archive that contain materials represented with a query signature.

Details of each retrieval scenario are explained in the following subsections.

Retrieval of Hyperspectral Images Based on Overall Content Similarity

In this retrieval scenario, the user benefits from the proposed system to retrieve hyperspectral images concerning overall content similarity by utilizing spectral and abundance descriptors of foreground and background contents. To this end, concatenated spectral and abundance descriptors calculated for foreground and background content of each hyperspectral image \mathbf{X}_n in the archive and spectral and abundance descriptors calculated query image \mathbf{X}_q are employed to perform multiple material-based retrievals.

In the first step, the similarity between \mathbf{X}_q and \mathbf{X}_n is computed concerning the binary spectral descriptors $\phi_n = (\phi_n^f, \phi_n^b)$ and ϕ_q by estimating the Hamming distance between them. Then, a set \mathbf{X}_H of $H \leq R$ images having the lowest Hamming distances are selected, while the remaining images in the archive are filtered out. In the case of considering only spectral descriptor-based similarity between hyperspectral images for retrieval, \mathbf{X}^H is considered as the final set of retrieved images (i.e., $\mathbf{X}^H = \mathbf{X}^R$) and the algorithm stops at this step. If the abundance of materials is also considered for retrieval, \mathbf{X}^H is forwarded to the second step. In the second step, the similarity between abundance descriptor $\alpha_n = (\alpha_n^f, \alpha_n^b)$ of each image in \mathbf{X}^H and α_q of the query image is estimated by considering the Euclidean distance measure. Then, the set $\mathbf{X}^R \subset \mathbf{X}^H$ of R images that have the highest similarity to the query image \mathbf{X}_q in terms of the fractional abundance of materials defined in abundance descriptors are chosen.

Retrieval of Hyperspectral Images Based on Foreground Content Similarity

In this retrieval scenario, the user benefits from the proposed system to retrieve hyperspectral images with respect to foreground content similarity with a two-steps hierarchical algorithm. In other words, since foreground and background content are modelled independently, user can perform a more effective retrieval process by forcing the system to focus only on foreground content those are significantly different from background, in terms of spectral features.

To this end, spectral and abundance descriptors calculated for foreground content of each hyperspectral image \mathbf{X}_n in the archive and overall spectral and abundance descriptors calculated query image \mathbf{X}_q are employed to perform multiple material based retrieval. It is critical to note that, in this retrieval scenario, spectral and abundance descriptors calculated for \mathbf{X}_n are modified so that portions of the descriptors related to background content vocabulary are discarded to perform the retrieval by focusing on foreground content only. Similarly, spectral and abundance descriptors calculated for \mathbf{X}_q are modified in a way that elements of descriptors referencing terms in background vocabulary are neglected.

In the first step, the similarity between \mathbf{X}_q and \mathbf{X}_n is computed with respect to the modified binary spectral descriptors ϕ_n and ϕ_q only by estimating Hamming distance between them. Then, a set \mathbf{X}_H of $H \leq R$ images having the lowest Hamming distance are selected, while the remaining images in the archive are filtered out. In case of considering Scenario 3 (please see Table 1) for retrieval, \mathbf{X}^H is considered as the final set of retrieved images (i.e., $\mathbf{X}^H = \mathbf{X}^R$) and the algorithm stops at this step. If Scenario 4 is considered for retrieval, \mathbf{X}^H is forwarded to the second step. In the second step, the similarity between modified abundance descriptor α_n of each image in \mathbf{X}^H and α_q of the query image is estimated by considering the Euclidean distance measure. Then, the set $\mathbf{X}^R \subset \mathbf{X}^H$ of R images that have the highest similarity to the query image \mathbf{X}_q in terms of the fractional abundance of materials defined in abundance descriptors is chosen.

Retrieval of Hyperspectral Images Based on Background Content Similarity

Similar to the retrieval of hyperspectral images with respect to foreground content similarity, the proposed CBHIR system allows the user to query hyperspectral images by only considering the background content similarity. In contrast to foreground content-based retrieval, in this retrieval scenario, spectral and abundance vectors of \mathbf{X}_n and \mathbf{X}_q are modified to focus only on background content. To this end, in the first step, the similarity between \mathbf{X}_q and \mathbf{X}_n is computed with respect to the modified background binary spectral descriptors ϕ_n and ϕ_q only by estimating Hamming distance between them.

Then, a set \mathbf{X}_H of $H \leq R$ images having the lowest Hamming distance are selected, while the remaining images in the archive are filtered out. In the case of considering Scenario 3 for retrieval, \mathbf{X}^H is considered as the final set of retrieved images (i.e.,

$\mathbf{X}^H = \mathbf{X}^R$), and the algorithm stops at this step. If Scenario 4 is considered for retrieval, \mathbf{X}^H is forwarded to the second step. In the second step, the similarity between abundance descriptor α_n^b of each image in \mathbf{X}^H and α_n^b of the query image is estimated by considering the Euclidean distance measure. Then, the set $\mathbf{X}^R \subset \mathbf{X}^H$ of R images that have the highest similarity to the query image \mathbf{X}_q in terms of the fractional abundance of materials defined in abundance descriptors is chosen.

As mentioned in previous sections, the proposed system supports single material based hyperspectral image retrieval scenarios as well. To perform a single material based retrieval, user is asked to provide a signatures describing spectral features of a content to be queried as defined in Scenario 1. In case fractional abundance of material to be queried is imported, user is also asked to provide minimum and maximum fractional abundance limits to perform retrieval that conforms with retrieval Scenario 2.

CHAPTER 6

DATA-SET DESCRIPTION

6.1 Data Source

In order to evaluate retrieval performance of proposed CBHIR system and compare with the state-of-the-art systems available in the literature, a multi-label benchmark hyperspectral image archive was created from a very high-resolution hyperspectral data products. The hyperspectral data products used during archive generation were acquired over a flight line covering Yenice and Yeşilkaya towns (which are located on the border of Eskişehir and Ankara cities) by VNIR hyperspectral imager of a multimodal imaging system (see Figure 40).

Sensor components of the imaging system are composed of two co-aligned very high-resolution hyperspectral (VNIR + SWIR), one RGB multispectral imager and one Fiber Optic Downwelling Irradiance Sensor (FODIS) to simultaneously measure the power of incident light during flight for atmospheric correction of VNIR hyperspectral images. In addition to the sensors, imaging system includes Applanix AP20 GPS/IMU, SOMAG GSM4000 gyro-stabilizer, two Headwall Hyperspectral Data Processing Units (HDPU) and a power distribution unit (see Figure 41). Specifications of sensors installed on the imaging system are provided in Table 3.

Data acquisition flight was performed with a Cessna 206 type aircraft with registration code TC-KFZ on May 04, 2019. Details of flight parameters and corresponding ground resolution obtained with each sensor are given in Table 7.

6.2 Data Pre-processing

In order to generate a coherent benchmark archive from large consecutive hyperspectral data products acquired during the mission and make the patches ready for the labeling phase, a set of pre-processing tasks were performed on raw data. Data pre-processing step consists of the following tasks: 1) digital number (raw image) to radiance conversion, 2) radiance to reflectance conversion, and 3) slicing data products to obtain patches to be labeled. Even though the first and second activities were performed using a commercial software named Headwall SpectralView (v3.2.0), the technical background of each step will be explained in the following paragraphs.



Figure 40: Fingerprint of the area imaged during flight and used in benchmark archive generation.

Table 6: Specifications of sensors of imaging system used during data acquisition.

	VNIR Hyperspectral	SWIR Hyperspectral	RGB Multispectral	FODIS
Manufacturer	Headwall		PhaseOne	Headwall
Commerical Name	HE Micro-Hypersec VNIR E Series	HE Micro-Hypersec SWIR 384	iXU-RS 1000	FODIS
Spectral Range (nm)	VNIR 400-1000	SWIR 900-2500	Visible	VNIR 400-1000
Spectral Channels	369	167	3	2400
Frame Size	1x1600	1x384	1108x8708	1x1
Design	Push-broom		Snapshot	Single Point
Dispersion/Pixel (nm)	1.63	9.6	-	0.25
Focal Plane Array	Scientific CMOS	MCT	CCD	CCD
Pixel Pitch (microns)	6.5	24	4.6	-
Aperture	F/2.5		-	-
Slit Length (mm)	10.5		-	-
Max. Frame Rate (Hz)	250	450	1.66	5
Bit Depth	16			
Cooling	TE Cooled	Stirling Cooled	-	-
Fore Optic	70 mm	100 mm	150 mm	Cosine Corrector



Figure 41: Multi-modal sensor configuration of the imaging system: a) sensors and auxiliary components, b) Cessna 206 manned airborne platform.

Table 7: Flight parameters and corresponding ground resolutions obtained with the sensors.

Aircraft	Cessna 206			
Flight Altitude (m)	~3000 (AGL) / ~3815 (ASL)			
Flight Speed (knots)	~90			
Flight Polygon Size (m)	8000 x 790			
	VNIR Hyperspectral	SWIR Hyperspectral	RGB Multispectral	
FOV (m)	445.17	276.48	1696.00 x 1356.80	
IFOV (cm)	27.86	72	1.32 x 1.32	

Digital number-to-radiance conversion of raw data is crucial in hyperspectral imaging. Since each individual detector on the focal plane array of a push-broom hyperspectral imager has slightly different gain and offset coefficients, raw hyperspectral images in digital number format are converted to radiance images before performing any analysis. This step achieves both removal of artifacts arising from non-uniformity (i.e., darker or brighter stripes), which are caused by different gain and offset coefficients of the detectors, and making each pixel signature in radiance unit ($\text{mW}/(\text{cm}^2 * \text{sr} * \mu\text{m})$), so that pixel signatures are standardized. Equation 25 is applied to every spatial-spectral pixel of the raw image in digital format (DN) to obtain a radiance (L) image.

$$L_{\lambda} = \frac{(DN_{\lambda} - SN_{\lambda}) \cdot \text{coeff}_{\lambda}}{t_{\text{exp}}} \quad (25)$$

where SN_{λ} , coeff_{λ} and t_{exp} are measured sensor noise, sensor coefficient, and exposure time of the sensor during data acquisition, respectively.

The second important pre-processing task performed on images was applying an atmospheric correction to obtain the reflectance signature of each pixel from the radiance image generated in the previous step. Atmospheric correction is usually done with three approaches: 1) using FODIS data acquired simultaneously with hyperspectral imagery, 2) using a calibrated reflectance tarp's signature located in the scene, or 3) using proprietary or publicly available correction models.

FODIS is a single-point spectrometer that synchronously measures incident light during data acquisition via a cosine corrector perpendicularly mounted on the top of the aircraft. Then, measured incident sunlight is used to remove atmospheric effects from hyperspectral data in radiance format. Thus, each pixel signature is converted to reflectance corresponding to the proportion of incident light reflected from that pixel at a specific wavelength.

Using a calibrated reflectance tarp, which exists in the scene, is yet another alternative method to obtain the reflectance of each pixel signature from hyperspectral data in radiance format. To this end, an average white reference signature is obtained from pixels covering only calibrated reflectance tarp in the scene. Then, each spatial-spectral pixel of the radiance data is divided by a white reference signature at a specific length as defined in Equation 26.

$$R_{\lambda} = \frac{L_{\lambda}}{WR_{\lambda}} \quad (26)$$

There have also been many proprietary and publicly available models exist to apply atmospheric correction to hyperspectral data in radiance format i.e., Fast Line-of-sight Atmospheric Analysis of Spectral Hypercubes (FLAASH), Atmospheric Correction (ATCOR) and Quick Atmospheric Correction (QUAC). Some of those methods use time and location information to estimate the position of the sun and the

strength of the incident solar light to perform atmospheric correction. On the other hand, some other methods, i.e., QUAC, do not require auxiliary information to generate reflectance data. Instead, these algorithms apply hypothetical methods based on radiance data to perform atmospheric correction.

As compared to the third one, the first and second methods allow for obtaining more realistic results since both methods include in-scene measurements of incident solar light despite the measurements being performed with different instruments. In this study, all the hyperspectral data products used in benchmark archive generation were converted to reflectance using incident solar radiance data captured by FODIS installed on the imaging system.

In the last step of data pre-processing, twelve reflectance hyperspectral payload data products with 2000x1600 pixels were equally sliced into 100x100 pixel square patches. By the end of this step, 3840 patches, each of which approximately covers 7.8 km² on the ground, were obtained.

6.3 Data Labelling

Accurate labeling of samples in any benchmark archive is a crucial task that explicitly affects performance analysis. Thus, patch labeling in the benchmark archive has been performed thanks to an auxiliary Very High Resolution (VHR) multispectral imagery, which provides 1.32 cm ground resolution acquired during the flight. (see Figure 42).

In addition to labeling each sample in the benchmark archive with VHR multispectral imagery, fieldwork was also performed on October 32, 2021, along the flight path to enhance the quality of labeling. In this fieldwork, objects existing in the hyperspectral image archive were also photographed from the ground to have more information about the objects (see Figure 43).

In order to perform an accurate data labeling process, a taxonomy of content labels has been generated with three main categories: i) vegetation, ii) man-made Objects, and iii) water bodies (see Figure 44).

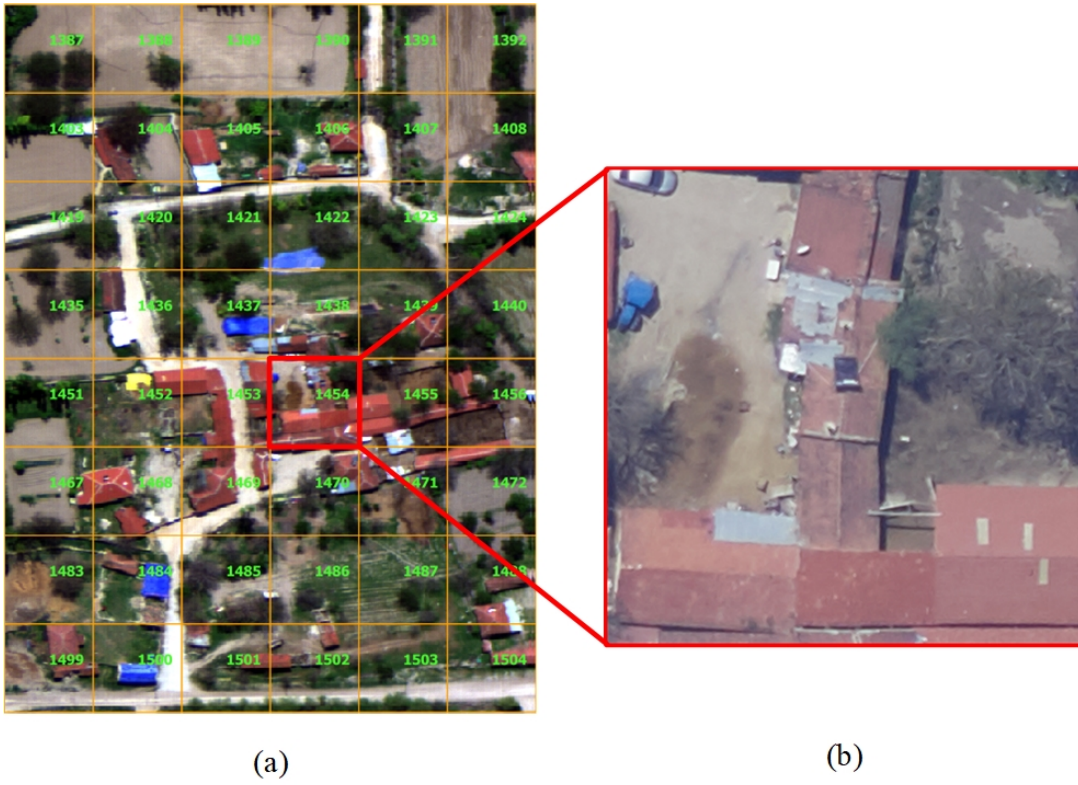


Figure 42: Proper labelling of hyperspectral images thanks to VHR multispectral imagery acquired during the same flight.



Figure 43: Fingerprint of the area imaged during flight and used in benchmark archive generation.

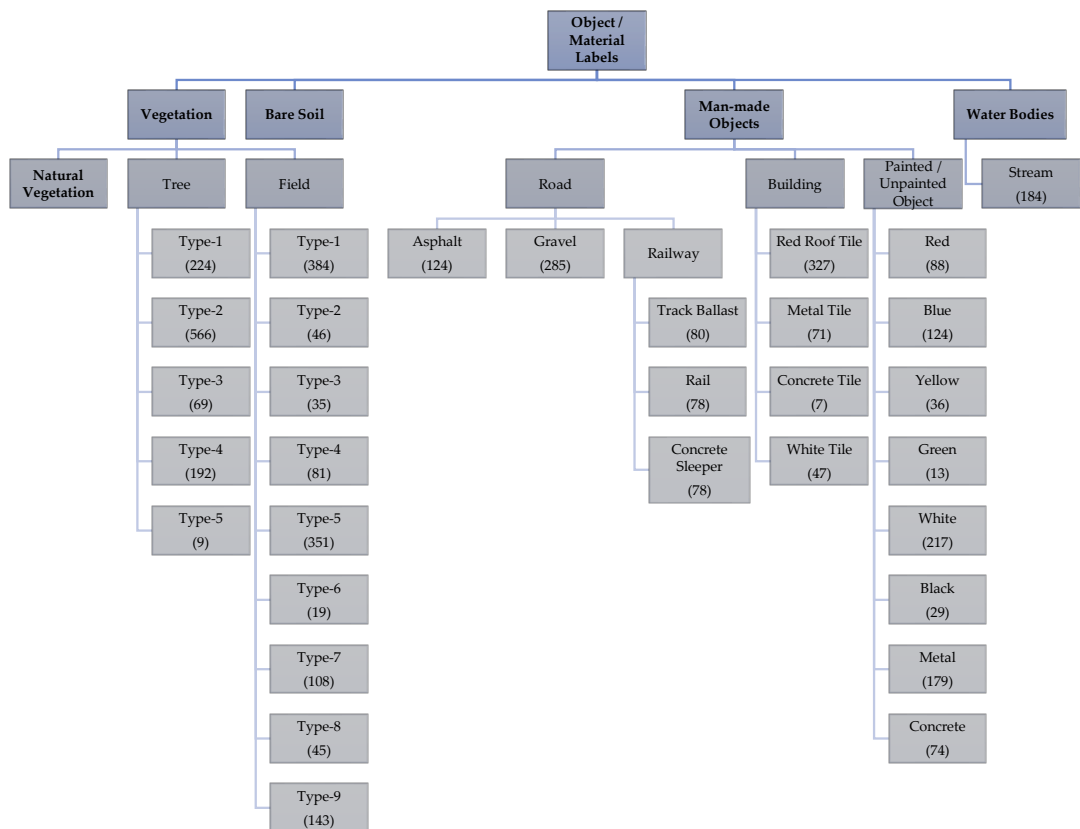


Figure 44: Taxonomy of content labels and corresponding number of images labeled under each sub-category.

CHAPTER 7

EXPERIMENTAL SETUP AND RESULTS

This section of the thesis elaborates on the experimental setup designed for performing objective and comparative performance analysis between the proposed and other CBHIR systems available in the literature.

7.1 Experimental Setup

A set of experiments were conducted to evaluate the performance of the proposed CBHIR system against other CBHIR systems in the literature. To this end, it is necessary to set specific variables and methods to perform the experiments presented in this section, including the proposed CBHIR system and other CBHIR systems from the literature. These parameters are essential for obtaining accurate experimental results. Therefore, we conducted preliminary experiments to determine the best values for these parameters. This section gives a detailed explanation of the values determined as a result of these preliminary experiments. First, the experimental setup of the CBHIR system proposed in this thesis and other studies in the literature are given.

Within the scope of the study, spectral-spatial segmentation is performed on hyperspectral images using the proposed system. In this segmentation performed with the hyperSLIC algorithm, the local neighborhood parameter is set to 4x4 pixels. The reason for choosing this size parameter is that, due to the spatial resolution of the hyperspectral images, spectral properties related to any material can be observed in an area of at least 4x4 pixels, which corresponds to an area of $\sim 1 \text{ m}^2$ on the ground. Such an area is clear enough to observe spectral features of matter in the scene for the spatial resolution of the imager at the given flight altitude in Table 7.

For each hyperspectral remote sensing data product, the proposed method requires determining the maximum number of reference background images. When examining the hyperspectral remote sensing data products that comprise the archive, this number has been determined as five. When determining reference background images, it has been observed that selecting the average spectral angular distance between images as 0.25 radians is the most suitable and sufficient for different background image sets.

The proposed CBHIR system uses Mahalanobis distance to regional reference background images to classify foreground and background content segments. At this

stage, the threshold value is set as the highest Mahalanobis distance to the regional background image pixels created by merging reference background images.

During the vocabulary generation stage, the spectral angular distance for foreground content dictionaries is set to 0.10 radians to eliminate the existence of repetition for the same material signature.

In order to evaluate the performance of the proposed BSD-SSR and system, we have considered three state-of-the-art methods for comparison: 1) the bag-of-endmember based method (denoted as BoE), 2) the endmember matching algorithm based on the Grana Distance (denoted as EM-Grana); and 3) the endmember matching algorithm that weights the distances estimated by the SAD between each endmember pair by their abundances (denotes as EM-WSAD).

To obtain the endmembers, VCA was used in the experiments for endmember based methods. HySime [119] was used in the experiments to estimate the number of endmembers.

In all experiments, CBHIR systems are requested to retrieve 10 most similar images to a given query image, and each hyperspectral image in the benchmark archive is used as a query image. Beyond each system’s retrieval performance, the retrieval time is also measured.

Computational Environment

The experiments were conducted in MATLAB® environment installed on a Microsoft Windows 10 operating system computer with 3.6 GHz Intel® i7-9750H processor 2.6 GHz and 32 GB RAM.

Performance Metrics

Since this study performs performance evaluation on a multi-label benchmark archive, we considered four different compatible multi-label performance metrics, which are: i) accuracy, ii) precision, iii) recall, and iv) Hamming loss. Let $\mathbf{L}_{\mathbf{X}_q}$ and $\mathbf{L}_{\mathbf{X}_r}$ be the label sets for the query image \mathbf{X}_q and any particular image \mathbf{X}_r in the corresponding set of retrieved images \mathbf{X}^R , respectively.

Accuracy is the fraction of identical content labels of the query and retrieved images in the union of label sets of two images and is defined as:

$$Accuracy = \frac{|\mathbf{L}_{\mathbf{X}_q} \cap \mathbf{L}_{\mathbf{X}_r}|}{|\mathbf{L}_{\mathbf{X}_q} \cup \mathbf{L}_{\mathbf{X}_r}|} \quad (27)$$

Thus, accuracy is directly proportional to the cardinality of the intersection of label sets of query and retrieved images. The retrieval performance increases when accu-

racy approaches 1. Precision is the fraction of identical content labels of query and retrieved images in the content label set of the retrieved image and is defined as:

$$Precision = \frac{|\mathbf{L}_{\mathbf{x}_q} \cap \mathbf{L}_{\mathbf{x}_r}|}{|\mathbf{L}_{\mathbf{x}_r}|} \quad (28)$$

In comparison with accuracy, precision evaluates the retrieval performance of the system by mainly focusing on the content labels of the retrieved image. Accordingly, content labels of the query image those apart from the matched ones are ignored. The retrieval performance increases when precision approaches 1. Unlike precision, recall is the fraction of identical content labels of query and retrieved images in the content labels of the query image and is defined as:

$$Recall = \frac{|\mathbf{L}_{\mathbf{x}_q} \cap \mathbf{L}_{\mathbf{x}_r}|}{|\mathbf{L}_{\mathbf{x}_q}|} \quad (29)$$

Thus, content labels of the retrieved image, those apart from the matched ones, are ignored. The retrieval performance increases when precision approaches 1. Hamming Loss evaluates the retrieval performance by calculating the symmetric difference (Δ) between two content label sets and defined as:

$$HammingLoss = \frac{|\mathbf{L}_{\mathbf{x}_q} \Delta \mathbf{L}_{\mathbf{x}_r}|}{|\mathbf{L}_{\mathbf{x}_q}|} \quad (30)$$

According to Hamming Loss, the system is penalized for each item not in the intersection of query and retrieved image content label sets. The retrieval performance increases when Hamming loss approaches zero.

7.2 Experimental Results

In this section, the retrieval performance of the proposed CBHIR system is compared with state-of-the-art systems available in the literature detailed in Chapter 3.

In the first subsection that follows, sample retrieval results of the proposed CBHIR system are presented, and in the second section, a comparative performance analysis with other systems is presented.

7.3 Sample Retrieval Results for the Proposed CBHIR System

In this subsection, the retrieval performance of the proposed CBHIR system within the scope of the thesis is demonstrated with visual examples using different query

images. For this purpose, query hyperspectral images are selected from different regions of the hyperspectral image archive used in the study. Careful consideration was given to selecting query hyperspectral images with varying foreground and background content.

The retrieval results presented in Figure 48 consist of content predominantly related to railway ballast material, steel rail, natural vegetation cover, and stabilized road, using a query image (please see Figure 45). The proposed system has successfully retrieved other images from the archive containing materials with similar spectral characteristics.

For the retrieval results presented in Figure 49, a query image was used with content primarily focused on a red-tiled roof, metal sheet roof, natural vegetation cover, and stabilized road. The proposed system retrieves other hyperspectral images from the archive containing materials with similar spectral characteristics.

Figure 50 presents the retrieval results of a query hyperspectral image comprising various land cover types, including a water stream, natural vegetation, bare soil, and gravel road (please see Figure 47).

In Figure 51, retrieval results for a query hyperspectral image specifically containing white tent tarpaulin observed in rural regions (please see Figure 46).

Figure 52 presents the retrieval results of a query hyperspectral image that is dominantly composed of bare soil and a specific tree type.

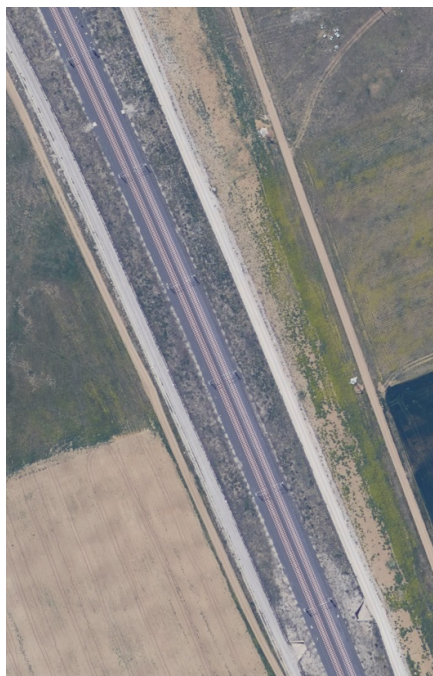


Figure 45: VHR multispectral image portion of the region containing railway ballast material, steel rail, natural vegetation cover, and stabilized road.



Figure 46: VHR multispectral image portion of the region containing white tent tarpaulin.



Figure 47: VHR multispectral image portion of the region containing water stream, gravel road and vegetation.

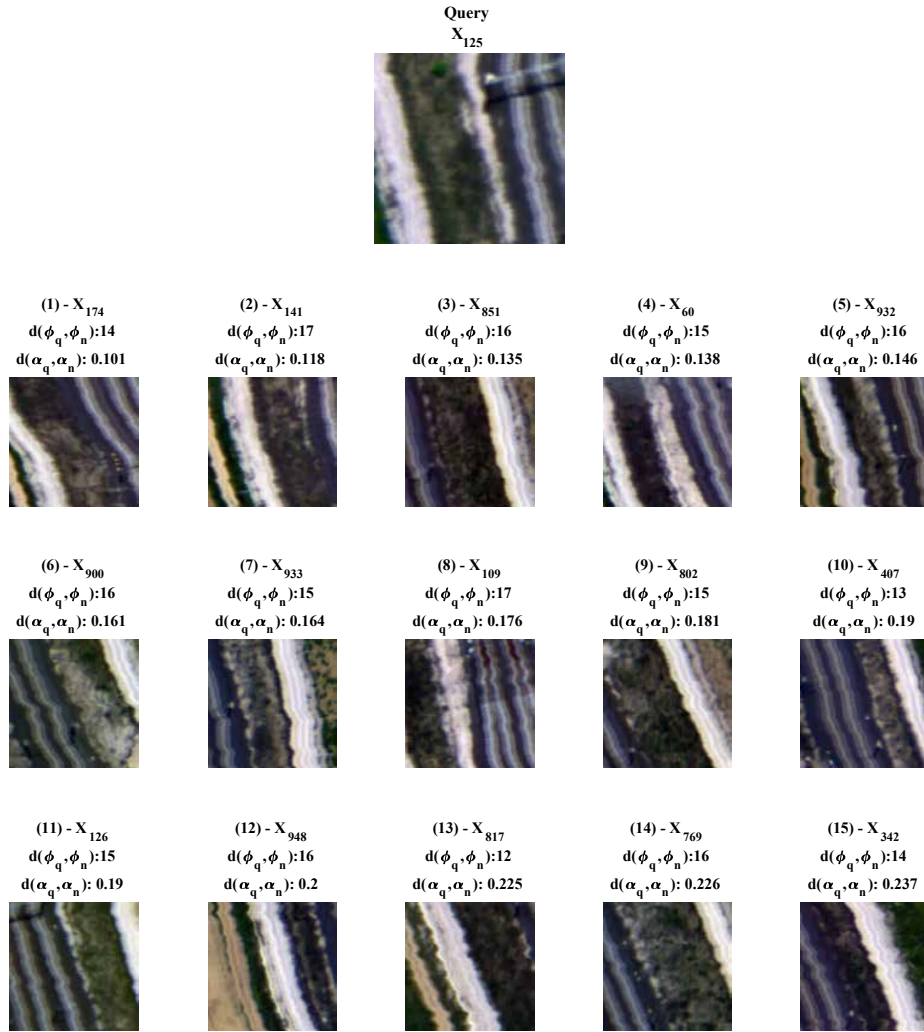


Figure 48: Content-based retrieval results of the proposed CBHIR system, $X_q = X_{125}$

Table 8: Content labels for retrieval results, $X_q = X_{125}$

X_q	1	2	3	4	5	6	7	8	9	10
X_{125}	X_{174}	X_{141}	X_{851}	X_{60}	X_{932}	X_{900}	X_{933}	X_{109}	X_{802}	X_{407}
track	track	track	track	track	track	track	track	track	track	track
ballast	ballast	ballast	ballast	ballast	ballast	ballast	ballast	ballast	ballast	ballast
rail	rail	rail	rail	rail	rail	rail	rail	rail	rail	rail
concrete sleeper	concrete sleeper	concrete sleeper	concrete sleeper	concrete sleeper	concrete sleeper	concrete sleeper	concrete sleeper	concrete sleeper	concrete sleeper	concrete sleeper
gravel road	gravel road	gravel road	gravel road	gravel road	gravel road	gravel road	gravel road	gravel road	gravel road	gravel road
natural veg.	natural veg.	natural veg.	natural veg.	natural veg.	natural veg.	natural veg.	natural veg.	natural veg.	natural veg.	natural veg.



Figure 49: Content-based retrieval result, $X_q = X_{1211}$

Table 9: Content labels for retrieval results, $X_q = X_{1211}$

X_q	1	2	3	4	5	6	7	8	9	10
X_{1211}	X_{1245}	X_{1212}	X_{1100}	X_{1142}	X_{2724}	X_{2758}	X_{2769}	X_{1159}	X_{1153}	X_{1143}
gravel road	gravel road		gravel road		gravel road	gravel road	gravel road	gravel road	gravel road	gravel road
metal sheet	metal sheet	metal sheet	metal sheet	metal sheet	metal sheet	metal sheet	metal sheet	metal sheet	metal sheet	metal sheet
bare soil	bare soil	bare soil	bare soil	bare soil	bare soil	bare soil	bare soil	bare soil	bare soil	metal sheet
red roof tile	red roof tile	red roof tile	red roof tile	red roof tile	red roof tile	red roof tile	red roof tile	red roof tile	red roof tile	red roof tile
white metal object	white metal object	white metal object			blue painted object	white metal object	white metal object	white metal object	white metal object	white metal object
tree	tree	tree	tree	tree	red painted object	tree	tree	blue painted object	blue painted object	black painted object
natural veg.	natural veg.	natural veg.	natural veg.	natural veg.	natural veg.	natural veg.	natural veg.	natural veg.	natural veg.	natural veg.

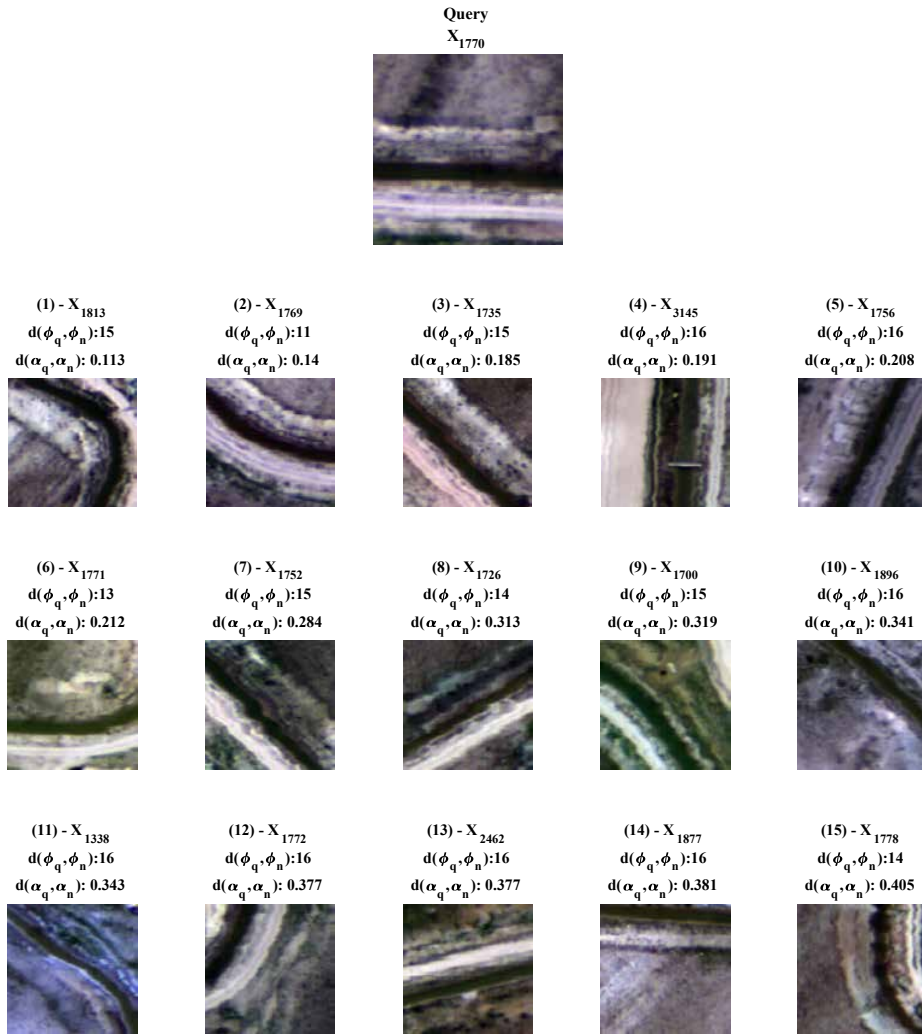


Figure 50: Content-based retrieval result, $X_q = X_{1770}$

Table 10: Content labels for retrieval results, $X_q = X_{1770}$

X_q	1	2	3	4	5	6	7	8	9	10
X_{1770}	X_{1813}	X_{1769}	X_{1735}	X_{3145}	X_{1756}	X_{1771}	X_{1752}	X_{1726}	X_{1700}	X_{1896}
water stream	water stream	water stream	water stream	water stream	water stream	water stream	water stream	water stream	water stream	water stream
gravel road	gravel road	gravel road	gravel road	gravel road	gravel road	gravel road	gravel road	gravel road	gravel road	gravel road
bare soil	bare soil	bare soil	bare soil	bare soil	bare soil	bare soil	bare soil	bare soil	bare soil	bare soil
natural veg.	natural veg.	natural veg.	natural veg.	natural veg.	natural veg.	natural veg.	natural veg.	natural veg.	natural veg.	natural veg.



Figure 51: Content-based retrieval result, $X_q = X_{1914}$

Table 11: Content labels for retrieval results, $X_q = X_{1914}$

X_q	1	2	3	4	5	6	7	8	9	10
X_{1914}	X_{1915}	X_{1846}	X_{1290}	X_{1882}	X_{1862}	X_{1799}	X_{2766}	X_{1780}	X_{3376}	X_{1291}
white tent	white tent	white tent	white tent	white tent	white tent	white tent	white tent	white tent	white tent	water stream
metal sheet	metal sheet	metal sheet		metal sheet				gravel road	metal sheet	blue painted object
blue painted object								tree	bare soil	bare soil
natural veg.	natural veg.	natural veg.	natural veg.	natural veg.	natural veg.	natural veg.	natural veg.	natural veg.	natural veg.	natural veg.
bare soil	bare soil	bare soil	bare soil	bare soil	bare soil	bare soil	bare soil	bare soil	natural veg.	natural veg.

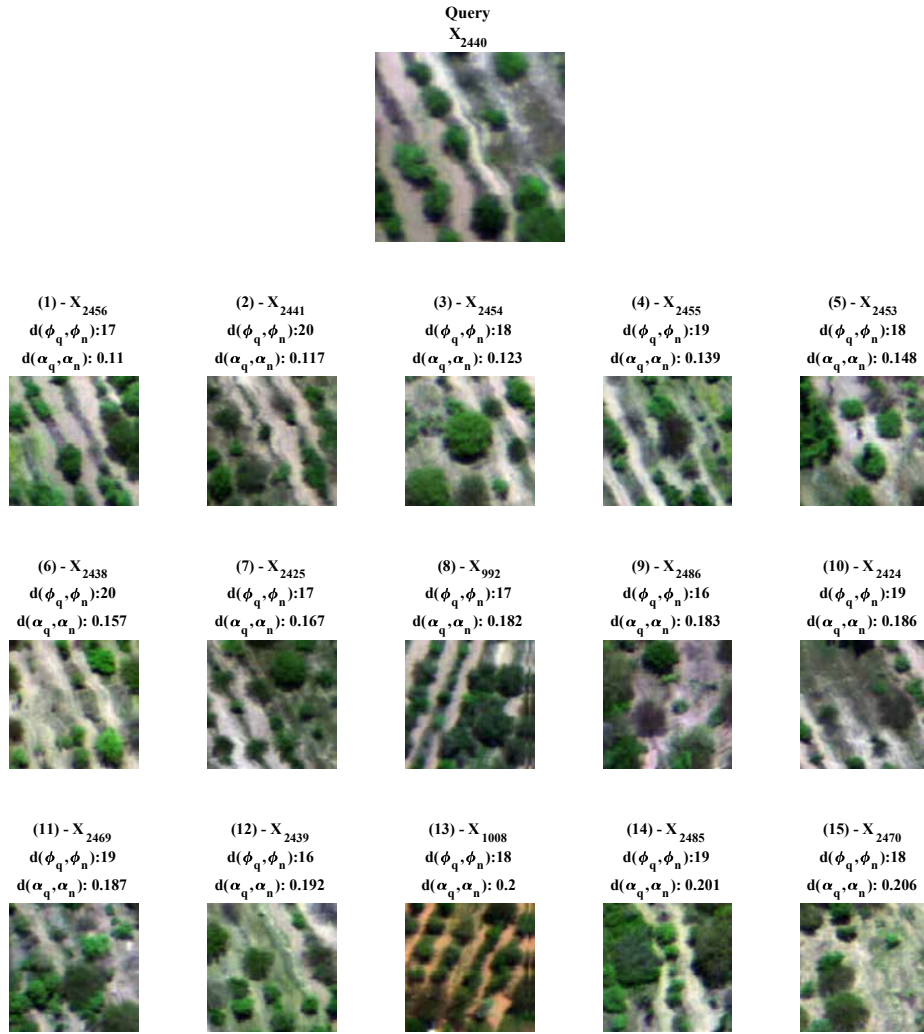


Figure 52: Content-based retrieval result, $X_q = X_{2440}$

Table 12: Content labels for retrieval results, $X_q = X_{2440}$

X_q	1	2	3	4	5	6	7	8	9	10
X_{2440}	X_{2456}	X_{2441}	X_{2454}	X_{2455}	X_{2453}	X_{2438}	X_{2425}	X_{992}	X_{2486}	X_{2424}
tree (Type-3)	tree (Type-3)	tree (Type-3)	tree (Type-3)	tree (Type-3)	tree (Type-3)	tree (Type-3)	tree (Type-3)	tree (Type-3)	tree (Type-3)	tree (Type-3)
bare soil	bare soil	bare soil	bare soil	bare soil	bare soil	bare soil	bare soil	bare soil	bare soil	bare soil
natural veg.	natural veg.	natural veg.	natural veg.	natural veg.	natural veg.	natural veg.	natural veg.	natural veg.	natural veg.	natural veg.

7.4 Further Performance Analysis of the Proposed CBHIR System

In addition to the above results obtained by considering both vocabularies, the proposed system was also tested against only foreground and background-based retrieval cases. The retrieval results presented in Figure 53 and the corresponding content labels given in Table 13 were obtained against a query image that contains a high abundance of man-made objects, particularly buildings with red roof tiles. The retrieval results given in Figure 53 show that the proposed system is capable of retrieving images with similar foreground contents.

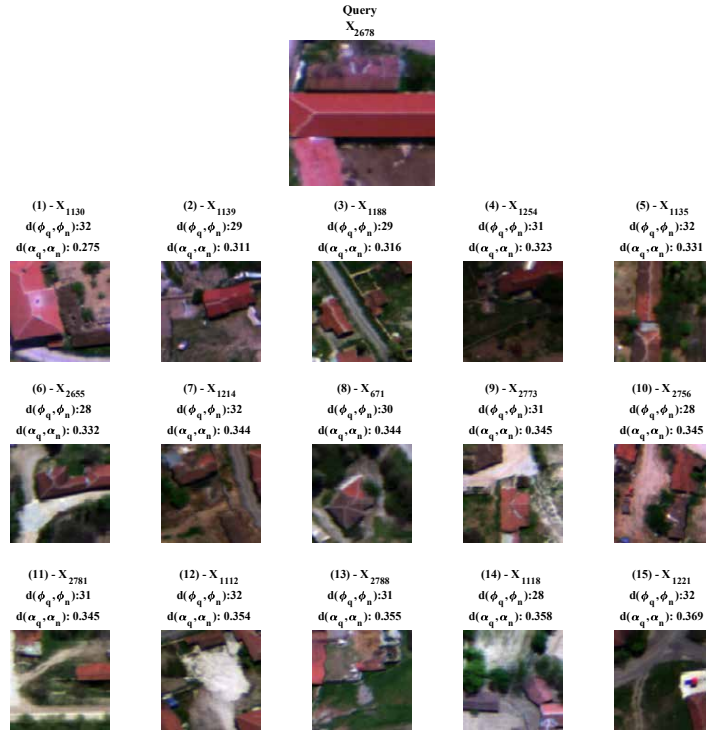


Figure 53: Content-based retrieval result, $X_q = X_{2678}$

Table 13: Content labels for retrieval results, $X_q = X_{2678}$

X_q	1	2	3	4	5	6	7	8	9	10
X_{2678}	X_{1130}	X_{1139}	X_{1188}	X_{1254}	X_{1135}	X_{2655}	X_{1214}	X_{671}	X_{2773}	X_{2756}
red roof tile	red roof tile	red roof tile	red roof tile	red roof tile	red roof tile	red roof tile	red roof tile	red roof tile	red roof tile	red roof tile
bare soil	bare soil	bare soil	bare soil	bare soil	bare soil	bare soil	bare soil	bare soil	bare soil	bare soil
natural veg.	natural veg.	natural veg.	natural veg.	natural veg.	natural veg.	natural veg.	natural veg.	natural veg.	natural veg.	natural veg.
tree	tree	tree	tree	tree	tree	tree	tree	tree	tree	tree
Type-2	Type-2	Type-2	Type-2	Type-2	Type-2	Type-2	Type-2	Type-2	Type-2	Type-2
gravel road	gravel road		gravel road			gravel road	gravel road	gravel road	gravel road	gravel road
metal object		metal object			white painted object	metal object				blue painted object
		white painted object	metal tile	metal tile	metal tile		metal tile			red painted object

The retrieval results presented in Figure 54 and the corresponding content labels given in Table 14 were obtained against a query image that contains a high abundance of background content (e.g., field and bare soil). The retrieval results given in Figure 54 show that the proposed system is capable of retrieving images with similar background contents.

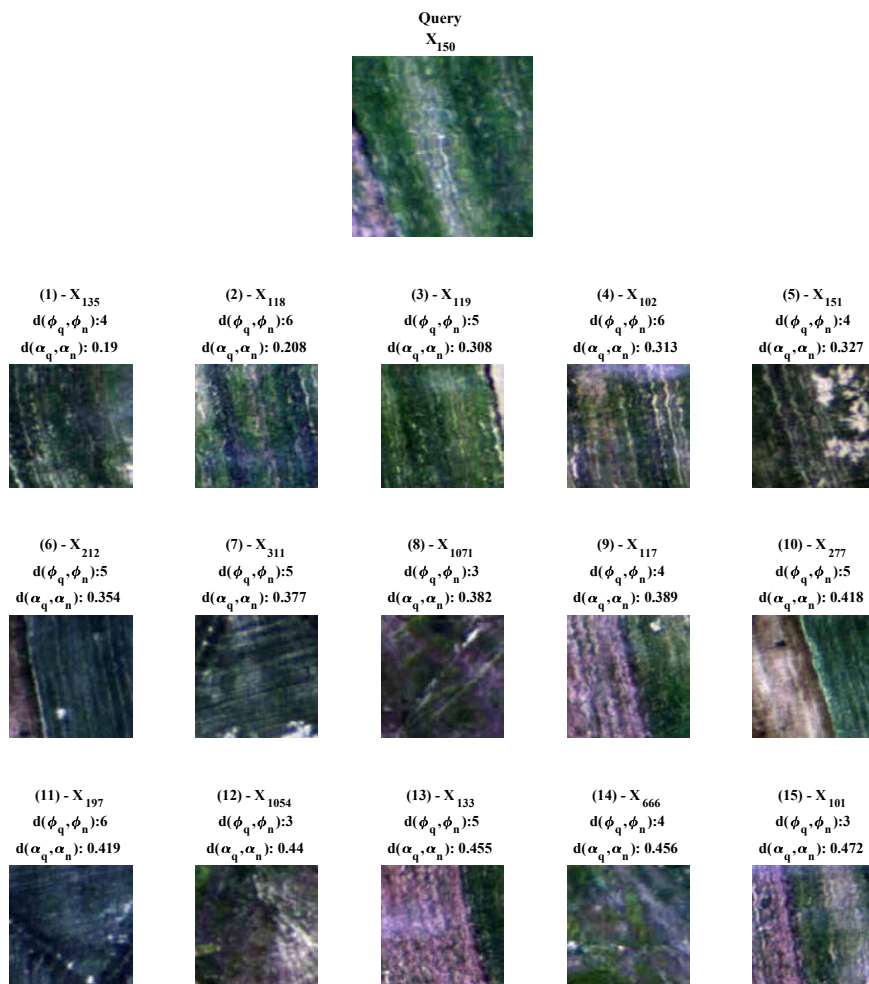


Figure 54: Content-based retrieval result, $X_q = X_{150}$

Table 14: Content labels for retrieval results, $X_q = X_{150}$

X_q	1	2	3	4	5	6	7	8	9	10
X_{125}	X_{135}	X_{118}	X_{119}	X_{102}	X_{151}	X_{212}	X_{311}	X_{1071}	X_{117}	X_{277}
field	field	field	field	field	field	field	field	field	field	field
Type-3	Type-3	Type-3	Type-3	Type-3	Type-3	Type-3	Type-3	Type-3	Type-3	Type-3
bare soil	bare soil	bare soil	bare soil	bare soil	bare soil	bare soil	bare soil	bare soil	bare soil	bare soil

A series of experiments were also performed to observe how the proposed CBHIR system performs the retrieval in the case of query images with different ground-sampling distances (resolutions) and spatial dimensions than the hyperspectral im-

ages in the archive. The retrieval results presented in Figure 55 and the corresponding content labels given in Table 15 were obtained for a query image whose resolution is reduced by a factor of 1/4 in both spatial dimensions. The resulting image has 25x25 pixels in x and y dimensions and the same spectral bands as the original image.

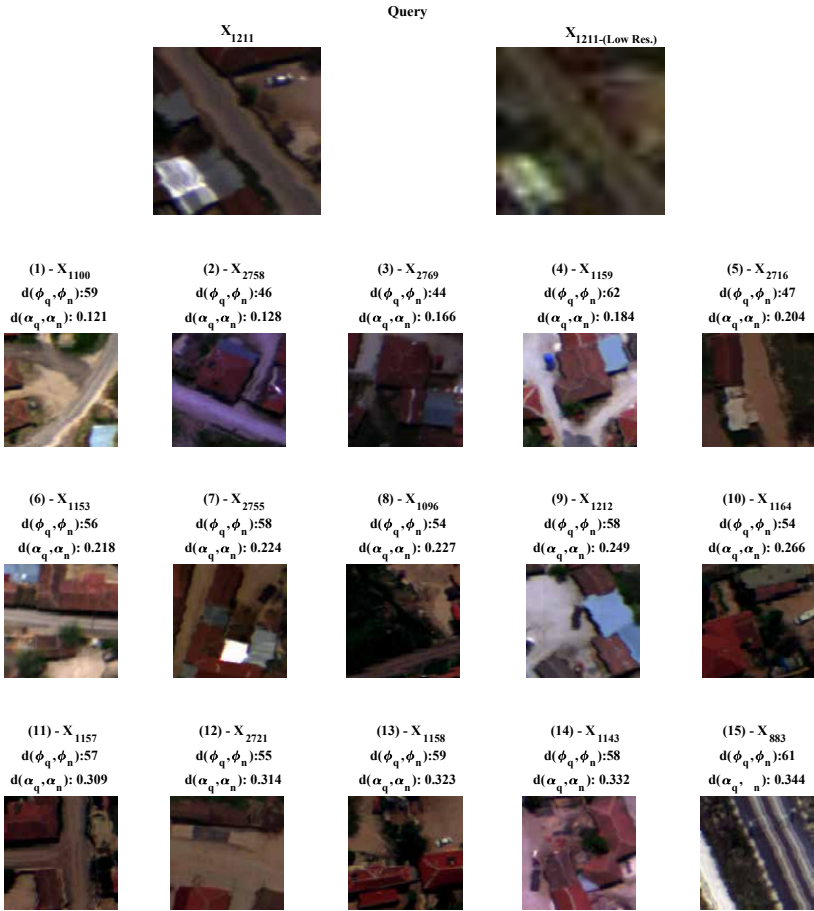


Figure 55: Content-based retrieval result (down-scaled), $X_q = X_{1211}$

Table 15: Content labels for retrieval results (down-scaled), $X_q = X_{1211}$

X_q	1	2	3	4	5	6	7	8	9	10
X_{1211}	X_{1100}	X_{2758}	X_{2769}	X_{1159}	X_{2716}	X_{1153}	X_{2755}	X_{1096}	X_{1212}	X_{1164}
gravel road	gravel road	gravel road	gravel road	gravel road	gravel road			gravel road	gravel road	gravel road
metal sheet	metal sheet	metal sheet	metal sheet	metal sheet	metal sheet	metal sheet	metal sheet		metal sheet	metal sheet
bare soil	bare soil	bare soil	bare soil	bare soil	bare soil	bare soil	bare soil	bare soil	bare soil	metal sheet
red roof tile	red roof tile	red roof tile	red roof tile	red roof tile	red roof tile	red roof tile	red roof tile	red roof tile	red roof tile	red roof tile
white metal object		white metal object	white metal object	white metal object		white metal object	white metal object		white metal object	white metal object
tree	tree	tree	tree	tree		tree	tree		tree	black painted object
natural veg.	natural veg.	natural veg.	natural veg.	natural veg.	natural veg.	natural veg.	natural veg.	natural veg.	natural veg.	natural veg.

Similarly, another experiment was conducted on the same image by increasing the resolution by a factor of 4 in both spatial dimensions. The resulting image has 400x400 pixels in x and y dimensions and the same spectral bands as the original image. The retrieval results for the up-scaled image and the corresponding content labels are given in Figure 56 and Table 16, respectively.

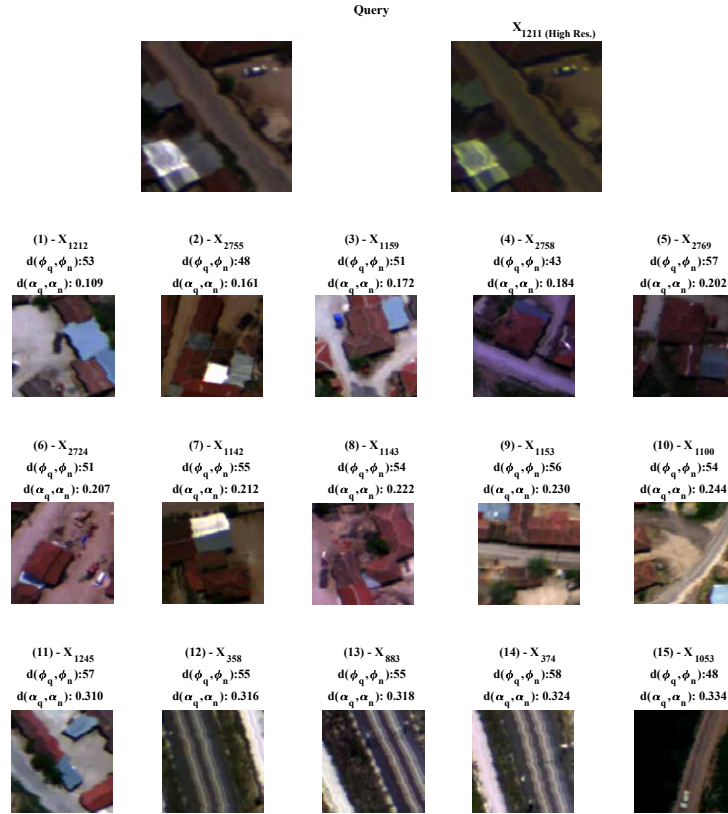


Figure 56: Content-based retrieval result, (down-scaled image) $X_q = X_{1211}$

Table 16: Content labels for retrieval results (up-scaled), $X_q = X_{1211}$

X_q	1	2	3	4	5	6	7	8	9	10
X_{1211}	X_{1212}	X_{2755}	X_{1159}	X_{2758}	X_{2769}	X_{2724}	X_{1142}	X_{1143}	X_{1153}	X_{1100}
gravel road			gravel road	gravel road	gravel road	gravel road		gravel road	gravel road	gravel road
metal sheet	metal sheet	metal sheet	metal sheet	metal sheet	metal sheet	metal sheet	metal sheet		metal sheet	metal sheet
bare soil	bare soil	bare soil	bare soil	bare soil	bare soil	bare soil	bare soil	bare soil	bare soil	metal sheet
red roof tile	red roof tile	red roof tile	red roof tile	red roof tile	red roof tile	red roof tile	red roof tile	red roof tile	red roof tile	red roof tile
white metal object	white metal object	white metal object	white metal object	white metal object	white metal object	white metal object			white metal object	
tree	tree	tree	tree	tree	tree	tree			tree	black painted object
natural veg.	natural veg.	natural veg.	natural veg.	natural veg.	natural veg.	natural veg.	natural veg.	natural veg.	natural veg.	natural veg.

The retrieval results shown in Figure 57 and the corresponding content labels given in Table 17 were obtained for an image query that had its resolution reduced by a factor of 1/4 in both spatial dimensions. The resulting image has 25x25 pixels in both x and y dimensions and the same spectral bands as the original image.

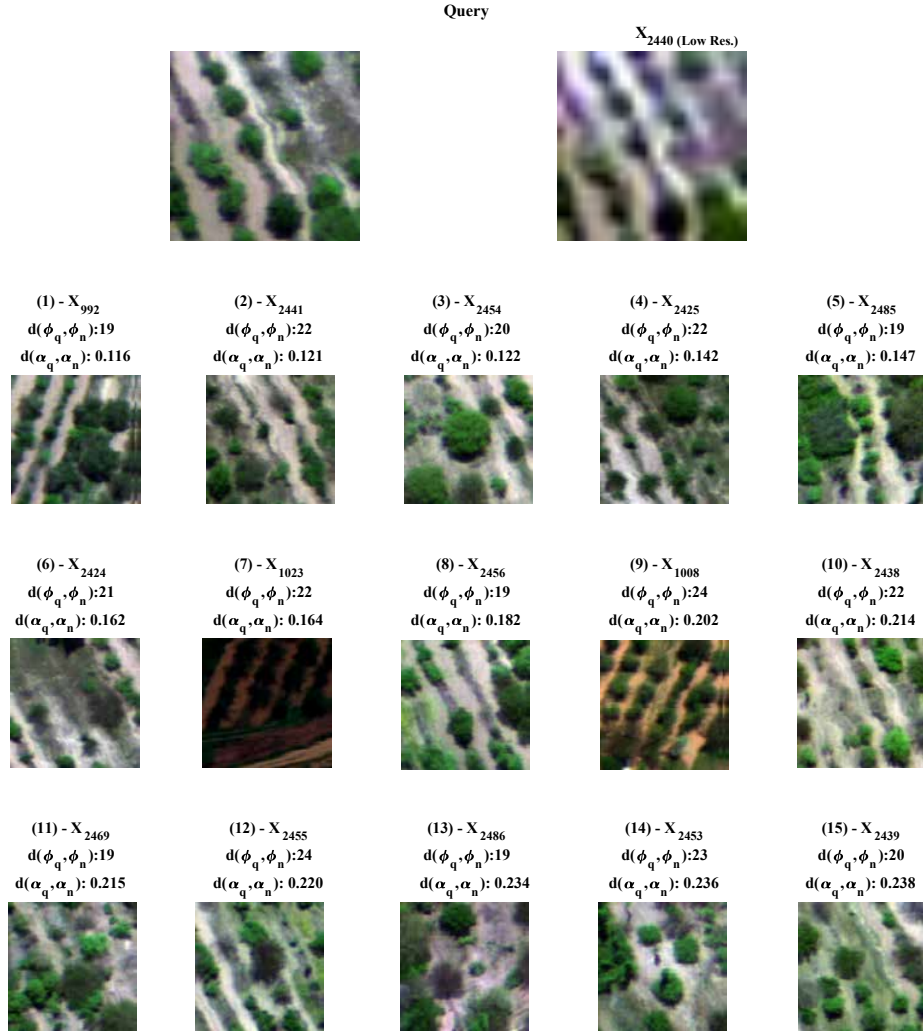


Figure 57: Content-based retrieval result (down-scaled image), $X_q = X_{2440}$

Table 17: Content labels for retrieval results (down-scaled image), $X_q = X_{2440}$

X_q	1	2	3	4	5	6	7	8	9	10
X_{2440}	X_{992}	X_{2441}	X_{2454}	X_{2425}	X_{2485}	X_{2424}	X_{1023}	X_{2456}	X_{1008}	X_{2438}
tree	tree	tree	tree	tree	tree	tree	tree	tree	tree	tree
Type-3	Type-3	Type-3	Type-3	Type-3	Type-3	Type-3	Type-3	Type-3	Type-3	Type-3
bare soil	bare soil	bare soil	bare soil	bare soil	bare soil	bare soil	bare soil	bare soil	bare soil	bare soil
natural veg.	natural veg.	natural veg.	natural veg.	natural veg.	natural veg.	natural veg.	natural veg.	natural veg.	natural veg.	natural veg.

In another experiment, the resolution of the same image was increased four times in both the x and y dimensions. The resulting image now has 400x400 pixels in both dimensions and has the same spectral bands as the original image. The results of the retrieval process for this up-scaled image, along with the corresponding content labels, are presented in Figure 58 and Table 18, respectively.

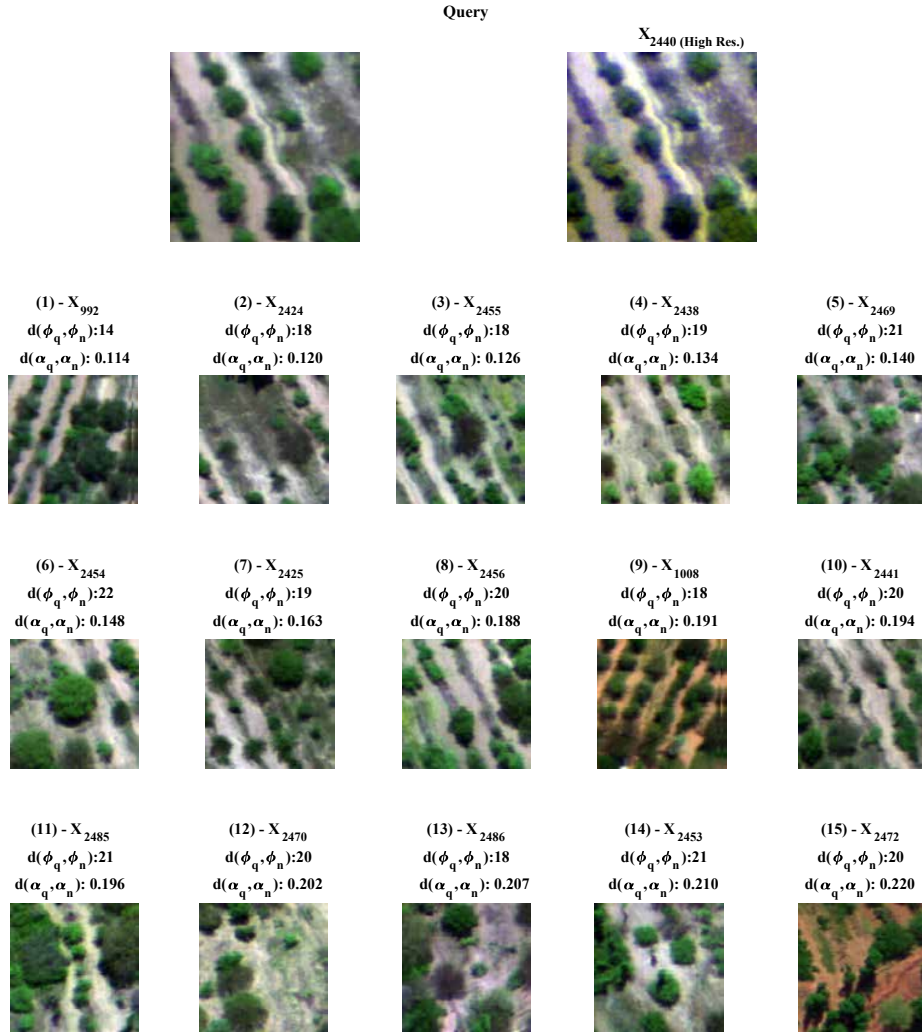


Figure 58: Content-based retrieval result (up-scaled image), $X_q = X_{2440}$

Table 18: Content labels for retrieval results (down-scaled image), $X_q = X_{2440}$

X_q	1	2	3	4	5	6	7	8	9	10
X_{2440}	X_{992}	X_{2424}	X_{2455}	X_{2438}	X_{2469}	X_{2454}	X_{2425}	X_{2456}	X_{1008}	X_{2441}
tree	tree	tree	tree	tree	tree	tree	tree	tree	tree	tree
Type-3	Type-3	Type-3	Type-3	Type-3	Type-3	Type-3	Type-3	Type-3	Type-3	Type-3
bare soil	bare soil	bare soil	bare soil	bare soil	bare soil	bare soil	bare soil	bare soil	bare soil	bare soil
natural veg.	natural veg.	natural veg.	natural veg.	natural veg.	natural veg.	natural veg.	natural veg.	natural veg.	natural veg.	natural veg.

The results demonstrate that when the query image has a higher ground-sampling distance (lower spatial resolution) than the images in the archive, the retrieval performance of the system is affected since the segments extracted from the query image in the feature extraction step represent mixed pixel signatures which are not directly represented by a term in the vocabularies. Due to the unavailability of relevant spectral terms for certain segments in the query image, the overall system performance is negatively impacted. For instance, the white-painted object (car), located in the top-right section of the image, in Figure 55 disappears when the resolution of the image is reduced by a factor of 1/4. Thus, the pixels representing the white-painted object intervene with the surrounding pixels containing bare soil.

On the other hand, it is also observed that upscaling the spatial dimensions of the query image does not remarkably affect the system’s performance if the segment window size required in the hyperSLIC algorithm remains the same.

7.5 Comparative Performance Analysis

In order to measure the retrieval performance of the system in this regard, each hyperspectral image X_n in X was used as query hyperspectral image to retrieve 10 hyperspectral images that contain similar materials. It is worth noting that while the proposed system performs retrieval based on overall content, other CBHIR systems perform retrieval based on the strategy they built on.

In terms of accuracy, the proposed CBHIR system shows the best performance among all CBHIR systems if the retrieval is performed with both foreground and background content descriptors. On the other hand, the proposed CBHIR system has the highest scores for precision, recall, and Hamming loss in case the retrieval is performed with foreground content descriptors.

Table 19: Performance evaluation of CBHIR systems.

CBHIR SYSTEM	Method	Accuracy (%)	Precision (%)	Recall (%)	Hamming Loss	Retrieval Time (ms)
Previously Proposed BoE Based System	BSD-SSR	64.82	76.03	74.17	6.02	0.114
	BSAD-TSHR	66.43	63.22	73.48	6.21	0.129
Proposed CBHIR System	Overall-SSR	76.65	84.28	85.54	4.48	0.146
	Overall-TSHR	82.20	83.25	82.43	5.21	0.159
Em-Grana		58.47	61.26	64.25	7.03	83.442
EM-WSAD		51.47	54.18	57.18	9.44	18756.36

In the experiments, the proposed CBHIR system was examined for the retrieval Scenario 3 and the Scenario 4 explained in Chapter 1. When Scenario 3 is considered, single-stage retrieval (SSR) is applied to the images represented by the binary spectral content descriptors (BSD). In order to evaluate the performance of the proposed CBHIR system, we have considered two state-of-the-art methods for comparison: 1) the

endmember matching algorithm based on the Grana Distance (denoted as EM-Grana); and 2) the endmember matching algorithm that weights the distances estimated by the SAD between each endmember pair by their abundances (denotes as EM-WSAD).

Comparative performance results show that the proposed system performs the retrieval with the highest accuracy (82.20%) in case both spectral and abundance descriptors are utilized by considering overall image content. On the other, while the proposed system has the highest precision (84.28%) and recall (85.54%) values, similarly, the lowest Hamming Loss score also belongs to the proposed algorithm when the retrieval is performed with respect to the spectral descriptor only.

On the other hand, it has been observed that the proposed CBHIR system exhibits an increase in retrieval time compared to the previously suggested bag-of-endmember based CBHIR system. This is because the descriptor vector lengths in the proposed CBHIR system are longer than those calculated in the previously suggested bag-of-endmember based CBHIR system system.

CHAPTER 8

CONCLUSION AND FUTURE WORK

This final chapter comprehensively analyzes the proposed Content-Based Image Retrieval (CBHIR) system. The methodology behind the development of the system is discussed by highlighting its key features and benefits. In addition, a detailed account of the system's performance results is concluded, demonstrating its ability to retrieve images based on their content accurately. In the future work section, comments and suggestions regarding the suggested improvements for the CBHIR system developed within the scope of the thesis are shared.

8.1 Conclusion

Hyperspectral imaging has become an increasingly prevalent passive optical remote sensing technique used across various fields to solve many problems, such as identifying plant diseases in precision agriculture or detecting buried objects in military operations. This remote sensing technique is particularly useful in applications that require observation of unique spectral features.

The most notable advantage of hyperspectral imaging, which distinguishes this remote sensing technique from other passive optical remote sensing methods, is the abundance of information provided in the spectral domain. By capturing a large number of observation channels at consecutive wavelengths, hyperspectral imaging allows for precise recognition and discrimination of objects in a scene. This makes hyperspectral remote sensing an invaluable tool in various fields. However, the dense spectral information in hyperspectral imagery also generates more data to be processed than other optical imaging techniques. Additionally, the vast amount of data generated in imaging campaigns may pose challenges when it comes to effectively utilizing hyperspectral images for interpretation and management purposes. Depending on the application requirements, this fact may limit the potential benefits that can be obtained from hyperspectral imagery. Therefore, accurate and fast retrieval of hyperspectral images from image collections, in the context of spectral properties of the matters, is one of the critical tasks in remote sensing.

Several content-based hyperspectral image retrieval (CBHIR) systems have been proposed in the literature. These methods aim to facilitate the retrieval of relevant hyperspectral images from hyperspectral archives by exploiting the spectral information

contained in the images. However, these methods have some common limitations listed below that affect the accurate retrieval of hyperspectral imagery.

1. Spectral information redundancy in archive images reduces retrieval performance due to dominant background content.
2. CBHIR methods that model hyperspectral images by only endmembers may not accurately extract the endmembers from the images, or pure material signatures may not exist in the scene.
3. Strategies (i.e., bag-of-endmembers) that aim at combining and clustering all endmembers to generate a global spectral vocabulary to model hyperspectral images may ignore spectral signatures (endmember) of rarely seen content in case of using an inappropriate clustering method or setting parameters of clustering method inaccurately.

To address these issues, this thesis proposes a novel content-based hyperspectral image retrieval (CBHIR) system to define global hyperspectral image representations based on a semantic approach to differentiate foreground and background image content for different retrieval scenarios. Two spectral content dictionaries are utilized to model hyperspectral images. The first dictionary consists of spectral terms related to materials seldom present in the relevant geographical region, known as foreground content. On the other hand, the second dictionary includes spectral terms for materials frequently observed in the geographical region, known as background content.

The proposed system consists of two main modules. The first module characterizes the query and the target hyperspectral images in the archive by four global descriptors: 1) two binary spectral descriptors (which represent spectral characteristics of distinct foreground and background materials); 2) two abundance descriptors (which model normalized cumulative fractional abundance of the corresponding materials). The second module retrieves hyperspectral images from the archive that cover materials most similar to the given query signature or query image based on a hierarchical strategy that evaluates the spectral and abundance descriptor similarity.

To evaluate the retrieval performance of the proposed CBHIR system and to compare it with state-of-the-art systems available in the literature, a multi-label benchmark hyperspectral image archive was created from high-resolution airborne hyperspectral remote sensing data products. Experiments carried out on this benchmark archive of hyperspectral images demonstrated the effectiveness of the proposed system in terms of retrieval accuracy and time.

Upon conducting a thorough analysis of the findings, it has been determined that the suggested system outperforms the traditional method of utilizing solely endmembers for retrieving hyperspectral images from an archive. The suggested system incorporates spatial and spectral relationships in content segments to model content types. These outcomes underscore the significant benefits of the suggested system when compared to the conventional approaches. By considering both spatial and spectral properties, the proposed system enables more accurate modeling of the content types

present in the hyperspectral imagery. In contrast, the conventional approach of using only endmembers may result in insufficient models that fail to capture the required content representation in hyperspectral imagery. Therefore, the proposed system is a more effective and sophisticated approach to accessing hyperspectral images in remote sensing archives.

Although the proposed CBHIR system exhibits higher retrieval performance than other systems during the experimental process, it also has certain limitations. The first is the input requirement from the user in modeling background content; even though this process is carried out in a semi-supervised manner, it is believed that fully unsupervised foreground and background content discrimination would positively impact the system's performance. Another observed limitation of the proposed system is the use of Hamming distance in comparing spectral descriptors. Hamming distance evaluates two spectral descriptor vectors in a binary manner, assigning a penalty score for each spectral term that is not common between the two vectors. This may pose a problem, particularly when comparing spectral vectors of images rich in content diversity and abundance. In addition to these limitations, proper specification of some parameters is a critical step affecting the overall system performance. For instance, the segment size required by the hyperSLIC algorithm should be chosen properly considering the ground-sampling distance of the imager and the minimum foreground segment size required by the task to be performed.

The proposed system has also been tested for query images with different ground-sampling distances (resolutions) and spatial dimensions than the hyperspectral images in the archive. The results demonstrated that when the query image has a different ground-sampling distance (higher spatial resolution), the system's overall performance is affected since the segments obtained in the feature extraction and vocabulary generation steps may represent different materials in the same location. For instance, if the ground-sampling distance of the query image gets higher, this results in obtaining segments that consist of mixed pixels. On the other hand, it is also observed that an increase in the spatial dimension of the query image does not affect the system's performance if the segment window size in the hyperSLIC algorithm remains the same.

Finally, the data labeling process of the hyperspectral images used in the benchmark archive also influences the performance results. Although VHR aerial photographs were used to label the images in the benchmark archive created within the scope of this study, it is believed that the labeling process can be improved with additional information obtained from the field.

8.2 Future Work

Although the proposed method has demonstrated a superior retrieval success rate compared to other methods found in the existing literature, certain aspects require additional development to make it more versatile and adaptable to a broad range of use cases.

The following improvements to the proposed system should be studied as future work.

- Comparing spectral descriptor vectors in a binary manner and assigning a penalty score for each non-common term provides a robust comparison in retrieving images with relatively less content and a homogeneous structure. However, it can pose challenges when comparing images with a richer diversity of content. For this reason, it is believed that introducing a similarity measure that allows penalty scoring relative to Hamming distance, as an alternative to Hamming distance, would positively impact the retrieval performance.
- Beyond classifying image content as foreground and background, identifying subclasses within these classes that are important to users. For instance, differences may arise in some types of content due to variations in time and environmental conditions (e.g., tiles exposed to sunlight at different angles on the same roof). This situation is defined as a distinct content and characterized by a different spectral term due to changes in the chemical structures of materials over time. It is believed that modeling image content types with a taxonomic approach would positively overcome this issue.
- Utilizing payload and altitude information as input in the proposed system's segmentation phase method would provide a significant advantage in modeling image contents at various spatial resolutions without needing any specific input.
- The proposed CBHIR system has the potential to benefit a wide range of users in various applications. To maximize its potential, it is highly recommended to implement a cloud-based application that can cater to the varying needs of different users. Such an application would allow users to access the system from different locations and devices, making it more convenient and flexible. Additionally, hosting the application on the cloud would enable users to take advantage of the scalability and reliability of cloud services, ensuring that the system can handle increasing demands in the future. Overall, a cloud-based application for the CBHIR system would greatly enhance its usability and accessibility, making it a valuable tool for various usage scenarios.

REFERENCES

- [1] X. Tong, H. Xie, and Q. Weng, “Urban land cover classification with airborne hyperspectral data: What features to use?,” *IEEE Journal of Selected Topics in Applied Earth Observations and Remote Sensing*, vol. 7, no. 10, pp. 3998–4009, 2014.
- [2] R. N. Clark, G. A. Swayze, I. Leifer, K. E. Livo, R. Kokaly, T. Hoefen, S. Lundeen, M. Eastwood, R. O. Green, N. Pearson, *et al.*, “A method for quantitative mapping of thick oil spills using imaging spectroscopy,” *US Geological Survey Open-File Report*, vol. 1167, no. 2010, pp. 1–51, 2010.
- [3] A. Ertürk, M.-D. Iordache, and A. Plaza, “Sparse unmixing-based change detection for multitemporal hyperspectral images,” *IEEE Journal of Selected Topics in Applied Earth Observations and Remote Sensing*, vol. 9, no. 2, pp. 708–719, 2016.
- [4] C. Camino, V. González-Dugo, P. Hernández, J. Sillero, and P. J. Zarco-Tejada, “Improved nitrogen retrievals with airborne-derived fluorescence and plant traits quantified from vnir-swir hyperspectral imagery in the context of precision agriculture,” *International Journal of Applied Earth Observation and Geoinformation*, vol. 70, pp. 105–117, 2018.
- [5] F. Omruuzun, D. O. Baskurt, H. Daglayan, and Y. Y. Cetin, “Utilizing hyperspectral remote sensing imagery for afforestation planning of partially covered areas,” in *Image and Signal Processing for Remote Sensing XXI* (L. Bruzzone, ed.), vol. 9643, p. 96432N, International Society for Optics and Photonics, SPIE, 2015.
- [6] F. D. van der Meer, H. M. van der Werff, F. J. van Ruitenbeek, C. A. Hecker, W. H. Bakker, M. F. Noomen, M. van der Meijde, E. J. M. Carranza, J. B. de Smeth, and T. Woldai, “Multi- and hyperspectral geologic remote sensing: A review,” *International Journal of Applied Earth Observation and Geoinformation*, vol. 14, no. 1, pp. 112–128, 2012.
- [7] C. Mielke, C. Rogass, N. Boesche, K. Segl, and U. Altenberger, “Engeomap 2.0—automated hyperspectral mineral identification for the german enmap space mission,” *Remote Sensing*, vol. 8, no. 2, 2016.
- [8] W. Hua, T. Guo, and X. Liu, “Camouflage target reconnaissance based on hyperspectral imaging technology,” in *2015 International Conference on Optical Instruments and Technology: Optoelectronic Imaging and Processing Technology* (G. Shi, X. Li, and B. Huang, eds.), vol. 9622, p. 962217, International Society for Optics and Photonics, SPIE, 2015.
- [9] P. Babington, *Hyperspectral Remote Sensing*. SPIE Bellingham.

- [10] T. Kato, “Database architecture for content-based image retrieval,” in *Image Storage and Retrieval Systems* (A. A. Jamberdino and C. W. Niblack, eds.), vol. 1662, pp. 112 – 123, International Society for Optics and Photonics, SPIE, 1992.
- [11] DigitalGlobe, *WorldView-1 Relative Radiometric Response Curve*, (accessed August 8, 2017). https://dg-cms-uploads-production.s3.amazonaws.com/uploads/document/file/228/RSR_WorldView-1.pdf.
- [12] DigitalGlobe, *WorldView-2 Relative Radiometric Response Curve*, (accessed August 8, 2017). https://dg-cms-uploads-production.s3.amazonaws.com/uploads/document/file/242/relative_spectral_response_WV4.pdf.
- [13] H. J. Kramer, *Survey of Airborne Sensors*, pp. 303–464. Berlin, Heidelberg: Springer Berlin Heidelberg, 1994.
- [14] J. R. Irons, P. W. Dabney, J. Paddon, R. R. Irish, and C. A. Russell, “Advanced Solid-State Array Spectroradiometer support of 1989 field experiments,” in *Imaging Spectroscopy of the Terrestrial Environment* (G. Vane, ed.), vol. 1298, pp. 2 – 10, International Society for Optics and Photonics, SPIE, 1990.
- [15] R. O. Green, M. L. Eastwood, C. M. Sarture, T. G. Chrien, M. Aronsson, B. J. Chippendale, J. A. Faust, B. E. Pavri, C. J. Chovit, M. Solis, M. R. Olah, and O. Williams, “Imaging spectroscopy and the airborne visible/infrared imaging spectrometer (aviris),” *Remote Sensing of Environment*, vol. 65, no. 3, pp. 227–248, 1998.
- [16] NASA, *AVIRIS Data Portal*, (accessed December 22, 2017). https://aviris.jpl.nasa.gov/alt_locator/.
- [17] L. J. Rickard, R. W. Basedow, E. F. Zalewski, P. R. Silverglate, and M. Landers, “HYDICE: an airborne system for hyperspectral imaging,” in *Imaging Spectrometry of the Terrestrial Environment* (G. Vane, ed.), vol. 1937, pp. 173 – 179, International Society for Optics and Photonics, SPIE, 1993.
- [18] P. A. Mitchell, “Hyperspectral digital imagery collection experiment (HYDICE),” in *Geographic Information Systems, Photogrammetry, and Geological/Geophysical Remote Sensing* (J. B. Lurie, J. J. Pearson, and E. Zilioli, eds.), vol. 2587, pp. 70 – 95, International Society for Optics and Photonics, SPIE, 1995.
- [19] L. Rousset-Rouviere, C. Coudrain, S. Fabre, I. Baarstad, A. Fridman, T. Løke, S. Blaaberg, and T. Skauli, “Sysiphe, an airborne hyperspectral imaging system for the vnir-swir-mwir-lwir region,” in *Proc. 7th EARSeL Workshop on Imaging Spectroscopy*, pp. 1–12, 2011.
- [20] R. Pu, *Hyperspectral Remote Sensing: Fundamentals and Practices*. CRC Press, 2017.

- [21] S. R. Sandor-Leahy, D. Beiso, M. A. Figueroa, M. A. Folkman, D. A. Gleichauf, T. R. Hedman, P. J. Jarecke, and S. Thordarson, “TRWIS III hyperspectral imager: instrument performance and remote sensing applications,” in *Imaging Spectrometry IV* (M. R. Descour and S. S. Shen, eds.), vol. 3438, pp. 13 – 22, International Society for Optics and Photonics, SPIE, 1998.
- [22] M. A. Voelker, R. G. Resmini, G. C. Mooradian, T. B. McCord, C. P. Warren, M. W. Fene, C. C. Coyle, and R. Anderson, “Advanced Airborne Hyperspectral Imaging System (AAHIS): an imaging spectrometer for maritime applications,” in *Imaging Spectrometry* (M. R. Descour, J. M. Mooney, D. L. Perry, and L. R. Illing, eds.), vol. 2480, pp. 357 – 367, International Society for Optics and Photonics, SPIE, 1995.
- [23] P. Strobl, A. A. Mueller, D. Schlaepfer, and M. E. Schaepman, “Laboratory calibration and inflight validation of the Digital Airborne Imaging Spectrometer DAIS 7915,” in *Algorithms for Multispectral and Hyperspectral Imagery III* (A. E. Iverson and S. S. Shen, eds.), vol. 3071, pp. 225 – 236, International Society for Optics and Photonics, SPIE, 1997.
- [24] S. Holzwarth, A. Muller, M. Habermeyer, R. Richter, A. Hausold, S. Thiemann, and P. Strobl, “Hysens-dais 7915/rosis imaging spectrometers at dlr,” in *Proceedings of the 3rd EARSeL Workshop on Imaging Spectroscopy*, pp. 3–14, 2003.
- [25] B. Stevenson, R. O’Connor, W. Kendall, A. Stocker, W. Schaff, D. Alexa, J. Salvador, M. Eismann, K. Barnard, and J. Kershenstein, “Design and performance of the Civil Air Patrol ARCHER hyperspectral processing system,” in *Algorithms and Technologies for Multispectral, Hyperspectral, and Ultraspectral Imagery XI* (S. S. Shen and P. E. Lewis, eds.), vol. 5806, pp. 731 – 742, International Society for Optics and Photonics, SPIE, 2005.
- [26] C. G. Simi, E. M. Winter, M. M. Williams, and D. C. Driscoll, “Compact Airborne Spectral Sensor (COMPASS),” in *Algorithms for Multispectral, Hyperspectral, and Ultraspectral Imagery VII* (S. S. Shen and M. R. Descour, eds.), vol. 4381, pp. 129 – 136, International Society for Optics and Photonics, SPIE, 2001.
- [27] Itres, *CASI-1500*, (accessed October 26, 2017). http://www.itres.com/wp-content/uploads/2014/10/CASI_1500H1.pdf.
- [28] R. Vaughan, W. M. Calvin, and J. V. Taranik, “Sebas hyperspectral thermal infrared data: surface emissivity measurement and mineral mapping,” *Remote Sensing of Environment*, vol. 85, no. 1, pp. 48–63, 2003.
- [29] S. J. Young, B. R. Johnson, and J. A. Hackwell, “An in-scene method for atmospheric compensation of thermal hyperspectral data,” *Journal of Geophysical Research: Atmospheres*, vol. 107, no. D24, pp. ACH 14–1–ACH 14–20, 2002.
- [30] B. Stevenson, R. O’Connor, W. Kendall, A. Stocker, W. Schaff, D. Alexa, J. Salvador, M. Eismann, K. Barnard, and J. Kershenstein, “Design and performance of the Civil Air Patrol ARCHER hyperspectral processing system,” in

- Algorithms and Technologies for Multispectral, Hyperspectral, and Ultraspectral Imagery XI* (S. S. Shen and P. E. Lewis, eds.), vol. 5806, pp. 731 – 742, International Society for Optics and Photonics, SPIE, 2005.
- [31] J. Marmo, M. A. Folkman, C. Y. Kuwahara, and C. T. Willoughby, “Lewis hyperspectral imager payload development,” in *Imaging Spectrometry II* (M. R. Descour and J. M. Mooney, eds.), vol. 2819, pp. 80 – 90, International Society for Optics and Photonics, SPIE, 1996.
- [32] J. Dozier, “HIRIS - The High Resolution Imaging Spectrometer,” in *Recent Advances in Sensors, Radiometry, and Data Processing for Remote Sensing* (P. N. Slater, ed.), vol. 0924, pp. 23 – 30, International Society for Optics and Photonics, SPIE, 1988.
- [33] A. Goetz and M. Herring, “The high resolution imaging spectrometer (hiris) for eos,” *IEEE Transactions on Geoscience and Remote Sensing*, vol. 27, no. 2, pp. 136–144, 1989.
- [34] F. Blechinger, D. E. Charlton, R. Davancens, B. Harnisch, B. P. Kunkel, R. Meynart, A. Novi, E. O’Mongain, H. H. Schwarzer, and P. N. Slater, “High-resolution imaging spectrometer (HRIS): optics, focal plane, and calibration,” in *Imaging Spectrometry of the Terrestrial Environment* (G. Vane, ed.), vol. 1937, pp. 207 – 224, International Society for Optics and Photonics, SPIE, 1993.
- [35] E. Roberts, J. Huntington, and R. Denize, “The australian resource information and environment satellite (aries), phase a study,” 1997.
- [36] S. Yarbrough, T. R. Caudill, E. T. Kouba, V. Osweiler, J. Arnold, R. Quarles, J. Russell, L. J. O. III, B. A. Jones, A. Edwards, J. Lane, A. D. Meigs, R. B. Lockwood, and P. S. Armstrong, “MightySat II.1 hyperspectral imager: summary of on-orbit performance,” in *Imaging Spectrometry VII* (M. R. Descour and S. S. Shen, eds.), vol. 4480, pp. 186 – 197, International Society for Optics and Photonics, SPIE, 2002.
- [37] J. Pearlman, C. Segal, L. B. Liao, S. L. Carman, M. A. Folkman, W. Browne, L. Ong, and S. G. Ungar, “Development and operations of the EO-1 Hyperion Imaging Spectrometer,” in *Earth Observing Systems V* (W. L. Barnes, ed.), vol. 4135, pp. 243 – 253, International Society for Optics and Photonics, SPIE, 2000.
- [38] USGS, *EarthExplorer*, (accessed December 12, 2017). <https://earthexplorer.usgs.gov>.
- [39] B. Van Mol, K. Ruddick, *et al.*, “The compact high resolution imaging spectrometer (chris): the future of hyperspectral satellite sensors. imagery of oostende coastal and inland waters,” in *Proceedings of the Airborne Imaging Spectroscopy workshop*, Brugge, 2004.
- [40] M. Cutter and D. Lobb, “Design of the compact high-resolution imaging spectrometer (CHRIS), and future developments,” in *International Conference on*

Space Optics — ICSO 2004 (J. Costeraste and E. Armandillo, eds.), vol. 10568, p. 1056805, International Society for Optics and Photonics, SPIE, 2004.

- [41] ESA, *Earth Online*, (accessed December 12, 2017). <https://earth.esa.int>.
- [42] NASA, “Spacecraft icons - nasa science,” (accessed August 6, 2017). <https://science.nasa.gov/multimedia-galleries/spacecraft-icons/>.
- [43] H. Sun, J. Wu, S. Dai, B. Zhao, and R. Shu, “Introduction to the payloads and the initial observation results of chang’e-1,” *Chinese Journal of Space Science*, vol. 28, no. 5, pp. 374–384, 2008.
- [44] O. Ziyuan, J. Jingshan, L. Chunlai, S. Huixian, Z. Yongliao, L. Jianzhong, L. Jianjun, Z. Baochang, R. Xin, Y. Jianfeng, *et al.*, “Preliminary scientific results of chang e-1 lunar orbiter: Based on payloads detection data in the first phase,” *Journal of Space Science*, vol. 28, no. 5, pp. 361–369, 2008.
- [45] A. Kiran Kumar, A. Roy Chowdhury, K. Murali, S. Sarkar, S. Joshi, S. Mehta, A. Dave, K. Shah, A. Banerjee, K. Mathew, *et al.*, “The hyper spectral imager instrument on chandrayaan-1,” in *Lunar and Planetary Science Conference*, vol. 40, 2009.
- [46] ISRO, *Overview of Chandrayaan-1 Mission*, (accessed October 22, 2017). <http://www.isro.gov.in/pslv-c11-chandrayaan-1/overview-of-chandrayaan-1-mission>.
- [47] NASA, *Moon Mineralogy Mapper (M³)*, (accessed October 22, 2017). https://solarsystem.nasa.gov/moon/newsdisplay.cfm?Subsite_News_ID=49330&SiteID=6&iSiteID=1.
- [48] L. Zhang, Y. Liu, and X. Zhang, “Progress in chinese satellite hyperspectral missions,” in *IEEE IGARSS*, 2014.
- [49] L. Liu, J. Feng, B. Rivard, X. Xu, J. Zhou, L. Han, J. Yang, and G. Ren, “Mapping alteration using imagery from the tiangong-1 hyperspectral spaceborne system: Example for the jintanzi gold province, china,” *International Journal of Applied Earth Observation and Geoinformation*, vol. 64, pp. 275–286, 2018.
- [50] R. Lockwood, T. Cooley, R. Nadile, J. Gardner, P. Armstrong, A. Payton, T. Davis, S. Straight, T. Chrien, E. Gussin, and D. Makowski, “Advanced responsive tactically-effective military imaging spectrometer (artemis) design,” in *2006 IEEE International Symposium on Geoscience and Remote Sensing*, pp. 1628–1630, 2006.
- [51] NASA, *Tacsat-3*, (accessed August 6, 2017). <https://www.nasa.gov/centers/wallops/missions/tacsat3.html>.

- [52] G. Kerr, J. Avbelj, E. Carmona, A. Eckardt, B. Gerasch, L. Graham, B. Günther, U. Heiden, D. Krutz, H. Krawczyk, A. Makarau, R. Miller, R. Müller, R. Perkins, and I. Walter, “The hyperspectral sensor desis on muses: Processing and applications,” in *2016 IEEE International Geoscience and Remote Sensing Symposium (IGARSS)*, pp. 268–271, 2016.
- [53] DLR, *DESI* - *Hyperspectral Sensor for MUSES*, (accessed October 22, 2017). http://www.dlr.de/os/en/desktopdefault.aspx/tabid-9294/16011_read-39367/.
- [54] E. C. Ray Perkins, Rupert Müller, *The DESIS Hyperspectral Instrument: A New Space-Based Tool for Coastal Zone Monitoring*, (accessed October 22, 2017). <https://coast.noaa.gov/data/docs/geotools/2017/presentations/Perkins.pdf>.
- [55] T. Matsunaga, A. Iwasaki, S. Tsuchida, J. Tanii, O. Kashimura, R. Nakamura, H. Yamamoto, T. Tachikawa, and S. Rokugawa, “Current status of hyperspectral imager suite (hisui),” in *2013 IEEE International Geoscience and Remote Sensing Symposium - IGARSS*, pp. 3510–3513, July 2013.
- [56] T. Matsunaga, S. Yamamoto, O. Kashimura, T. Tachikawa, K. Ogawa, A. Iwasaki, S. Tsuchida, and N. Ohgi, “Operation plan study for japanese future hyperspectral mission: Hisui,” in *Proc. 34th International Symposium on Remote Sensing of Environment. Tucson: ISRSE*, 2011.
- [57] M. Communications, *GHGSat Imaging Spectrometer Payload Delivered*, (accessed October 22, 2017). http://www.mpbcommunications.com/en/site/news/news_releases/stories/GHGSat.html.
- [58] A. Barducci, P. Marcoionni, and I. Pippi, “Recent advances in earth remote sensing: Fourier transform stationary hyperspectral imagers,” *Annals of Geophysics*, vol. 49, no. 1, 2006.
- [59] GHGSat, *CLAIRE’S LAUNCH!*, (accessed October 22, 2017). http://www.ghgsat.com/?page_id=142.
- [60] K. Karalas, G. Tsagkatakis, M. Zervakis, and P. Tsakalides, “Land classification using remotely sensed data: Going multilabel,” *IEEE Transactions on Geoscience and Remote Sensing*, vol. 54, no. 6, pp. 3548–3563, 2016.
- [61] F. Jahan, J. Zhou, M. Awrangjeb, and Y. Gao, “Fusion of hyperspectral and lidar data using discriminant correlation analysis for land cover classification,” *IEEE Journal of Selected Topics in Applied Earth Observations and Remote Sensing*, vol. 11, pp. 3905–3917, Oct 2018.
- [62] N. Chang, B. Vannah, and Y. Jeffrey Yang, “Comparative sensor fusion between hyperspectral and multispectral satellite sensors for monitoring microcystin distribution in lake erie,” *IEEE Journal of Selected Topics in Applied Earth Observations and Remote Sensing*, vol. 7, pp. 2426–2442, June 2014.

- [63] V. E. García Millán, G. A. Sanchez-Azofeifa, and G. C. Malvárez, “Mapping tropical dry forest succession with chris/proba hyperspectral images using non-parametric decision trees,” *IEEE Journal of Selected Topics in Applied Earth Observations and Remote Sensing*, vol. 8, pp. 3081–3094, June 2015.
- [64] D. Marinelli, F. Bovolo, and L. Bruzzone, “A novel change detection method for multitemporal hyperspectral images based on binary hyperspectral change vectors,” *IEEE Transactions on Geoscience and Remote Sensing*, vol. 57, pp. 4913–4928, July 2019.
- [65] D. M. Tratt, S. J. Young, J. A. Hackwell, D. J. Rudy, D. W. Warren, A. G. Vore, and P. D. Johnson, “Mahi: An airborne mid-infrared imaging spectrometer for industrial emissions monitoring,” *IEEE Transactions on Geoscience and Remote Sensing*, vol. 55, no. 8, pp. 4558–4566, 2017.
- [66] A. S. Moriya, N. N. Imai, A. M. G. Tommaselli, and G. T. Miyoshi, “Mapping mosaic virus in sugarcane based on hyperspectral images,” *IEEE Journal of Selected Topics in Applied Earth Observations and Remote Sensing*, vol. 10, no. 2, pp. 740–748, 2017.
- [67] Q. Xie, W. Huang, B. Zhang, P. Chen, X. Song, S. Pascucci, S. Pignatti, G. Laneve, and Y. Dong, “Estimating winter wheat leaf area index from ground and hyperspectral observations using vegetation indices,” *IEEE Journal of Selected Topics in Applied Earth Observations and Remote Sensing*, vol. 9, no. 2, pp. 771–780, 2016.
- [68] W. Huang, Q. Guan, J. Luo, J. Zhang, J. Zhao, D. Liang, L. Huang, and D. Zhang, “New optimized spectral indices for identifying and monitoring winter wheat diseases,” *IEEE Journal of Selected Topics in Applied Earth Observations and Remote Sensing*, vol. 7, no. 6, pp. 2516–2524, 2014.
- [69] C. M. Gevaert, J. Suomalainen, J. Tang, and L. Kooistra, “Generation of spectral–temporal response surfaces by combining multispectral satellite and hyperspectral uav imagery for precision agriculture applications,” *IEEE Journal of Selected Topics in Applied Earth Observations and Remote Sensing*, vol. 8, no. 6, pp. 3140–3146, 2015.
- [70] T. Sankey, J. Donager, J. McVay, and J. B. Sankey, “UAV lidar and hyperspectral fusion for forest monitoring in the southwestern USA,” *Remote Sensing of Environment*, vol. 195, pp. 30–43, 2017.
- [71] A. P. Crósta, C. Sabine, and J. V. Taranik, “Hydrothermal alteration mapping at bodie, california, using aviris hyperspectral data,” *Remote Sensing of Environment*, vol. 65, no. 3, pp. 309–319, 1998.
- [72] F. Kruse, J. Boardman, and J. Huntington, “Comparison of airborne hyperspectral data and eo-1 hyperion for mineral mapping,” *IEEE Transactions on Geoscience and Remote Sensing*, vol. 41, no. 6, pp. 1388–1400, 2003.
- [73] R. Vaughan, W. M. Calvin, and J. V. Taranik, “Sebas hyperspectral thermal infrared data: surface emissivity measurement and mineral mapping,” *Remote Sensing of Environment*, vol. 85, no. 1, pp. 48–63, 2003.

- [74] N. Yokoya, J. C.-W. Chan, and K. Segl, “Potential of resolution-enhanced hyperspectral data for mineral mapping using simulated enmap and sentinel-2 images,” *Remote Sensing*, vol. 8, no. 3, 2016.
- [75] G. Kereszturi, L. Schaefer, W. Schleiffarth, J. Procter, R. Pullanagari, S. Mead, and B. Kennedy, “Integrating airborne hyperspectral imagery and lidar for volcano mapping and monitoring through image classification,” *International Journal of Applied Earth Observation and Geoinformation*, vol. 73, pp. 323 – 339, 2018.
- [76] K. Tan, F. Wu, Q. Du, P. Du, and Y. Chen, “A parallel gaussian–bernoulli restricted boltzmann machine for mining area classification with hyperspectral imagery,” *IEEE Journal of Selected Topics in Applied Earth Observations and Remote Sensing*, vol. 12, no. 2, pp. 627–636, 2019.
- [77] F. Kühn, K. Oppermann, and B. Hörig, “Hydrocarbon index—an algorithm for hyperspectral detection of hydrocarbons,” *International Journal of Remote Sensing*, vol. 25, no. 12, pp. 2467–2473, 2004.
- [78] Q. Tian, “Study on oil-gas reservoir detecting methods using hyperspectral remote sensing,” *The International Archives of the Photogrammetry, Remote Sensing and Spatial Information Sciences*, vol. XXXIX-B7, pp. 157–162, 2012.
- [79] P. W. Yuen and M. Richardson, “An introduction to hyperspectral imaging and its application for security, surveillance and target acquisition,” *The Imaging Science Journal*, vol. 58, no. 5, pp. 241–253, 2010.
- [80] D. Manolakis, C. Siracusa, and G. Shaw, “Hyperspectral subpixel target detection using the linear mixing model,” *IEEE Transactions on Geoscience and Remote Sensing*, vol. 39, no. 7, pp. 1392–1409, 2001.
- [81] L. Zhang, L. Zhang, D. Tao, X. Huang, and B. Du, “Hyperspectral remote sensing image subpixel target detection based on supervised metric learning,” *IEEE Transactions on Geoscience and Remote Sensing*, vol. 52, no. 8, pp. 4955–4965, 2014.
- [82] E. Puckrin, C. S. Turcotte, P. Lahaie, D. Dubé, V. Farley, P. Lagueux, F. Marcotte, and M. Chamberland, “Airborne infrared-hyperspectral mapping for detection of gaseous and solid targets,” in *Chemical, Biological, Radiological, Nuclear, and Explosives (CBRNE) Sensing XI* (A. W. F. III and P. J. Gardner, eds.), vol. 7665, p. 766516, International Society for Optics and Photonics, SPIE, 2010.
- [83] Y. Chen, N. M. Nasrabadi, and T. D. Tran, “Sparse representation for target detection in hyperspectral imagery,” *IEEE Journal of Selected Topics in Signal Processing*, vol. 5, no. 3, pp. 629–640, 2011.
- [84] L. Zhang, L. Zhang, D. Tao, and X. Huang, “Sparse transfer manifold embedding for hyperspectral target detection,” *IEEE Transactions on Geoscience and Remote Sensing*, vol. 52, no. 2, pp. 1030–1043, 2014.

- [85] I. Reed and X. Yu, "Adaptive multiple-band cfar detection of an optical pattern with unknown spectral distribution," *IEEE Transactions on Acoustics, Speech, and Signal Processing*, vol. 38, no. 10, pp. 1760–1770, 1990.
- [86] H. Kwon and N. Nasrabadi, "Kernel rx-algorithm: a nonlinear anomaly detector for hyperspectral imagery," *IEEE Transactions on Geoscience and Remote Sensing*, vol. 43, no. 2, pp. 388–397, 2005.
- [87] M. Imani, "Rx anomaly detector with rectified background," *IEEE Geoscience and Remote Sensing Letters*, vol. 14, no. 8, pp. 1313–1317, 2017.
- [88] M.-A. Gagnon, P. Lagueux, J.-P. Gagnon, S. Savary, P. Tremblay, V. Farley, É. Guyot, and M. Chamberland, "Airborne thermal infrared hyperspectral imaging of buried objects," in *Detection and Sensing of Mines, Explosive Objects, and Obscured Targets XX* (S. S. Bishop and J. C. Isaacs, eds.), vol. 9454, p. 94540K, International Society for Optics and Photonics, SPIE, 2015.
- [89] D. E. Bar, K. Wolowelsky, Y. Swirski, Z. Figov, A. Michaeli, Y. Vaynzof, Y. Abramovitz, A. Ben-Dov, O. Yaron, L. Weizman, and R. Adar, "Target detection and verification via airborne hyperspectral and high-resolution imagery processing and fusion," *IEEE Sensors Journal*, vol. 10, no. 3, pp. 707–711, 2010.
- [90] I. Makki, R. Younes, C. Francis, T. Bianchi, and M. Zucchetti, "A survey of landmine detection using hyperspectral imaging," *ISPRS Journal of Photogrammetry and Remote Sensing*, vol. 124, pp. 40–53, 2017.
- [91] M. Shimoni, G. Tolt, C. Perneel, and J. Ahlberg, "Detection of vehicles in shadow areas using combined hyperspectral and lidar data," in *2011 IEEE International Geoscience and Remote Sensing Symposium*, pp. 4427–4430, 2011.
- [92] O. A. De Carvalho and P. R. Meneses, "Spectral correlation mapper (scm): an improvement on the spectral angle mapper (sam)," in *Summaries of the 9th JPL Airborne Earth Science Workshop, JPL Publication 00-18*, vol. 9, p. 2, JPL publication Pasadena, CA, USA, 2000.
- [93] Y. Du, C.-I. Chang, H. Ren, C.-C. Chang, J. O. Jensen, and F. M. D'Amico, "New hyperspectral discrimination measure for spectral characterization," *Optical Engineering*, vol. 43, no. 8, pp. 1777 – 1786, 2004.
- [94] M. Naresh Kumar, M. Seshasai, K. Vara Prasad, V. Kamala, K. Ramana, R. Dwivedi, and P. Roy, "A new hybrid spectral similarity measure for discrimination among vigna species," *International journal of remote sensing*, vol. 32, no. 14, pp. 4041–4053, 2011.
- [95] S. Padma and S. Sanjeevi, "Jeffries matusita-spectral angle mapper (jm-sam) spectral matching for species level mapping at bhitarkanika, muthupet and pichavaram mangroves," *The International Archives of the Photogrammetry, Remote Sensing and Spatial Information Sciences*, vol. XL-8, pp. 1403–1411, 2014.

- [96] L. Capobianco, A. Garzelli, and G. Camps-Valls, "Semi-supervised kernel orthogonal subspace projection," in *IGARSS 2008 - 2008 IEEE International Geoscience and Remote Sensing Symposium*, vol. 4, pp. IV – 216–IV – 219, 2008.
- [97] M. A. Veganzones, M. Datcu, and M. Grana, "Dictionary based hyperspectral image retrieval," in *Special Session on Pattern Recognition Applications in Remotely Sensed Hyperspectral Image Analysis*, vol. 2, pp. 426–432, SciTePress, 2012.
- [98] A. J. Plaza, J. Plaza, and A. Paz, "Parallel heterogeneous cbir system for efficient hyperspectral image retrieval using spectral mixture analysis," *Concurrency and Computation: Practice and Experience*, vol. 22, no. 9, pp. 1138–1159, 2010.
- [99] A. J. Plaza, "Content-based hyperspectral image retrieval using spectral unmixing," in *Image and Signal Processing for Remote Sensing XVII* (L. Bruzzone, ed.), vol. 8180, p. 81800O, International Society for Optics and Photonics, SPIE, 2011.
- [100] J. Zhang, Q. Zhou, L. Zhuo, W. Geng, and S. Wang, "A cbir system for hyperspectral remote sensing images using endmember extraction," *International Journal of Pattern Recognition and Artificial Intelligence*, vol. 31, no. 04, p. 1752001, 2017.
- [101] P. Zheng, Z. Wu, J. Sun, Y. Zhang, Y. Zhu, Y. Shen, J. Yang, Z. Wei, and A. Plaza, "A parallel unmixing-based content retrieval system for distributed hyperspectral imagery repository on cloud computing platforms," *Remote Sensing*, vol. 13, no. 2, 2021.
- [102] M. Graña and M. A. Veganzones, "An endmember-based distance for content based hyperspectral image retrieval," *Pattern Recognition*, vol. 45, no. 9, pp. 3472–3489, 2012. Best Papers of Iberian Conference on Pattern Recognition and Image Analysis (IbPRIA'2011).
- [103] M. A. Veganzones and M. Grana, "A spectral/spatial cbir system for hyperspectral images," *IEEE Journal of Selected Topics in Applied Earth Observations and Remote Sensing*, vol. 5, no. 2, pp. 488–500, 2012.
- [104] J. Sevilla and A. Plaza, "A new digital repository for hyperspectral imagery with unmixing-based retrieval functionality implemented on gpus," *IEEE Journal of Selected Topics in Applied Earth Observations and Remote Sensing*, vol. 7, no. 6, pp. 2267–2280, 2014.
- [105] J. Sevilla, L. I. Jiménez, and A. Plaza, "Sparse unmixing-based content retrieval of hyperspectral images on graphics processing units," *IEEE Geoscience and Remote Sensing Letters*, vol. 12, no. 12, pp. 2443–2447, 2015.
- [106] Z. Shao, W. Zhou, Q. Cheng, C. Diao, and L. Zhang, "An effective hyperspectral image retrieval method using integrated spectral and textural features," *Sensor Review*, vol. 35, no. 3, pp. 274–281, 2015.

- [107] W. Geng, J. Zhang, L. Zhuo, J. Liu, and L. Chen, “Creating spectral words for large-scale hyperspectral remote sensing image retrieval,” in *Advances in Multimedia Information Processing-PCM 2016: 17th Pacific-Rim Conference on Multimedia, Xi’an, China, September 15-16, 2016, Proceedings, Part II*, pp. 116–125, Springer, 2016.
- [108] J. Zhang, W. Geng, X. Liang, L. Zhuo, and L. Chen, “Secure retrieval method of hyperspectral image in encrypted domain,” *Journal of Applied Remote Sensing*, vol. 11, no. 3, p. 035021, 2017.
- [109] J. Zhang, W. Geng, X. Liang, J. Li, L. Zhuo, and Q. Zhou, “Hyperspectral remote sensing image retrieval system using spectral and texture features,” *Appl. Opt.*, vol. 56, pp. 4785–4796, Jun 2017.
- [110] J. Zhang, L. Chen, L. Zhuo, X. Liang, and J. Li, “An efficient hyperspectral image retrieval method: Deep spectral-spatial feature extraction with dcan and dimensionality reduction using t-sne-based nm hashing,” *Remote Sensing*, vol. 10, no. 2, 2018.
- [111] F. Ömriüzun and Y. Y. Çetin, “Gas detection in longwave infrared hyperspectral imagery and black body effect compensation,” in *2015 23rd Signal Processing and Communications Applications Conference (SIU)*, pp. 2341–2344, 2015.
- [112] F. Omruuzun and Y. Y. Cetin, “Endmember signature based detection of flammable gases in LWIR hyperspectral images,” in *Advanced Environmental, Chemical, and Biological Sensing Technologies XII* (T. Vo-Dinh, R. A. Lieberman, and G. G. Gauglitz, eds.), vol. 9486, p. 948612, International Society for Optics and Photonics, SPIE, 2015.
- [113] D. Sulla-Menashe and M. A. Friedl, “User guide to collection 6 modis land cover (mcd12q1 and mcd12c1) product,” *Usgs: Reston, Va, Usa*, vol. 1, p. 18, 2018.
- [114] T. Food and A. O. O. T. U. Nations, “Faostat database,” 2023. accessed November 03, 2023.
- [115] X. Xu, J. Li, C. Wu, and A. Plaza, “Regional clustering-based spatial preprocessing for hyperspectral unmixing,” *Remote Sensing of Environment*, vol. 204, pp. 333–346, 2018.
- [116] R. Achanta, A. Shaji, K. Smith, A. Lucchi, P. Fua, and S. Süsstrunk, “Slic superpixels compared to state-of-the-art superpixel methods,” *IEEE Transactions on Pattern Analysis and Machine Intelligence*, vol. 34, no. 11, pp. 2274–2282, 2012.
- [117] F. Kruse, A. Lefkoff, J. Boardman, K. Heidebrecht, A. Shapiro, P. Barloon, and A. Goetz, “The spectral image processing system (sips)—interactive visualization and analysis of imaging spectrometer data,” *Remote Sensing of Environment*, vol. 44, no. 2, pp. 145–163, 1993. Airbone Imaging Spectrometry.

- [118] M. Ester, H.-P. Kriegel, J. Sander, and X. Xu, “A density-based algorithm for discovering clusters in large spatial databases with noise,” in *Proceedings of the Second International Conference on Knowledge Discovery and Data Mining*, KDD’96, p. 226–231, AAAI Press, 1996.
- [119] J. M. P Nascimento and J. M. Bioucas-Dias, “Hyperspectral signal subspace estimation,” in *2007 IEEE International Geoscience and Remote Sensing Symposium*, pp. 3225–3228, 2007.
- [120] H. Photonics, “Nano-Hyperspec.” <https://cdn2.hubspot.net/hubfs/145999/June%202018%20Collateral/NanoHyperspec0118.pdf>. [Accessed August 25, 2019].
- [121] H. Photonics, *Micro-Hyperspec*, (accessed August 25, 2019). <https://cdn2.hubspot.net/hubfs/145999/June%202018%20Collateral/MicroHyperspec0418.pdf>.
- [122] H. Photonics, *VNIR-SWIR Co-Registered*, (accessed October 26, 2017). http://cdn2.hubspot.net/hub/145999/docs/ds_vnir_swir_pixel_co_registered_2014.pdf.
- [123] H. Photonics, *Hyperspec Fluorescence*, (accessed August 25, 2019). <https://cdn2.hubspot.net/hubfs/145999/June%202018%20Collateral/Fluorescence0418.pdf>.
- [124] SPECIM, *AisaFENIX*, (accessed October 26, 2017). http://www.specim.fi/downloads/AisaFenix%20ver1-2017_web.pdf.
- [125] SPECIM, *AisaFENIX 1K*, (accessed October 26, 2017). http://www.specim.fi/downloads/AisaFenix_1K%20ver1-2017_web.pdf.
- [126] SPECIM, *AiSAIBIS*, (accessed October 26, 2017). <http://www.specim.fi/downloads/AisaIBIS%20ver1-2017.pdf>.
- [127] SPECIM, *AisaOWL*, (accessed October 26, 2017). <http://www.specim.fi/downloads/AisaOWL%20ver1-2017.pdf>.
- [128] SPECIM, *AisaKESTREL*, (accessed October 26, 2017). <http://www.specim.fi/downloads/AisaKESTREL-ver2-2016.pdf>.
- [129] Resonon, *Airborne Hyperspectral Imaging Systems*, (accessed October 26, 2017). <https://www.resonon.com/data-sheets/ResononHyperspectralAirborne.Datasheet.pdf>.
- [130] Corning, *Hyperspectral Imaging Systems and Solutions*, (accessed October 26, 2017). <https://www.corning.com/worldwide/en/products/advanced-optics/product-materials/spectral-sensing.html>.
- [131] Itres, *SASI-1000A*, (accessed October 26, 2017). http://www.itres.com/wp-content/uploads/2014/10/SASI_1000A.pdf.

- [132] Itres, *MA SI-600*, (accessed October 26, 2017). <http://www.itres.com/wp-content/uploads/2014/10/MA SI-600.pdf>.
- [133] Itres, *TASI-600*, (accessed October 26, 2017). <http://www.itres.com/wp-content/uploads/2014/10/TASI-600.pdf>.
- [134] Itres, *microCASI-1920*, (accessed October 26, 2017). <http://www.itres.com/wp-content/uploads/2015/08/MicroCASI-Preliminary-Specifications.pdf>.
- [135] Itres, *microSASI-384*, (accessed October 26, 2017). <http://www.itres.com/wp-content/uploads/2015/08/MicroSASI-Preliminary-Specifications.pdf>.
- [136] T. Cocks, R. Jenssen, A. Stewart, I. Wilson, and T. Shields, “The hymaptm airborne hyperspectral sensor: The system, calibration and performance,” in *Proceedings of the 1st EARSeL workshop on Imaging Spectroscopy*, pp. 37–42, EARSeL, 1998.
- [137] TELOPS, *Hyperspectral IR Cameras*, (accessed October 26, 2017). <http://telops.com/products/hyperspectral-cameras>.
- [138] OCI, *OCI-UAV Hyperspectral Camera*, (accessed October 26, 2017). <http://www.bayspec.com/wp-content/uploads/2015/09/BaySpec-Datasheet-OCI-UAV-Hyperspectral-Camera.pdf>.
- [139] N. E. Optikk, *HySpex VNIR-1024*, (accessed October 26, 2017). https://www.hyspex.no/products/vnir_1024.php.
- [140] N. E. Optikk, *ODIN-1024*, (accessed October 26, 2017). <https://www.hyspex.no/products/odin.php>.
- [141] N. E. Optikk, *HySpex Mjolnir V-1240*, (accessed October 26, 2017). <https://www.hyspex.no/products/mjolnir.php>.
- [142] S. OPTICS, *SOC710-GX Airborne Hyperspectral Imager*, (accessed October 26, 2017). <https://surfaceoptics.com/products/hyperspectral-imaging/710-gx/>.
- [143] SENOP, *OPTRONICS HYPERSPECTRAL*, (accessed October 26, 2017). <http://senop.fi/en/optronics-hyperspectral>.
- [144] Cubert, *SI85*, (accessed October 26, 2017). <http://cubert-gmbh.com/wp-content/uploads/SI85-.pdf>.
- [145] X. Zhao, Z. Xiao, Q. Kang, Q. Li, and L. Fang, “Overview of the fourier transform hyperspectral imager (hsi) boarded on hj-1a satellite,” in *2010 IEEE International Geoscience and Remote Sensing Symposium*, pp. 4272–4274, 2010.
- [146] T. L. Wilson and C. O. Davis, “Naval EarthMap Observer (NEMO) satellite,” in *Imaging Spectrometry V* (M. R. Descour and S. S. Shen, eds.), vol. 3753, pp. 2 – 11, International Society for Optics and Photonics, SPIE, 1999.

- [147] T. Wilson, R. Felt, and R. Baugh, “Naval earthmap observer (nemo) hyper-spectral remote sensing program,” tech. rep., PRAXIS INC ALEXANDRIA VA, 2000.
- [148] ESA, *OrbView-4 - eoPortal Directory - Satellite Missions*, (accessed October 22, 2017).
- [149] L. Bourq and S. Delwart, “Meris instrument calibration,” in *Second MERIS and AATSR Calibration and Geophysical Validation Workshop, Frascati, Italy*, pp. 20–24, 2006.
- [150] ESA, “Meris product handbook,” tech. rep., 2006.
- [151] R. L. Lucke, M. Corson, N. R. McGlothlin, S. D. Butcher, D. L. Wood, D. R. Korwan, R. R. Li, W. A. Snyder, C. O. Davis, and D. T. Chen, “Hyperspectral imager for the coastal ocean: instrument description and first images,” *Appl. Opt.*, vol. 50, pp. 1501–1516, Apr 2011.
- [152] A. Hollinger, M. Bergeron, M. Maskiewicz, S. Qian, H. Othman, K. Staenz, R. Neville, and D. Goodenough, “Recent developments in the hyperspectral environment and resource observer (hero) mission,” in *2006 IEEE International Symposium on Geoscience and Remote Sensing*, pp. 1620–1623, 2006.
- [153] ISRO, *ISRO Develops Optical Imaging Detector Array for Hyperspectral Imaging Applications*, (accessed October 22, 2017). <https://www.isro.gov.in/>
- [154] S. Michel, P. Gamet, and M.-J. Lefevre-Fonollosa, “Hypxim — a hyperspectral satellite defined for science, security and defence users,” in *2011 3rd Workshop on Hyperspectral Image and Signal Processing: Evolution in Remote Sensing (WHISPERS)*, pp. 1–4, 2011.
- [155] C. Galeazzi, R. Carpentiero, V. De Cosmo, L. Garramone, F. Longo, E. Lopinto, and G. Varacalli, “The prisma system an pan/hyp instrument,” in *Proceedings of the 6th EARSeL Imaging Spectroscopy SIG (Special Interest Group) Workshop*, 2009.
- [156] ASI, *Space Segment*, (accessed October 22, 2017). <http://prisma-isi.it/index.php/en/mission/space-segment>.
- [157] DLR, *EnMAP HSI Instrument Specification*, (accessed October 22, 2017). http://www.enmap.org/sites/default/files/pdf/Table_EnMAP_Specs.pdf.
- [158] T. Stuffer, C. Kaufmann, S. Hofer, K. Förster, G. Schreier, A. Mueller, A. Eckardt, H. Bach, B. Penné, U. Benz, and R. Haydn, “The enmap hyperspectral imager—an advanced optical payload for future applications in earth observation programmes,” *Acta Astronautica*, vol. 61, no. 1, pp. 115–120, 2007. Bringing Space Closer to People, Selected Proceedings of the 57th IAF Congress, Valencia, Spain, 2-6 October, 2006.

- [159] ESA, *Copernicus: Sentinel-5 (Atmospheric Monitoring Mission) in LEO*, (accessed October 22, 2017). <https://directory.eoportal.org/web/eoportal/satellite-missions/c-missions/copernicus-sentinel-5>.
- [160] S. Kraft, U. Del Bello, M. Bouvet, M. Drusch, and J. Moreno, “Flex: Esa’s earth explorer 8 candidate mission,” in *2012 IEEE International Geoscience and Remote Sensing Symposium*, pp. 7125–7128, 2012.
- [161] C. M. Lee, M. L. Cable, S. J. Hook, R. O. Green, S. L. Ustin, D. J. Mandl, and E. M. Middleton, “An introduction to the nasa hyperspectral infrared imager (hyspirci) mission and preparatory activities,” *Remote Sensing of Environment*, vol. 167, pp. 6–19, 2015. Special Issue on the Hyperspectral Infrared Imager (HyspIRI).
- [162] C. Bruce, “Hyspirci mission concept overview and recent ice and trl activities,” in *Proc. HyspIRI Sci. Workshop*, 2012.
- [163] M. J. Abrams and S. J. Hook, *NASA’s Hyperspectral Infrared Imager (HyspIRI)*, pp. 117–130. Dordrecht: Springer Netherlands, 2013.
- [164] J.-Y. Labandibar, Y. Delclaud, U. D. Bello, R. Meynart, R. Garrels, and G. Adami, “PRISM: processes research by imaging space mission,” in *Infrared Spaceborne Remote Sensing IV* (M. S. Scholl and B. F. Andresen, eds.), vol. 2817, pp. 14 – 23, International Society for Optics and Photonics, SPIE, 1996.
- [165] M. Rast, F. Baret, B. van den Hurk, W. Knorr, W. Mauser, M. Menenti, J. Miller, J. Moreno, M. Schaepman, and M. Verstraete, “Spectra-surface processes and ecosystem changes through response analysis,” tech. rep., ESA Publications Division, 2004.
- [166] M. Crisconio, V. D. Cosmo, A. Foni, and R. Loizzo, “Hypseo: Demonstration mission for a new earth observation hyperspectral sensor,” in *3rd International Symposium of the IAA on Small Satellites for Earth Observation*, pp. 1–7, Berlino, 2001, 2001.
- [167] A. Schoonwinkel, H. Burger, and S. Mostert, “Integrated hyperspectral, multi-spectral and video imager for microsatellites,” 2005.

Appendix A

LIST OF AIRBORNE HYPERSPECTRAL REMOTE SENSING SYSTEMS

IMAGER	MANUFACTURER / OWNER	AIRCRAFT TYPE	SPECTRAL RANGE (nm)	NUMBER OF BANDS	NUMBER OF SPATIAL PIXELS	SPECTRAL SAMPLING (nm)	SPECTRAL SCANNING	SPATIAL SCANNING	BIT DEPTH
AIS-1 [13]	NASA	Manned	900-2400	128	32	9.3	n/a	n/a	n/a
AIS-2 [13]		Manned	800-2400	128	64	10.6	n/a	n/a	n/a
ASAS [14]		Manned	465-871	29	512	15	Grating	Push-broom	16
AVIRIS [15]		Manned	400-2500	224	614	10	Grating	Whisk-broom	12
HYDICE [17,18]	HDOS		400-2500	210	320	10.2	Prism	Push-broom	16
SYSIPHE [19]	ONERA	Manned	400-1400 1400-2500 3000-5500 8000-11500	~ 500	VNIR: 1024 SWIR:1024 MWIR:1016 LWIR:1016	VNIR:5 SWIR:6.1 MWIR:13 cm-1 LWIR: 6 cm-1	VNIR-SWIR: Grating / MWIR-LWIR: Interferometer	Push-broom	n/a
TRWIS-A [13]	TRW Space	Manned	430-850	128	240	3.3	Grating	Push-broom	8
TRWIS-B [13]		Manned	460-880	90	241	4.8	Grating	Push-broom	8
TRWIS-II [20]		Manned	1500-2500	80	242	12	Grating	Push-broom	8
TRWIS-III [21]		Manned	400-2450	384	256	5/6.25	Grating	Push-broom	12
AAHIS-1 [22]	SETS Technology - SAIC	Manned	432-832	288	192	5.5	Grating	Push-broom	12
AHS (MAS) [13]	Daedalus Enterprises	Manned	440-12700	48	n/a	200-1500	n/a	n/a	12
DAIS-7915 [23]	DLR	Manned	450-1050 1500-1800 1900-2500	VNIR:32 SWIR-1:8 SWIR-2:32	512	VNIR:15-30 SWIR-1:45 SWIR-2:35	Grating	Push-broom	15

IMAGER	MANUFACTURER / OWNER	AIRCRAFT TYPE	SPECTRAL RANGE (nm)	NUMBER OF BANDS	NUMBER OF SPATIAL PIXELS	SPECTRAL SAMPLING (nm)	SPECTRAL SCANNING	SPATIAL SCANNING	BIT DEPTH
ROSIS [24]		Manned	430-860	115	512	4	Grating	Push-broom	14
SMIFTS [13]	University of Hawaii	Manned	1000-5200 3200-5200	75-35	256	100cm-1 - 50cm-1	Interferometer	n/a	n/a
ARCHER (NovaSol 1100-2) [25]	US Arif Force Civil Air Patrol	Manned	500-1100	52	504	11.5	Grating	Push-broom	n/a
COMPASS [26]	US Government	Manned	400-2350	256	256	8	Grating	Whisk-broom	14
SEBASS [28, 29]	Aerospace Corporation	Manned	2500-5200 7500-13500	128	128	MWIR:25 LWIR:50	n/a	Push-broom	24
Nano-Hyperspec [120]	Headwall Photonics	Manned / Unmanned	400-1000	270	640	2.1	Grating	Push-broom	12
Micro-Hyperspec [121]		Manned / Unmanned / Satellite	400-1000 900-1700 600-1700 900-2500	VNIR:325-369 NIR:67-134 Ex-VNIR:267 SWIR:166-267	VNIR:1004-1600 NIR:320-640 Ex-VNIR:640 SWIR:384-640	VNIR:1.6-1.9 NIR:6-12 Ex-VNIR:4.1 SWIR:6-9.6	Grating	Push-broom	12-16
Hyperspec Co-Registered [122]		Manned / Unmanned	400-2500	VNIR:384 SWIR:166	VNIR:1600 - SWIR:384	VNIR:1.6 SWIR:10.8	Grating	Push-broom	16
Hyperspec Fluorescence [123]		Manned / Unmanned	670-780	2160	1600	0.1-0.2	Grating	Push-broom	16
AisaFENIX [124]	SPECIM	Manned	380-970 970-2500	VNIR:87-348 SWIR:274	384	VNIR:1.7-6.8 SWIR:5.7	Grating	Push-broom	12-16
AisaFENIX 1K [125]		Manned	380-970 970-2500	VNIR:87-348 SWIR:256	1024	VNIR:1.7-6.8 SWIR:6.3	Grating	Push-broom	12-16
AiSAIBIS [126]		Manned	670-780	n/a	384-768	0.11-0.22	Grating	Push-broom	16
AisaOWL [127]		Manned	7700-12300	96	384	100	Grating	Push-broom	16
AisaKESTREL [128]		Manned / Unmanned	400-1000 600-1640	n/a	640-2040	1.75 - 7	n/a	Push-broom	12-14
Pika [129]	Resonon	Manned / Unmanned	350-800 400-1000 900-1700	VNIR:196 VNIR:281-447 NIR:164-328	VNIR:1600 VNIR:900-1600 NIR:320-640	VNIR:2.3 VNIR:1.3-2.1 NIR:2.5-4.9	Grating	Push-broom	12-14
SHARK [130]	Corning	Manned / Unmanned	400-1000	155	704	2	Grating	Push-broom	12

IMAGER	MANUFACTURER / OWNER	AIRCRAFT TYPE	SPECTRAL RANGE (nm)	NUMBER OF BANDS	NUMBER OF SPATIAL PIXELS	SPECTRAL SAMPLING (nm)	SPECTRAL SCANNING	SPATIAL SCANNING	BIT DEPTH
CASI-1500 [127]	ITRES	Manned	380-1050	288	1500	2.4	n/a	Push-broom	14
SASI-1000A [131]		Manned	950-2450	100	600	15	n/a	Push-broom	14
MASI-600 [132]		Manned	3000-5000	64	600	32	n/a	Push-broom	14
TASI-600 [133]		Manned	8000-11500	32	600	110	n/a	Push-broom	14
microCASI-1920 [134]		Unmanned	400-1000	288	1920	2.1	n/a	Push-broom	12
microSASI-384 [135]		Unmanned	1000-2500	200	384	6	n/a	Push-broom	14
HyMAP [136]	Integrated Spectronics	Manned	450-890 890-1350 1400-1800 1950-2480	128	512	VIS:15 NIR:15 SWIR1:13 SWIR2:17	Grating	Whisk-broom	n/a
Hyper-Cam [137]	TELOPS	Manned	3000-5000 8000-12000	n/a	320 x 256	0.25 cm-1	Interferometer	Snapshot	n/a
OCI-1000 [138]	BaySpec	Unmanned	600-1000	100	2048	5	Filter	Push-broom	n/a
OCI-2000 [138]		Unmanned	600-1000	20-25	400x200	12-15	Filter	Snapshot	n/a
HySpex [139]	NEO	Manned / Unmanned	400-1000 1000-2500	VNIR:108-182 SWIR:288	VNIR:1024-1800 SWIR:384	VNIR:3.26-5.4 SWIR:5.45	Grating	Push-broom	12-16
HySpex ODIN [140]		Manned	400-2500	427	1024	VNIR:3.6 SWIR:6.1	Grating	Push-broom	16
HySpex Mjolnir V-1240 [141]		Unmanned	VNIR:400-1000	200	2048	3	Grating	Push-broom	12
SOC710-GX [142]	SURFACE OPTICS	Manned / Unmanned	400-1000	120	640	4.2	Grating	Push-broom	12
Rikola [143]	SENOP	Manned / Unmanned	500-900	100	1010 x 1010	10	Filter	Snapshot	12
Cubert [144]	Rikola	Manned / Unmanned	450-950	125	1 MP	4	Filter	Snapshot	12

Appendix B

LIST OF SPACEBORNE HYPERSPECTRAL REMOTE SENSING SYSTEMS

IMAGER	COUNTRY / ORGANIZATION	MISSION	PLATFORM	SPECTRAL RANGE (nm)	NUMBER OF BANDS	SPECTRAL SAMPLING	SWATH (km)	GSD (m)	ALTITUDE (km)	SPECTRAL SCANNING	SPATIAL SCANNING	BIT DEPTH	LAUNCH DATE	STATUS
HIRIS [32,33]	US / NASA	EOS	Satellite	400-1000 1000-2500	224	9.4 VNIR 11.7 SWIR	30	30	824	n/a	Whisk-broom	12	n/a	Cancelled
HRIS [34]	Multinational / ESA	n/a	Satellite	450-2350	n/a	10	30	40	800	Grating/Prism	Push-broom	n/a	n/a	Cancelled
ARIES [35]	Australia / ARIES	ARIES-1	Satellite	400-1000 1000-2500	n/a	20-VNIR 16-SWIR	15	n/a	800	n/a	n/a	n/a	n/a	Cancelled
HIS [45]	US / NASA	LEWIS	Satellite	400-1000 900-2500	384	5-VNIR 6.4-SWIR	7.7	30	523	Grating	Push-broom	12	1997	Deorbited
FTHSI [36]	US / USAF	MightySat II	Satellite	475-1050	256	84.4 cm-1-0.1 cm-1	7.5-30	30	556	Interferometer	Push-broom	12	2000	Deorbited
COIS [146,147]	US / USAF	NEMO	Satellite	400-1000 1000-2500	60-VNIR 150-SWIR	10	30	60	605	n/a	n/a	n/a	2000	Cancelled
Hyperion [37]	US / NASA	EO-1	Satellite	400-2500	220	10	7.5	30	705	Grating	Push-broom	12	2000	Decomm.
OHIS [148]	US / OrbImage	OrbView-4	Satellite	400-905 830-1750 1580-2490	40-VNIR 80-NIR 80-SWIR	11.4	5	8	470	n/a	Whisk-broom	12	2001	Failed
CHRIS [39,40]	Multinational / ESA	Proba	Satellite	415-1050	18-62	1.3-11.3	14	17 34	560	Prism	Push-broom	12	2001	Active
MERIS [149,150]	Multinational / ESA	ENVISAT-1	Satellite	390-1040	15	1.8	1150	300	790	Grating	Push-broom	12	2002	Failed
HIM [43,44]	China / CNSA	Chang'e-1	Satellite	480-960	32	n/a	25.6	200	200 (lunar)	Interferometer	n/a	12	2007	Deorbited
HIS [145]	China / CAST	HJ-1	Satellite	459-956	115	98.5 cm-1	50	100	650	Interferometer	Push-broom	12	2008	Active
HySI [45,46]	India / ISRO	Chandrayaan-1	Satellite	421-964	32	15	20	80	100 (lunar)	Filter	Push-broom	12	2008	Deorbited
M³ [46,47]	India / ISRO	Chandrayaan-1	Satellite	400-3000	260	n/a	40	67	100 (lunar)	Grating	Push-broom	12	2008	Deorbited

IMAGER	COUNTRY / ORGANIZATION	MISSION	PLATFORM	SPECTRAL RANGE (nm)	NUMBER OF BANDS	SPECTRAL SAMPLING	SWATH (km)	GSD (m)	ALTITUDE (km)	SPECTRAL SCANNING	SPATIAL SCANNING	BIT DEPTH	LAUNCH DATE	STATUS
Artemis [50,151]	US / DoD	TacSat-3	Satellite	400-2500	400	5	n/a	n/a	425	Grating	Push-broom	10	2009	Deorbited
HICO [151]	US / Naval Research	ISS	Station	350-1080	n/a	5.73	42	83	350-400	Grating	Push-broom	14	2009	Mulfunct.
HERO [152]	Canada / CSA	HERO	Satellite	400-2500	>200	10	30	30	700	Grating	Push-broom	12	2010	Cancelled
HIS [48,49]	China / CNSA	Tiangong-1	Station	400-1000 1000-2500	64 VNIR / 64 SWIR	10 VNIR 23 SWIR	10	10 20	300-400	n/a	n/a	n/a	2011	Deorbited
Claire [57,58,59]	Canada / GHGSat	Claire	Satellite	400-1000 1600-1700	325 VNIR	1.9 VNIR	n/a	50	512	Grating	Push-broom	n/a	2016	Active
HysIS [153]	India / ISRO	Hyspex	Satellite	400-950	55	10	n/a	30	630	n/a	Push-broom	n/a	>2017	Design phase
HYPXIM [154]	France / CNES	HYPXIM	Satellite	400-2500	>200	10	15-30	10 20	650	n/a	n/a	n/a	>2017	Design phase
DESI [52,53,54]	Germany / DLR	ISS	Station	450-950	240	2.32	44 57	79- 104	330-435	Grating	Push-broom	12	2018	Design phase
PRISMA [155,156]	Italy / ASI	PRISMA	Satellite	400-2500	239	12	30	30	615	Prism	Push-broom	12	2018	Design phase
EnMAP [157,158]	Germany / DLR	EnMAP	Satellite	420-2450	228	6.5 VNIR 10 SWIR	30	30	652	Prism	Push-broom	14	2019	Design phase
HISUI [55,56]	Japan / JAXA	ALOS-3	Satellite	400-970 1000-2500	57 VNIR 128 SWIR	10 VNIR 12.5 SWIR	30	30	618	Grating	Push-broom	12	2019	Launched
UVNS [159]	Multinational / ESA	Sentinel-5	Satellite	270-310 300-500 685-710 750-773 1590-1675 2305-2385	n/a	0.25-1	2670	7500	817	Grating	Push-broom	n/a	2021	Design phase
FLORIS [160]	Multinational / ESA	FLEX	Satellite	500-780	n/a	0.3-3	150	300	815	Grating	n/a	n/a	2022	Design phase
HyspIRI [161,162,163]	US / NASA	HyspIRI	Satellite	380-2510	n/a	10	153	60	626	Grating	Whiskbroom	14	>2022	Design phase
PRISM [164]	ESA	PRISM	Satellite	450-2500	n/a	12	50	50	666	Prism	Push-broom	12	n/a	Cancelled
SPECTRA [165]	Multinational / ESA	SPECTRA	Satellite	400-2350	n/a	<15	50	50- 100	n/a	n/a	n/a	n/a	n/a	Cancelled
HypSEO [166]	Italy / ASI	MITA	Satellite	400-1000 1000-2500	210	10	20	20	619.6	n/a	Push-broom	12	n/a	Cancelled
MSMI [167]	S. Africa / SUNSAT	ARM	Satellite	400-2350	>200	10	15	15	660	Prism	Push-broom	n/a	n/a	Ready for launch

Appendix C

SYMBOLS AND THEIR DESCRIPTIONS

Symbol	Description
$\mathbf{X} = \{\mathbf{X}_n\}_{n=1}^N$	Archive of N hyperspectral images
\mathbf{X}_n	n -th hyperspectral image in \mathbf{X}
\mathbf{X}_q	Query hyperspectral image
\mathbf{X}^R	The ranked set of R retrieved images that are most similar to \mathbf{X}_q
\mathbf{X}_r	r -th retrieved hyperspectral image in \mathbf{X}^R
W	Number of spectral bands
P	Number of pixels
$\mathbf{x}_n^p \in \mathbb{R}^W$	Spectral signature vector of p -th spatial pixel in \mathbf{X}_n , where $1 \leq p \leq P$
$\mathbf{V}^f = [\mathbf{v}_1^f, \dots, \mathbf{v}_\Psi^f]$	Foreground content spectral vocabulary, where $\mathbf{v}_\psi \in \mathbb{R}^W$ and $\psi = 1, 2, \dots, \Psi$
$\mathbf{V}^b = [\mathbf{v}_1^b, \dots, \mathbf{v}_\Omega^b]$	Background content spectral vocabulary, where $\mathbf{v}_\omega \in \mathbb{R}^W$ and $\omega = 1, 2, \dots, \Omega$
ϕ_n^f	Foreground content spectral descriptor of \mathbf{X}_n
ϕ_n^b	Background content spectral descriptor of \mathbf{X}_n
ϕ_n	Overall content spectral descriptor of \mathbf{X}_n
ϕ_q	Overall content spectral descriptor of \mathbf{X}_q
α_n^f	Foreground content abundance descriptor of \mathbf{X}_n
α_n^b	Background content abundance descriptor of \mathbf{X}_n
α_n	Overall content abundance descriptor of \mathbf{X}_n
α_q	Overall content abundance descriptor of \mathbf{X}_q
$\sigma_{\mathbf{X}_n}$	Spectral diversity of \mathbf{X}_n
S	Number of content segments extracted from \mathbf{X}_n
s	s -th content segment extracted from \mathbf{X}_n
\mathbf{x}_n^s	Spectral signature representing s -th segment extracted from \mathbf{X}_n
$\mu_{\mathbf{B}}$	Sample mean for territorial background image \mathbf{B}
\mathbf{B}	Territorial background image
$\Gamma_{\mathbf{B}}^{-1}$	Covariance matrix for territorial background image
$\mathbf{L}_{\mathbf{X}}$	Set of associated category labels with archive \mathbf{X}
$\mathbf{L}_{\mathbf{X}_q}$	Set of associated category labels with \mathbf{X}_q
$\mathbf{L}_{\mathbf{X}_r}$	Set of associated category labels with \mathbf{X}_r

CURRICULUM VITAE

PERSONAL INFORMATION

Surname, Name: Ömriüzun, Fatih

EDUCATION

Degree	Institution	Year of Grad.
M.A. in I.P. Rights and Innov. Man.	Ankara University	2023
M.Sc. in Information Systems	METU	2011
B.Sc. in Computer Engineering	European University of Lefke	2007

PROFESSIONAL EXPERIENCE

Year	Place	Enrollment
2015-	Visratek Defense & Information Technologies	Managing Director
2015-2016	RSLAB, University of Trento	Visiting Researcher
2008-2015	Graduate School of Informatics, METU	Research Assistant
2007-2008	MOBILTRUST Information Technologies	Software Engineer

PUBLICATIONS

Journal Articles

[1] Ömriüzun, F.; Yardımcı Çetin, Y.; Leloğlu, U.M.; Demir, B. A Novel Semantic Content-Based Retrieval System for Hyperspectral Remote Sensing Imagery. *Remote Sens.* 2024, 16, 1462. <https://doi.org/10.3390/rs16081462>.

Book Chapters

[1] Temizel, A.; Halici, T.; Logoglu, B.; Temizel, T.; Omruuzun, F.; Karaman, E., “Experiences on image and video processing with CUDA and OpenCL”, in *GPU Computing Gems Emerald Edition*, 1st ed., W. Hwu, Ed. Boston, MA: Morgan Kaufmann, 2011, pp. 547-567.

International Conference Publications

- [1] Başkurt, D.; Gür, Y.; Ömrüuzun, F.; Cetin, Y.Y., ‘Gas detection by using transmittance estimation and segmentation approaches’, in SPIE Remote Sensing – Remote Sensing Technologies and Applications in Urban Environments, Edinburgh, 2016.
- [2] Ömrüuzun, F.; Demir, B.; Bruzzone, L.; Cetin, Y.Y., ‘Content Based Hyperspectral Image Retrieval Using Bag of Endmembers Image Descriptors’, in Workshop on Hyperspectral Image and Signal Processing: Evolution in Remote Sensing (IEEE WHISPERS), Los Angeles, 2016.
- [3] Omruuzun, F.; Baskurt, D.; Daglayan, H.; Cetin, Y.Y., “Utilizing hyperspectral remote sensing imagery for afforestation planning of partially covered areas”, in SPIE 9643, Image and Signal Processing for Remote Sensing, Toulouse, 2015.
- [4] Omruuzun, F.; Baskurt, D.; Cetin, Y.Y., “DTW based signal alignment for enhancing CO2 detection in MWIR hyperspectral imagery”, in Workshop on Hyperspectral Image and Signal Processing: Evolution in Remote Sensing (IEEE WHISPERS), Tokyo, 2015.
- [5] Omruuzun, F.; Cetin, Y.Y., “Endmember signature based detection of flammable gases in LWIR hyperspectral images”, in SPIE 9486, Advanced Environmental, Chemical, and Biological Sensing Technologies XII, Baltimore, 2015.
- [6] Omruuzun, F., Baskurt, D.; Daglayan, H.; Cetin, Y.Y., “Shadow removal from VNIR hyperspectral remote sensing imagery with endmember signature analysis”, in SPIE 9482, Next-Generation Spectroscopic Technologies VIII, Baltimore, 2015.
- [7] Omruuzun, F.; Cetin, Y.Y., “Content based hyperspectral image retrieval: a systematic review”, in Hyperspectral Imaging and Applications Conference, Coventry, 2014.
- [8] Omruuzun, F., Ozdemir, O.B.; Cetin, Y.Y., “METU SPEL: Development of a new spectral signature library for food products”, in International Conference on Mass Data Analysis with Applications in Medicine, r/g/b Biotechnology, Food Industries and Dietetics, Biometry and Security, and Agriculture (MDA 2014), St. Petersburg, 2014, pp. 15-24.
- [9] Alasehir, O.; Omruuzun, F.; Baykal, N., “Understanding university ranking systems and necessity of a new ranking system for Turkey”, in International Higher Education Congress: New Trends and Issues (UYK-2011), Istanbul, 2011, pp. 1003-1009.
- [10] Omruuzun, F.; Alasehir, O., “URAP – University Ranking by Academic Performance”, in IREG Forum: National University Rankings on the Rise, Bratislava, 2011.

[11] Alasehir, O.; Omruuzun, F., “A New Glocal Ranking System: URAP-TR”, in Istanbul, Seventh International Conference on Webometrics, Informetrics and Scientometrics (WIS) & Twelfth COLLNET Meeting, 2015.

National Conference Publications

[1] Gür, Y.; Ömrüuzun, F.; Başkurt, D.; Cetin, Y.Y., ‘Detection and Identification of Gas Emission in Hyperspectral Imagery’, in 7th National Conference on Defense Applications Modeling And Simulation, Ankara, 2017.

[2] Ömrüuzun, F.; Demir, B.; Bruzzone, L.; Cetin, Y.Y., ‘A Novel Content Based Hyperspectral Image Retrieval System Based on Bag of End Members’, in IEEE 24th Signal Processing and Communications Applications Conference, Zonguldak, 2016.

[3] Başkurt Ö., D.; Gür, Y.; Ömrüuzun, F.; Cetin, Y.Y., ‘Absorbance Estimation and Gas Emissions Detection in Hyperspectral Imagery’, in IEEE 24th Signal Processing and Communications Applications Conference, Zonguldak, 2016.

[4] Omruuzun, F.; Baskurt, D.; Cetin, Y.Y., ‘Hyperspectral Unmixing Based Analysis of Forested Areas’, in IEEE 23th Signal Processing and Communications Applications Conference, Malatya, 2015.

[5] Omruuzun, F.; Baskurt, D.; and Cetin, Y.Y., ‘Gas Detection in Longwave Infrared Hyperspectral Imagery and Black Body Effect Compensation’, in IEEE 23th Signal Processing and Communications Applications Conference, Malatya, 2015.

[6] Pacin, Y.; Omruuzun, F., ‘Evaluation of Public Service Internet Sites’, in 30th National Informatics Congress, Ankara, 2013.

[7] Ordu, C.; Arifoglu, A.; Omruuzun, F., “e-service performance evaluation: municipalities”, in Smart Cities, VI. Istanbul Informatics Congress, Istanbul, 2012.